Spectroscopy and engineering of single rare-earth solid-state qubits

Von der Fakultät 8 Mathematik und Physik der Universität Stuttgart zur Erlangung der Würde eines Doktors der Naturwissenschaften (Dr. rer. nat.) genehmigte Abhandlung

Vorgelegt von

Thomas Kornher

aus Heidelberg

Hauptberichter: Prof. Dr. Jörg Wrachtrup

Mitberichter: Prof. Dr. Peter Michler

Tag der mündlichen Prüfung: 05.08.2020

3. Physikalisches Institut der Universität Stuttgart
2020

Contents

List of Abbreviations

AFM	**Atomic-Force Microscope**
AOM	**Acousto-Optic Modulator**
CCE	**Cluster-Correlation Expansion**
CPMG	**Carr-Purcell-Meiboom-Gill**
CQED	**Cavity Quantum ElectroDynamics**
CW	**Continous Wave**
ESA	**Excited State Absorption**
FEM	**Finite Element Method**
FFT	**Fast Fourier Transform**
FIB	**Focused Ion Beam**
FID	**Free Induction Decay**
FSR	**Free Spectral Range**
FWHM	**Full Width at Half Maximum**
LN	**Lithium Niobate**
LNOI	**Lithium Niobate On Insulator**
MW	**MicroWave**
ODMR	**Optically Detected Magnetic Resonance**
PSF	**Point Spread Function**
RIE	**Reactive Ion Etching**
RWA	**Rotating-Wave Approximation**
SEM	**Secondary Electron Microscope**
SIL	**Solid Immersion Lens**
STM	**Scanning Tunneling Microscope**
TEM	**Transmission Electron Microscope**
WGMR	**Whispering Gallery Mode Resonator**
ZPL	**Zero-Phonon Line**

Summary

Single quantum systems interacting with light provide essential functionality for their application as building blocks in future quantum networks, and also present an opportunity for their own investigation with optical means. Solids doped with rare-earth ions are an attractive platform, that can act as such a light-matter interface, capable of reversibly transferring quantum information between photons and atoms, based on their unique optical and spin properties. Yet, the implementation of rare-earth ions in scalable quantum architectures remains a challenging task due to diverse reasons. Typically weak interaction with light, sparsely explored electron spin properties in dense nuclear spin bath host materials, and limited nanofabrication technology when compared to other material systems are among the most pressing issues. In pursuit of overcoming weak light-matter interaction, several routes towards rare-earth ion integration into photonic resonators, which allows to boost light-matter interaction, are presented in this work. Furthermore, single rare-earth ions are explored as versatile probes for both, their unique immediate magnetic environment, and also for a deterministic doping technique.

This thesis begins with discussing experiments with cerium-ion-related electron spins in a YSO matrix, which will give insight into electron spin interaction with nearby nuclear spins in a material with a dense nuclear spin bath. As an introduction, the method of optical isolation of cerium is presented, fundamental to the experiment. In the following, the electron spin properties are investigated at cryogenic temperatures, under which circumstances

the spin lifetime is found to extend to several hundred microseconds. Coherent control of the electron spin with microwaves show spin coherences to persist for durations on the order of hundred microseconds, sufficiently long to isolate proximal ^{89}Y nuclear spins from the nuclear spin bath of ^{89}Y . The coherent interaction time also allows for the detection of a single nearby ^{29}Si nuclear spin, native to the host material with approximately 5% abundance. These results establish single rare-earth ions to be used as probes for single nuclear spins in their environment; single nuclear spins are a potentially useful resource in quantum error correction schemes, that can ultimately facilitate scalability for quantum networks. The discussed findings open up access to a broad range of materials, that can now be considered for quantum applications, due to versatile doping of rare-earth ions into solid state hosts.

In the second part, a deterministic doping technique is studied. Single rare-earth ion microscopy on praseodymium in a YAG matrix is introduced as a means to characterize a Paul-trap-based single ion implantation device. Based on the appreciably high conversion yield of implanted praseodymium ions into fluorescent color centers, integer number resolved fluorescence signals are found in implanted spots, revealing quantized creation of color centers. These findings provide access to studying color center formation and also the conversion yield was quantified to up to 50%. The utilized upconversion microscopy also allows to describe the spatial quality of the single ion doping, yielding a positioning accuracy of 72nm and precision of 34nm. These results establish a novel, material independent deterministic doping technique as promising tool for various solid-state approaches concerned with quantum networks.

In the last part of the thesis, rare-earth integration into photonic resonators is investigated, targeted at enhancing light interaction with rare-earth emitters and enabling scalable light-matter interfaces. Two different material

platforms are presented, both with their unique approach for realizing rare-earth-based quantum architectures. Thin films made out of amorphous silicon-doped titanium dioxide and deposited on various host crystals are introduced as a first photonic platform. Due to films exhibiting a higher refractive index than subjacent crystals, films support waveguiding of light and are shown to be shaped into waveguides and photonic resonators with low propagation loss and high quality factors. Further, evanescent coupling between light modes in resonators and emitters located in the subjacent host crystals is demonstrated. During cryogenic experiments, emitter properties were also identified to be unaffected by the fabrication protocol, laying a foundation for further resonant studies of emitters interfaced with titanium-dioxide-based resonators. As a second photonic platform, targeted at Purcell-enhancement based lifetime shortening of emitters interfaced with photonic resonators under electro-optic control, the lithium-niobate-on-insulator platform is introduced. The fabrication of photonic structures and their implantation doping with various rare-earth species is demonstrated. Characterization of fabricated devices show sufficiently high quality factors and low mode volumes, which in principle allow for measurements of Purcell enhancement. Electro-optically modulated lifetime measurements reveal the degree of lifetime shortening and an appended analysis of doping procedure allows to consider routes for future improvements towards single ion detection based on integrated resonators. The presented work provides access to a novel photonic platform with potentially remarkable control over individual devices or nodes in a network, yielding a particularly high degree of scalablility in rare-earth-based quantum architectures.

Zusammenfassung

Einzelne Quantensysteme, die mit Licht wechselwirken, stellen eine grundlegende Funktionalität bereit, um sie als Bausteine in zukünftigen Quantennetzwerken zu verwenden und bieten zudem die Möglichkeit an, sie selbst mit optischen Mittel zu erforschen. Festkörper die mit Elementen der seltenen Erden dotiert sind, stellen eine attraktive Plattform für solche einzelnen Quantensysteme dar, welche als Schnittstelle zwischen Licht und Materie fungieren können. Eine derartige Schnittstelle erlaubt es Quanteninformationen zwischen Photonen und Atomen in einer reversiblen Art und Weise zu transferieren, und im Beispiel an Ionen der seltenen Erden ist dies auf deren einzigartige, optische- und spin-physikalische Eigenschaften zurückzuführen.

Die Implementierung von Ionen der seltenen Erden in skalierbare Architekturen von Quantennetzwerken bleibt jedoch aus verschiedenen Gründen eine besonders herausfordernde Aufgabe. Unter die dringlichsten Probleme fällt die typischerweise schwache Wechselwirkung von Ionen der seltenen Erden mit Licht und die nur spärlich erforschten Eigenschaften von deren Elektronenspins, insbesondere wenn sie sich in Materialien befinden, die eine hohe Dichte an Kernspins aufweisen. Zudem findet man schnell Beschränkungen in der Nanofabrikationstechnologie von seltene-Erd-dotierten Materialien im Vergleich zu anderen, herkömmlicheren Materialsystemen. Im Bestreben die relativ schwache Licht-Materie-Wechselwirkung zu überwinden, werden in dieser Arbeit verschiedene Wege präsentiert, um Ionen der seltenen Erden in photonische Resonatoren zu integrieren, welche es ermöglichen

die Licht-Materie-Wechselwirkung zu verstärken. Außerdem werden einzelne Ionen der seltenen Erden als vielseitige Messsonden in dieser Arbeit vorgestellt, die einerseits dazu benutzt werden die unmittelbare Umgebung der Ionen hinsichlicht magnetischer Felder von umliegenden Kernspins zu untersuchen, und andererseits um eine deterministische Dotiermethode zu studieren.

Die Dissertation beginnt mit der Diskussion von Experimenten an einzelnen Elektronenspins von Ceriumionen, die sich als Störstellen im YSO-Kristallgitter befinden. Durch die Interaktion der Elektronenspins mit benachbarten Kernspins, können Rückschlüsse auf die Kernspinumgebung des Ceriumions im Kristall gezogen werden. Als Einstieg wird die Methode zur optischen Isolierung von Ceriumionen präsentiert, welche grundlegend für nachfolgende Experimente ist. Danach werden bei kryogenen Temperaturen die Eigenschaften des untersuchten Elektronenspins untersucht, wobei sich die Lebenszeit des Spinzustandes auf mehrere hundert Mikrosekunden unter diesen Bedingungen erstreckt. Kohärente Kontrolle über den Elektronenspin mittels Mikrowellenstrahlung erlaubt es Kohärenzzeiten des Spins in der Größenordnung von hundert Mikrosekunden zu messen. Diese Zeitdauer ist ausreichend lang, um die dem Ceriumion nahgelegenen ^{89}Y Kernspins vom Gesamtbad aller ^{89}Y Kernspins zu isolieren. Zusätzlich erlaubt diese kohärente Interaktionsdauer die Detektion eines einzelnen ^{29}Si Kernspins, welcher nächstgelegener Nachbar zum Ceriumion im Kristallgitter ist, und der mit einer Häufigkeit von ungefähr 5% im Material vorzufinden ist. Diese Ergebnisse etablieren Ionen der seltenen Erden als Messfühler für einzelne Kernspins in deren unmittelbaren Umgebung. Da einzelne, adressierbare Kernspins als eine nützliche Ressource für Quantentechnologien betrachtet werden können, bedeutet deren Detektion mittels seltener Erden, dass eine ganze Reihe neuer Materialien für Quantenanwendungen in Frage kommen, aufgrund der flexiblen Dotierung von Materialien mittels seltener Erden. Ein Beispiel für die Nützlichkeit von Kernspins ist deren Anwendung in Quantenfehlerkorrekturalgorithmen, deren Implementierung als grundlegend für die Skalierbarkeit von Quantennetzwerken angenommen wird.

Im zweiten Teil wird eine deterministische Dotiermethode studiert. Hierfür wird die Mikroskopie an einzelnen Ionen der seltenen Erde Praseodym in einem YAG Kristall vorgestellt, welche dazu benutzt wird, eine auf einer Paul-Falle basierenden Implantationsapparatur für einzelne Ionen zu charakterisieren. Aufgrund der nennenswert hohen Konversionsrate von in YAG implantierten Praseodymionen zu fluoreszierenden Praseodymfarbzentren, können ganzzahlige Fluoreszenssignalstufen in den implantierten Stellen gefunden werden, welche die quantisierte Erzeugung von Farbzentren offenbaren. Diese Erkenntnis erlaubt es, die Entstehung der Praseodymfarbzentren genauer zu untersuchen und eine Konversionswahrscheinlichkeit zu bestimmen, die bis zu 50% erreicht. Die verwendete Mikroskopiemethode erlaubt es außerdem die örtliche Auflösung der Dotiermethode für einzelne Ionen zu beschreiben. Die Positionstreue der implantierten Stellen konnte auf 72nm und die Wiederholgenauigkeit der Positionierung in den jeweiligen Stellen konnte auf 34nm beziffert werden. Diese Ergebnisse etablieren eine neuartige und materialunabhängige Methode zur deterministischen Dotierung, die ein vielversprechendes Werkzeug für verschiedene festkörperbasierte Ansätze darstellt, welche auf die Realisierung von Quantennetzwerken ausgerichtet sind.

Im letzten Teil der Arbeit wird die Integration von Ionen der seltenen Erden in photonische Resonatoren untersucht, welche darauf abzielt, die Wechselwirkung zwischen Licht und den auf seltenen Erden basierenden Farbzentren zu verstärken, um schließlich skalierbare Licht-Materie-Schnittstellen zu ermöglichen. Hierbei werden zwei verschiedene Material-Plattformen vorgestellt, die beide eine jeweils spezifische Herangehensweise aufweisen, um eine auf seltene Erden basierte Quantennetzwerkarchitektur zu realisieren. Die erste Material-Plattform arbeitet mit dünnen Filmen bestehend aus amorphem, siliziumdotiertem Titandioxid, welche auf verschiedene Kristalle, die mit seltenen Erden dotiert werden können, abgeschieden werden. Da die abgeschiedenen Filme über einen höheren Brechungsindex als die darunterliegenden Kristalle verfügen, können sie Lichtwellenleitung unterstützen;

und es wird gezeigt, dass die Filme in photonische Wellenleiter und Resonatoren mit niedrigen Propagationsverlusten und hohen Gütefaktoren ausgestaltet werden können. Desweiteren wird die evaneszente Kopplung zwischen Lichtmoden in Resonatoren und Emittern, die sich im tieferliegenden Kristall befinden, demonstriert. In Experimenten bei kryogenen Temperaturen wird gezeigt, dass die Eigenschaften der seltenen Erden als Emitter nicht von Fabrikationsabläufen beeinträchtigt werden. Dieser Sachverhalt schafft die Grundlage für weitere resonante Studien an seltenen Erden, die an Titandioxidresonatoren gekoppelt sind. Als zweite photonische Plattform wird Lithiumniobat auf Isolator vorgestellt; ein Materialsystem, das auf eine elektro-optisch kontrollierbare Lebenszeitverkürzung der Ionen der seltenen Erden abzielt, basierend auf deren Kopplung mit photonischen Resonatoren und deren einhergehender Purcell-Verstärkung. Für dieses Materialsystem wird die Fabrikation von photonischen Strukturen, sowie deren Dotierung mittels Ionenimplantation gezeigt. Die photonischen Elemente weisen kompakte Modenvolumina auf und zeigen in anschließenden Charakterisierungen ausreichend hohe Gütefaktoren, die es prinzipiell ermöglichen Purcell-Effekt basierte Lebenszeitverkürzungen an Emittern zu messen. Die elektro-optisch modulierten Lebenszeitmessungen offenbaren den Grad der Purcell-Verstärkung und die anschließende Analyse des Dotiervorgangs erlaubt Betrachtungen zu zukünftigen Fortschritten in Richtung Einzelionendetektion basierend auf integrierten Resonatoren. Die vorgestellten Resultate ermöglichen Einsicht in eine neuartige photonische Plattform, die eine potenziell beachtenswerte Kontrolle über einzelne Knotenpunkte in einem festkörperbasierten Quantennetzwerk ermöglicht, womit sich ein besonders hohes Maß an Skalierbarkeit für Quantenarchitekturen basierend auf seltenen Erden ergibt.

Chapter 1

Introduction

A fascinating range of information processing tasks are enabled by modern computing based on the seemingly relentless progress made by computation and information technology. This unprecedented rate of advancement draws attention to what fundamentally limits information processing. Limits, defined by quantum physics, are being explored with both, scientific and technological implications.

Current research is motivated by the idea to apply a quantum mechanical system to quantum information processing tasks, an area coined "quantum information" and in this spirit, this work focuses on the palpable point of understanding the physical realization of such a quantum mechanical system from different perspectives. This boils down to the exploration of a unique material system, namely rare-earth ion doped solids and in particular to three, on first glance, mutually independent topics.

Firstly, the detection of single nuclear spins in the host crystal, by sensing them on the single spin level with a nearby rare-earth quantum emitter.

Secondly, the generation of single rare-earth dopants in host crystals, by using a deterministic single ion implantation technique.

And lastly, in order to access an ever increasing number of different single quantum systems, the effort to engineer the density of states of rare-earth dopants by means of optical resonators.

These three points constitute fundamental and ongoing trends for the broad field of solid-state emitters and they receive ample attention regarding rare-earth ion doped solids in this work. The topics merge into a coherent picture of the expansion of accessible tools and materials, and the change of paradigms, all in the light of unique rare-earth properties and directed at realizing quantum light-matter interfaces to obtain building blocks for future quantum networks.

1.1   Outline of the Thesis

This thesis is the compilation of the work done during my PhD by my collaborators and I on developing device fabrication techniques for rare-earth ion doped solids and on single rare-earth ion spin spectroscopy.

Chapter 1 gives a background for this thesis with an abridged introduction to quantum information processing, it introduces rare-earth ion physics and lastly techniques, that allow experimenting with individual ions, which represents a foundation of this work.

Chapter 2 presents a spin spectroscopic study on single Ce^{3+} ions in YSO. This comprises the optical isolation of a single cerium ion, demonstration of coherent manipulation of the cerium electron spin and the sensing of a single nearby nuclear spin.

Relevant publication for Chapter 2:

- Thomas Kornher, Dawu Xiao, Kangwei Xia, Fiammetta Sardi, Roman Kolesov, Nan Zhao, and Jörg Wrachtrup, *Sensing individual nuclear spins with a single rare-earth electron spin*, Physical Review Letters, volume 124, issue 17, page 170402 (2020)

In chapter 3, I discuss a deterministic single ion implantation technique. Using this technique, single rare-earth ions were implanted in patterns into a crystal and subsequently analyzed by optical microscopy. I describe the procedure of background free microscopy and quantify precision and accuracy. These are measures that characterize the implantation technique and are deduced from optical measurements.

Relevant publication for Chapter 3:

- Karin Groot-Berning, Thomas Kornher, Georg Jacob, Felix Stopp, Samuel T. Dawkins, Roman Kolesov, Jörg Wrachtrup Kilian Singer, and Ferdinand Schmidt-Kaler, *Deterministic Single-Ion Implantation of Rare-Earth Ions for Nanometer-Resolution Color-Center Generation*, Physical Review Letters, volume 123, issue 10, page 106802 (2019)

Chapter 4 focuses on techniques, that are developed for fabrication of optical resonators coupled to rare-earth ions. I discuss an approach based on evanescent emitter-resonator coupling based on amorphous thin film silicon doped titanium dioxide films. Additionally, an alternative take that involves directly embedded rare-earth ions in thin film lithium niobate on insulator, capable of electro-optic modulation of cavity resonances, is presented.

Relevant publication for Chapter 4:

- Thomas Kornher, Kangwei Xia, Roman Kolesov, Bruno Villa, Stefan Lasse, Cosmin. S. Sandu, Estelle Wagner, Scott Harada, Giacomo Benvenuti, Hans-Werner Becker, and Jörg Wrachtrup, *Amorphous Silicon-Doped Titania Films for on-Chip Photonics*, ACS Photonics, volume 4, issue 5, pp. 1101–1107 (2017)

1.2   Quantum Networks: From Classical to Quantum Information Processing

Progress in computational power over the last decades sprang from developments in fabrication techniques, that led to an ever-increasing density of manufactured transistors on computer chips and to the observed exponential rise in information processing power. Extrapolation tells us, that a further miniaturization will eventually meet fundamental limits in size. So, in order to maintain progress in computational capabilities, a shift in computing paradigm from conventional towards quantum computation was proposed by Richard Feynman in 1982 [1]. This proposal targeted the inability of conventional computers to solve certain problems *efficiently*, meaning without an exponential scaling in computation time. The idea of encoding information as quantum states, however, allows to project to an exponential increase in computing power as a function of the systems size and in turn opens up afore-said classes of problems to be solved. Important examples for such a problem are the factorization of large numbers, put forth by Peter Shor in 1994 [2] and simulating quantum mechanical systems.

As a consequence, an increasing effort is expended to control and study single quantum systems, in order to discover unexpected phenomena, stimulate the development of new experimental methods and ultimately to exploit them to our advantage. Prominent research fields dealing with single quantum systems are single atoms in traps, quantum dots, superconducting circuits and amongst others, single impurities in solids. They all share a fundamental property: an accessible quantum-mechanical degree of freedom [3, 4].

1.2.1   Quantum bits

In analogy to conventional computers storing information in binary bits in form of a logical 0 or 1, quantum information is stored in quantum bits, or

qubits, in form of quantum-mechanical states of individual particles. In order to grasp the advantage of the qubits' superposition states versus their classical counterparts logical states, it is sufficient to consider a simple two-level system. The two different levels, represented by two distict quantum states, can originate from a variety of physical systems. Most commonly, photons and their polarization, electrons or nuclei and their spin, Josephson junctions and their electric charge or superconducting loops and their magnetic flux, are used as physical realizations of qubits.

In Dirac notation, where $|0\rangle$ and $|1\rangle$ label the quantum states, an arbitrary superposition state is given by the wave function ψ with:

$$|\psi\rangle = c_0 |0\rangle + c_1 |1\rangle \tag{1.1}$$

The wave function amplitudes c_0 and c_1 are complex numbers with $|c_0|^2 + |c_1|^2 = 1$ and contain the quantum information, such as coherence between the states. The favorable scaling of quantum information within a registers becomes apparent for a larger number N of qubits considered. While for a two-qubit register we have four possible states,

$$|\psi\rangle = c_{00} |00\rangle + c_{01} |01\rangle + c_{10} |10\rangle + c_{11} |11\rangle \tag{1.2}$$

in the case of $N = 3$, we have $2^N = 8$ wave function amplitudes with

$$
\begin{aligned}
|\psi\rangle = \quad & c_{000} |000\rangle + c_{001} |001\rangle + c_{010} |010\rangle + c_{011} |011\rangle \\
& + c_{100} |100\rangle + c_{101} |101\rangle + c_{110} |110\rangle + c_{111} |111\rangle .
\end{aligned} \tag{1.3}
$$

The shown exponential growth in number of amplitudes for qubits translates into exponentially many locigal states a quantum computer can simultaneously explore. In contrast, a classical computer with n bits can also have 2^n possible states, but can only be in one state at a time [5].

Input qubits		Output qubits	
Control	Target	Control	Target
$|0\rangle$	$|0\rangle$	$|0\rangle$	$|0\rangle$
$|0\rangle$	$|1\rangle$	$|0\rangle$	$|1\rangle$
$|1\rangle$	$|0\rangle$	$|1\rangle$	$|1\rangle$
$|1\rangle$	$|1\rangle$	$|1\rangle$	$|0\rangle$

TABLE 1.1: Truth table for the C-NOT operation.

1.2.2 Experimental conditions for Quantum Computing

Just like a classical computer performs operations on one or more bits simultaneously in order to change its state, a quantum computer carries out quantum logic gates during the processing task. It was shown that unitary single qubit operations as well as a unitary two-qubit gate, in the simplest case the controlled-NOT (C-NOT) gate (see table 1.1), already represent a "universal" set of quantum gates [6].

While quantum computing hardware requires only coherent interactions in the considerations up to now, additional requirements for the physical system were proposed by DiVincenzo [7], targeted at achieving quantum computation in a realistic scenario and in order to benchmark different systems:

1. A scalable physical system with well characterized qubits.

2. The ability to initialize the state of the qubits to a simple fiducial state, such as $|000\ldots\rangle$.

3. Long relevant coherence times, much longer than the gate operation time.

4. A "universal" set of quantum gates.

5. A qubit-specific measurement capability.

These five criteria are largely intertwined, however, the scalability of a physical system emerged as key question and can constitute a hard limit that rules

out usage of matter systems for quantum computation. In principle, each individual qubit in a register must only interact weakly with its environment, in order to exhibit long conherence times (3). Simultaneously, qubits must interact strongly with each other for performing quantum gates (4) and also with a qubit specific driving field for initialization (2) and readout (5), in contrast to the need for high isolation from environment. The addition of a qubit to an existing network of qubits is therefore equivalent to adding noise to the system and in turn affects the networks properties. In order to meet these disparate requirements, a high degree of control is required over the physical system and more specifically, the individual qubits constituting the network. As a consequence, the study of individual qubits emerged as flourishing area of research with its own range of approaches and techniques to identify and address single quantum systems. In this work, examples for some of these approaches are given and comprise the use of micro- and nanostructures (see chapter 4) and spatial confinement (see chapter 2). In general, longer coherence times, faster quantum gates, higher fidelities and quantum error correction are examples for key aspects that are continually studied and optimized because they allow for an increased number of qubits used in a network.

Scalable quantum systems need to preserve coherent quantum states and perform quantum gates on the timescale of the relevant coherence time of the system. The constituent qubits and their operations, however, are fundamentally susceptible to errors. In order to account for uncontrolled interactions with the environment, quantum error-correction has been developed to protect quantum information. Most notably, fault-tolerant quantum computing was paved the way by the development of topological error code techniques [8, 9] that try to realize noise-resilient logical qubits comprised of numerous physical qubits with a probability of error per quantum gate up to 1%. However, while a demonstration of error-corrected logical qubits outperforming their physical constituents has not yet been achieved, coordinated efforts are being expanded towards this goal [10].

Ultimately, a quantum computer will only be worth building, if it can out-perform its classical counterpart in a certain task. This condition is closely linked to the size of the quantum network, or number of qubits the quantum computer can draw on, its gate operation fidelities and gate modalities and the problem at hand. Factorizing a large number is a good example of a relevant problem where a quantum computer can best a classical one. With a high error tolerance of 1% during gate operations on a two-dimensional lattice of qubits with only nearest-neighbor interaction, the factorization of a number with $N = 2000$ bits would require 2.2×10^8 physical qubits and a full day of operation. While an error tolerance of about 0.1% can reduce the number of physical qubits by an order of magnitude to 2×10^7, the execution time would stay unaffected [8, 11]. In any case, this surpasses even the fastest classical supercomputers of today. Heuristically estimated [12], they would not take shorter than hundreds of thousands of years for this particular task. Other estimates for usefulness of a quantum computer find $\sim 10^6$ qubits [13] as a threshold , or even 53 qubits in the most recent case [14], where the delicate choice of the problem should be taken with a grain of salt.

On the basis of DiVincenzo's list of requirements, different matter systems can be compared with each other. To what degree different systems are fulfilling these requirements serves as a measure for their matureness for quantum computing applications. Several material systems, such as super-conducting qubits, trapped ions, ultracold atoms and solid-state spins offer quantum coherence, the central resource that allows for creation of entanglement by controlled interactions [10]. In particular, solid-state spins with optical transitions are seen as promising route to obtaining scalable quantum networks. Such a network would consist of several quantum nodes in the form of the spin systems, which are connected through quantum channels, where photons carry quantum information over long distances at room temperature [15]. There is a multitude of different solid-state spin system that can serve as light-matter interface, such as various color centers in diamond

or silicon carbide, donors in silicon, quantum dots and rare-earth ions in solids [16]. The reason why rare-earth ions are considered a promising platform with potential to go beyond more established approaches, is a unique set of properties. They combine record-long coherence times in the solid-state [17], telecom band transitions for long-distance entanglement distribution [18] and integrability into photonic structures [19, 18, 20], a crucial point that implies scalability. Additionally, highly efficient creation of rare-earth ions via implantation techniques [21, 22, 23] underpins their application in quantum technologies. Specifically, the deterministic implantation with high accuracy and precision, discussed in chapter 3, shows how interwoven advances in implantation techniques and the study of single quantum systems are.

1.3 Rare-Earth Ions in Solid-State Hosts

The spectroscopy of rare-earth ions, by now a decades spanning research endeavor [24, 25, 26] , put forth a multitude of applications for modern technology. The scientific interest in unusually narrow optical spectral features and their relation to f-shell electrons initiated the widespread study of rare-earth ions in solids. This led to insights into the fundamental structure of solid-state systems by studying rare-earth probes in crystalline lattices, which up until now continues as fruitful research modality of the field. The findings resulted in technologies like rare-earth activated phosphors, once used for TV screens and nowadays in light emitting diodes, and development of some of the most prevalent laser media, such as Nd^{3+} doped materials. The example of Er^{3+} doped materials, which constitute an essential part of today's telecommunication technology in the form of optical fiber amplifiers, helps to understand the reasoning behind ongoing investigation of rare-earths. The interlinked fields of rare-earth quantum information and quantum telecommunication research represent an obvious trend towards progression of modern technologies [27, 28, 29, 18].

1.3.1   The Lanthanides

Rare-earths are chemical elements of the lanthanide series, ranging from lanthanum with atomic number $Z = 57$ to lutetium ($Z = 71$). Contrary to their naming, they are far from a rare constituent in the earth's crust, with the exception of the unstable promethium. Their abundance is comparable to that of arsenic or lead, neither of them are considered rare; cerium even is almost as abundant as copper on earth [30]. Their arrangement in the periodic table is related to their $4f$ electronic shell filling up with increasing atomic number, reflected in their electronic configuration $[Xe]6s^2 4f^n$, with $n \in \{0, \ldots, 14\}$. The fact that they all share the same bonding electrons located in the $6s$ shell translates into their chemically similar properties, such as the preferred $3+$ oxidation state. Their exceptional optical properties can be understood from the radial extent of the full $5s$ and $5p$ shells, which enclose the partially filled $4f$ shell, as shown in figure 1.1. These $5s$ and $5p$ shells act as shielding for the $4f$ electrons from environmental disturbances imposed by neighboring ions. In this isolation, optical transitions of electrons within the $4f$ shell, so-called $4f \leftrightarrow 4f$ transitions, give rise to extremely narrow optical linewidths in crystals, as small as 122Hz for Eu^{3+} [31] and even 50Hz for Er^{3+} [32]. The fact, that electrons in the partially occupied $4f$ shell are shielded by a "Faraday cage" and do not participate in chemical bond formation is also the reason why a simple approximation allows for establishing the electronic level structure of rare-earth ions. It is the application of quantum theory of atomic spectroscopy, that permits to readily construct free-ion energy levels and only a subsequent perturbation theoretical treatment of crystal-field interactions is needed to explain collective solid-state effects when the ion is in a condensed phase, what makes the rare-earth ions unique amongst solid-state systems [26].
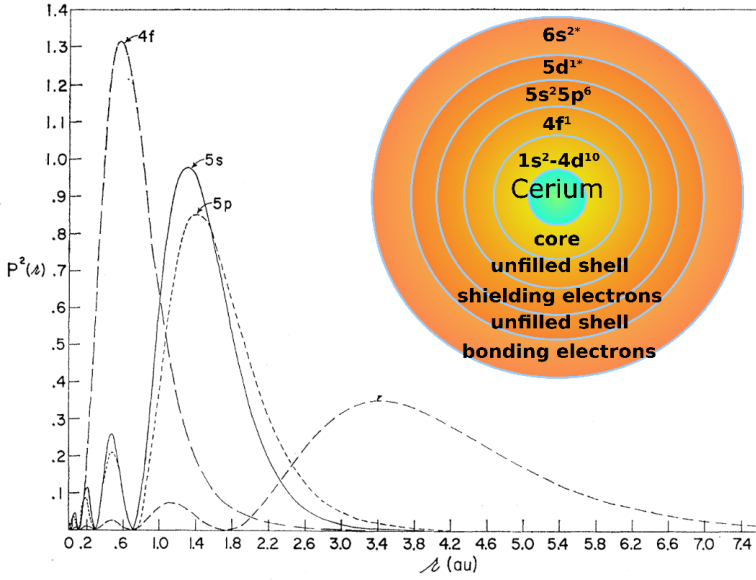
FIGURE 1.1: Radial charge densities for the $4f$, $5s$, $5p$, $6s$ electrons calculated for Gd^{3+}, taken from [33]. The $4f$ shell is well enclosed by the $5s$ and $5p$ shells and is largely unaffected by the outer $6s$ electrons. Inset: Electronic ground state configuration of cerium. Asterisked shells contain valence electrons that participate in the formation of ionic bonds for the case of Ce^{3+}

1.3.2 Electronic Level Structure of Rare-Earths

For an N-electron ion without influence of external fields, the terms of the Hamiltonian are [26]:

$$\mathcal{H} = \mathcal{H}_0 + \mathcal{H}_C + \mathcal{H}_{SO} \tag{1.4}$$

with

$$\mathcal{H}_0 = -\sum_{i=1}^{N} \frac{\hbar^2}{2m} \nabla_i^2 - \sum_{i=1}^{N} \frac{Ze^2}{r_i}, \tag{1.5}$$

$$\mathcal{H}_C = \sum_{i<j}^{N} \frac{e^2}{r_{ij}}, \tag{1.6}$$

$$\mathcal{H}_{SO} = \sum_{i}^{N} \xi(r_i)\mathbf{l}_i \cdot \mathbf{s}_i. \tag{1.7}$$

Equation 1.5 contains the kinetic energy and the potential energy of the electrons in in the field of the core of the atom, equation 1.6 denotes the Coulomb interaction between electrons and equation 1.7 represents the spin-orbit interactions, typically regarded as magnetic dipole-dipole interaction between the spin and the angular moment of the electrons with the spin-orbit coupling constant $\xi(r_i)$, which is usually determined empirically. While not absolutely accurate for rare-earth ions, the so-called Russell-Saunders, or *LS*, coupling scheme serves as starting point for momentum summation. Accordingly, the total orbital and total spin momentum operators are the sums

$$\mathbf{L} = \sum_{i=1}^{N} \mathbf{l}_i, \qquad \mathbf{S} = \sum_{i=1}^{N} \mathbf{s}_i. \tag{1.8}$$

The $4f$ states of rare-earth ions are split into manifolds with the same total angular momentum $\mathbf{J} = \mathbf{L} + \mathbf{S}$. Each J multiplet has $2J + 1$ energy levels. In the *LS* coupling scheme, J is a good quantum number and is used to identify the electronic configurations by $^{2S+1}L_J$. Trivalent rare-earth ions and their ground state configuration relevant to this work include Ce^{3+} with $^2F_{5/2}$, Pr^{3+} with $^3H_4$, Er^{3+} with $^4I_{15/2}$ and Yb^{3+} with $^2F_{7/2}$ as examples.

The crystal-field influence onto the free ion is treated as point-charge perturbation and is defined by [34]

$$\mathcal{H}_{CF} = \sum_{k,q,i} B_q^k C_q^k(i), \tag{1.9}$$

where B_q^k are crystal-field parameters, and $C_q^k(i)$ are spherical tensor operators that transform like spherical harmonics and are summed over all i electrons of the ion. The $2J + 1$ energy levels in each J multiplet are Stark split by the electrostatic crystal-field into a local crystal symmetry dependent number of levels. According to Kramers theorem, every energy eigenstate of a time-reversal symmetric system with half-integer total spin has at least one more eigenstate with the same energy. In other words, ions with odd number of electrons, so-called Kramers ions, stay at least doubly degenerate. Furthermore, the crystal-field influence can cause a mixing of wave functions with opposite parity, such as $4f^{n-1}5d^1$ states, to the $4f$ states. This makes the strictly parity forbidden $4f \leftrightarrow 4f$ transitions partially dipole allowed. Since these crystal-field perturbations are typically small, only weak electron-phonon coupling can be observed for these transitions [35], represented by narrow optical linewidths and long excited-state lifetimes, characteristic for rare-earth ion spectroscopy. The interest within the field of quantum information in rare-earth ions builds exactly on these properties, namely the high degree of isolation from environmental effects, which is closely related to long coherence times of systems. However, the low interaction with environment and the access to a single quantum system, which is required to reliably measure said system, are two sides of the same coin.

1.3.3 Previous Work on Single Rare-Earth Ions

Probing single rare-earth ions has emerged as research direction over the last years [36, 37, 38, 39, 19, 18], with a variety of techniques, that grant access to previously unaccessible single quantum systems. The identification of a single rare-earth ion proved to be challenging based on the long excited-state lifetimes of the characteristic $4f \leftrightarrow 4f$ transitions. Typically, these optical lifetimes range between 100μs-10ms [40]. This corresponds to a rather low flux of photons that can in principle be collected in order to observe single ion signatures.

To alleviate experimental conditions, the first definitive proof of single rare-earth ion detection [36] exploited the energetically higher $4f5d$ states of Pr:YAG due to the much shorter lifetime of these states. This approach, sometimes referred to as the "brute force approach" within the rare-earth ion community, requires broadband UV photons to be detected. This was realized by optical upconversion, where the $4f$ electron is promoted to states outside the $4f$ shell and can then decay back within nanoseconds under phonon sideband assisted emission of a photon. Finally, based on the increased emission rate of the rare-earth ion, sufficient signal can be collected in a confocal microscope [41]. The main function of the confocal microscope is the additional spatial filtering it applies to the detected signal, which can be further enhanced by microscopy of nanocrystals as demonstrated in [36, 39]. Apart from spatial filtering, spectral filtering with optical filters to reduce background fluorescence and most importantly the efficient extraction of fluorescence light from the ion require special attention for this technique. This does not only include the use of optical elements with minimum loss in the spectral range of the signal photons, but also covers micron-sized photonic structures such as a solid immersion lense (SIL) [42]. SILs fabricated directly onto the surface of a crystal can cancel refraction and total internal reflection of excitation and emission light fields based on the index difference between the refractive index of the crystal and the immersion medium of the microscope objective lens. This index difference otherwise causes a reduction of resolution and collection efficiency of the microscope, by effectively reducing the numerical aperture of the microscope objective lens. In a similar fashion, single Ce:YAG [37] was detected and subsequently used for coherent microwave manipulation of its spin [43] and for coherent population trapping [44].

A fundamentally different approach to access single rare-earth ions was presented in [38], where a single electron transistor (SET) is used to detect single photoionized erbium ions in silicon. The SET functions as a charge sensor, which detects photoionization events of erbium when a narrow band laser is tuned into resonance of an individual ion's $^4I_{15/2} \leftrightarrow ^4I_{13/2}$ transition. This

was the first demonstration, where a single rare-earth ion was selected optically in the spectral domain. Later, it was followed by [39], where a highly stabilized laser was used to excite a single Pr:YSO ion, located in a nanoparticle (spatial confinement) and spectrally filtered by excitation with the narrow band laser. The experiment marks a direct optical detection of single ions via a $4f \leftrightarrow 4f$ transition and it was achieved by collecting signal photons with the help of a SIL.

Further successful detections of single rare-earth ions were all recently achieved by coupling either single Nd:YVO [19] or single Er:YSO [18] to a nanophotonic resonator. Selection of the indivudual ions was achieved by narrow band excitation lasers in the spectral domain. These integrated nanophotonic structures serve as an efficient light-matter interface, that allows to collect a well-defined optical mode as signal and they provide an enhancement of the photon emission rate. They grant access to originally long-lived $4f \leftrightarrow 4f$ transitions by speeding up the excitation-emission cycle by up to almost three orders of magnitude [18]. The development of single shot read-out schemes, based on cycling transitions of resonator-coupled single ions [20, 45] are the most recent and novel demonstrations by this approach. Most importantly, the integration of rare-earth ions in light-matter interfaces presents a strong shift towards scalable architectures for quantum information technology, further discussed in chapter 4.

Chapter 2

Rare-earth Electron Spin Spectroscopy on Single Ce^{3+}:YSO

In this chapter, I will summarize the work on single cerium ions in YSO crystals. Starting out by motivating the study and introducing the basic system properties, the optical isolation of a single Ce^{3+} ion in YSO is discussed with focus on the experimental microscope setup and the optical initialization of the single Ce^{3+} electron spin. Based on the single spin access, coherent spin manipulation by microwaves is shown and used to perform sensing of environmental nuclear spins, native to the host crystal. I conclude with results showing the detection of a single ^{29}Si nuclear spin coupled to a nearby Ce^{3+} electron spin.

2.1 Introduction

Hybrid quantum systen have demonstrated exceptional properties [46, 47, 16] for quantum memory applications. These systems are comprised of both, electron spin and nuclear spin and thus bring together unique properties.

Here, typically long-lived nuclear coherences can be accessed by the read-out electron spin. This enables active quantum processing when handled on the single spin level, for example in quantum error correction schemes [48]. Individual environmental nuclear spins, the key resource at hand, were detected only in dilute nuclear spin bath host materials so far, such as diamond [49, 50, 51, 52, 53], silicon carbide [54] and silicon [55]. Prior to an implementation of quantum error correction in the rare-earth ion system, access to single nuclear spins needs to be demonstrated. Access to a single nuclear spin was shown for single rare-earth ions with an internal hyperfine structure and their potential as a quantum memory has been demonstrated [39, 56, 20]. However, the sensing of several environmental nuclear spins proximal to the rare-earth electron spin is shown in the following and denotes another potentially powerful approach to a memory resource. Additionally, the detection of a single external nuclear spin closeby the ancillary rare-earth electron spin is revealed.

A previous study on single Ce^{3+} ions in a YAG crystal identified the dense nuclear spin bath of the crystal as the limiting factor for the electron coherence time [43], quantified in Hahn spin echo experiments to $T_2 = 200$ns. The short coherence time likewise affects the sensing capabilities of the electron spin and generally limits it to sensing high frequencies above $1/T_2$ and prevented sensing of nearby individual nuclear spins. A host material with relatively low magnetic noise, namely the YSO crystal, was therefore chosen for the study of the nuclear spin environment of individual Ce^{3+} electron spins. Previous work on Er^{3+} [57] and Eu^{3+} [58] located in the same host crystal had shown superhyperfine interaction between ^{89}Y^{3+} and the respective rare-earth ion in ensemble measurements. Extending these observations to the single spin level in the case of ^{29}Si is demonstrated in the following.

2.2 Yttrium Orthosilicate: The Host Crystal

Yttrium orthosilicate (Y_2SiO_5, YSO) is a low symmetry crystal with monoclinic biaxial structure, that belongs to the C2/c (C_{2h}^6) space group. The first growth of this crystal was reported in the year 1967 [59] and later characterized by [60]. These early reports mentioned growth temperatures of around $400°C$ and reported the low temperature set of lattice parameters, listed in table 2.1. An alternative version of the crystal structure was reported in [61, 62] for a Cr:YSO crystal, grown at high temperature by the Czochralski technique in a high-frequency heated iridium crucible. Only the high temperature grown version of the crystal is considered hereafter for the study of Ce^{3+} ion impurities, as this is the most common method to grow YSO crystals nowadays and was used for all our studied samples. The crystallographic properties of the low and high temperature grown versions are summarized in table 2.1. The unit cell of the crystal consists of eight molecular units of Y_2SiO_5 and the high temperature version is shown in figure 2.1.

Method	a (Å)	b (Å)	c (Å)	β (deg)
Low temperature [60]	10.41	6.72	12.49	102.65
High temperature [62]	14.37	6.71	10.39	122.17

TABLE 2.1: Experimental lattice parameters for YSO grown with different methods.

There are two crystallographically distinct sites for Y^{3+}, labelled Y1 and Y2. They are discriminated by their oxygen coordination, where Y1 bonds to seven oxygen ions (Y1-O7) and Y2 bonds only to six oxygen ions (Y2-O6). Both Y^{3+} sites have C_1 point symmetry, a point group with practically no symmetry. When doped into YSO, rare-earth ions substitute yttrium in the crystal with 3+ oxidation state, hence no charge compensation is needed. The crystal was used for demonstrations of particularly narrow homogeneous [63] and inhomogeneous [64] linewidths, which can be attributed to the small magnetic moment of yttrium. Table 2.2 lists the non-zero nuclear
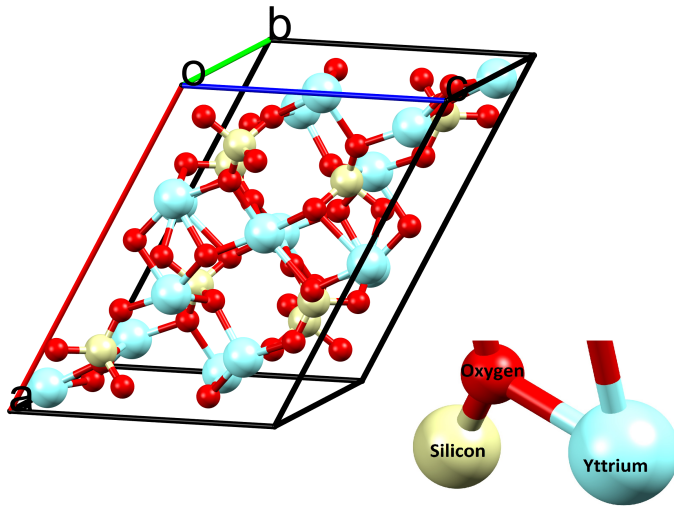
FIGURE 2.1: Crystal structure of yttrium orthosilicate after
[62]. Yttrium, oxygen and silicon ions are displayed in light
blue, red, and beige, respectively.

spin isotopes native to YSO and their relevant isotope data.

Isotope	Mass (u)	Abundance (%)	Nuclear spin (I)	Magnetic moment (μ/μ_N)
^{89}Y	89.9	100	$^1/_2$	-0.137
^{29}Si	29.0	4.68	$^1/_2$	-0.555
^{17}O	17.0	0.038	$^5/_2$	-1.894

TABLE 2.2: Isotope data about naturally occuring isotopes
native to YSO with non-zero nuclear spin. Taken from [65].

2.3   Optical Isolation of Single Ce^{3+}:YSO

In the YSO crystal, 95% of trivalent cerium substitutes Y^{3+} at the seven-oxygen-coordinated Y1-O7 site. The remaining 5% Ce^{3+} substitute at the

Y2-O6 site. These figures are estimated from EPR studies on the Lu_2SiO_5 (LSO) crystal [66], which is isomorphic to YSO, hence they share the same chemical formulation, space group and unit cell dimensions [67]. These two cerium sites have significantly different optical properties in YSO. For the cerium at the Y1-O7 site, a blue-shifted characteristic emission with respect to the cerium at the Y2-O6 site is observed [68], shown in figure 2.2 a).
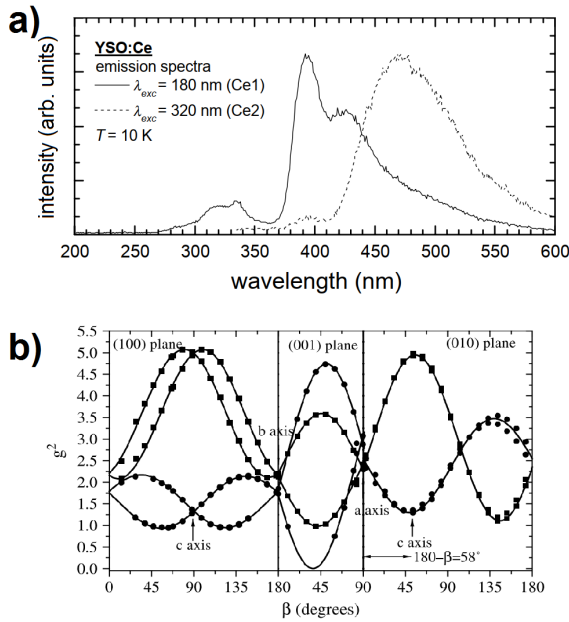

FIGURE 2.2: a) Low temperature photoluminescence spectra of the two cerium sites in YSO, taken from [68]. b) Angular variation of g^2 for different crystalligraphic planes for Ce^{3+} in LSO, taken from [66]. The squares depict experimental data for cerium in site Y1-O7 and the circle for cerium in site Y2-O6. Split lines represent the magnetically inequivalent sites for each of the crystallographic sites.

Consequently, their optical signal can be seperated effectively. Additionally, they also exhibit different magnetic properties, found in EPR experiments

[66] and shown in figure 2.2 b). We can therefore exclude the Ce^{3+} ions located at the six-oxygen-coordinated site from further considerations. The crystallographically unique Y2-O7 site however, consists of a pair of magnetically inequivalent sites, represented by a line splitting of the EPR data shown in figure 2.2 b).

2.3.1   Electronic Level Structure of Ce^{3+}:YSO

The Ce^{3+} :YSO system can be described by the following Hamiltonian

$$\mathcal{H}_{Ce} = \mathcal{H}_0 + \mathcal{H}_{SO} + \mathcal{H}_{CF} \tag{2.1}$$

in the absence of a magnetic field. As cerium has only isotopes with zero nuclear spin, there is no hyperfine interaction to be taken care of. Also, with only one electron left in the $4f$ shell, the Coulomb interaction between unpaired electrons can also be excluded from the total Hamiltonian. Based on the $4f^1$ configuration of Ce^{3+} , the shielded $4f$ states consist of two electronic multiplets $^2F_{5/2}$ and $^2F_{7/2}$, which are seperated by roughly 2000cm^{-1} [69]. These multiplets are further split by crystal field interaction into three ($^2F_{5/2}$) and four ($^2F_{7/2}$) Kramers doublets, respectively. The lowest two $5d$ Kramers doublets have an energy difference of approximately 6000cm^{-1}, taken from the excitation peak energies in [68] and information about the zero-phonon line (ZPL) [69]. The schematic energy level structure of Ce^{3+} :YSO is shown in figure 2.3.

The $5d$ states, often also referred to as $5d$ band as indicated in figure 2.3, are not shielded from crystal field perturbation and thus undergo strong interaction with phonons. This manifests in the phonon sideband assisted emission, which is dominated by parity-allowed electric dipole transitions and observed in the fluorescence spectrum (taken with Princeton Instruments, Acton SpectraPro 2300i), when excited with a laser of 355nm wavelength, as shown in figure 2.4 a). For this experiment, a 0.01% doped Ce:YSO crystal
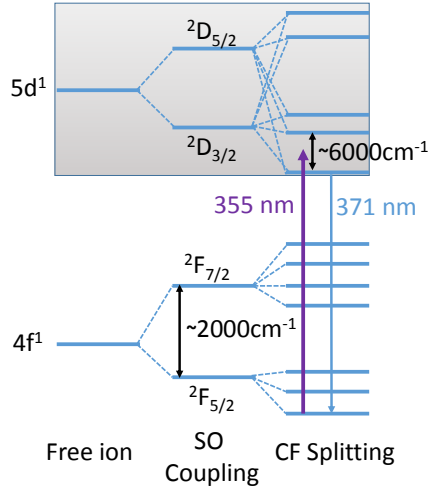
FIGURE 2.3: Schematic energy level structure of Ce^{3+} in YSO.

cooled to cryogenic temperature of 8K was excited with a home-built picosecond pulsed 355nm laser, capable of promoting the $4f$ electron of Ce^{3+} into the $5d$ band. For this measurement, a narrow multiband notch filter for 355nm and 532nm wavelength was used as a dichroic mirror, which explains the gap around 532nm in the spectrum. As previously reported by [69], the ZPL of Ce^{3+} ions in YSO is expected at 371nm. In figure 2.4 b), a high-resolution spectrum of the 0.01% doped Ce:YSO crystal at 8K confirms this observation. A resonant CW excitation scheme based on the ZPL can in principle yield a spectral filtering by the narrowband excitation laser and thus reduce background fluorescence and the corresponding noise in samples with high Ce^{3+} concentration. However, photostable emission of Ce^{3+} in YAG crystals under CW excitation was only found in conjunction with a special annealing treatment in a reducing atmosphere of argon (95%) and hydrogen (5%) [44], yet to be shown for YSO.

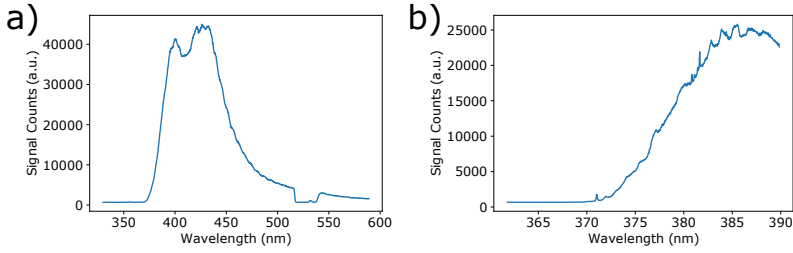A typical fluorescence decay measurement taken on the 0.01% doped Ce:YSO

FIGURE 2.4: Fluorescence spectra of 0.01% Ce^{3+} :YSO, taken at low temperature (8K). a) Low-resolution spectrum showing the broad phonon sideband assisted emission. b) High-resolution spectrum showing the ZPL at 371nm.

is shown in figure 2.5. By fitting a single exponential decay, a fluorescence lifetime of the lowest $5d$ state of $\tau_{Ce:YSO} = 37$ns is found, in good agreement with [70]. This short lifetime translates into high emission rate of photons and through efficient photon collection, it enables optical detection of single Ce^{3+} ions.

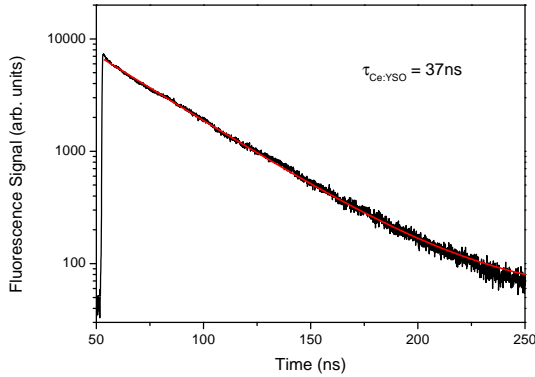
FIGURE 2.5: Fluorescence lifetime measurement of Ce^{3+} in YSO under pulsed 355nm excitation.

2.3.2 Confocal Microscope Setup

The experiments for single Ce^{3+} ion detection were carried out in a home-built laser scanning confocal microscope setup, shown in figure 2.6. Samples were cooled to cryogenic temperatures in a vacuum-pumped cold-finger cryostat (CryoVac, Konti-Cryostat Type Micro) with optical access. On the cold-finger, samples were mounted either directly or on top of a permanent magnet. During operation of the cryostat, the cold-finger is connected to the heat-exchanger, which is fed by liquid helium, thus thermalizing cold-finger and sample to cryogenic temperatures. The actual temperature measurement is taken on the heat-exchanger, which typically yields a slight offset to the actual sample temperature due to limited cooling power of the heat-exchanger and finite heat conductivity of the cold-finger/sample- or cold-finger/manget/sample-stack. The heat-exchanger is mouned on a motorized 3D stage, which covers 10mm x 10mm x 10mm for rough positioning. For spatial high-resolution fluorescence imaging, the objective lens of the confocal microscope is mounted within the cryostat vacuum chamber on a 3D piezo translation stage (NPoint, NPXY100Z25-264) capable to position throughout 100μm x 100μm x 25μm with nanometer resolution.
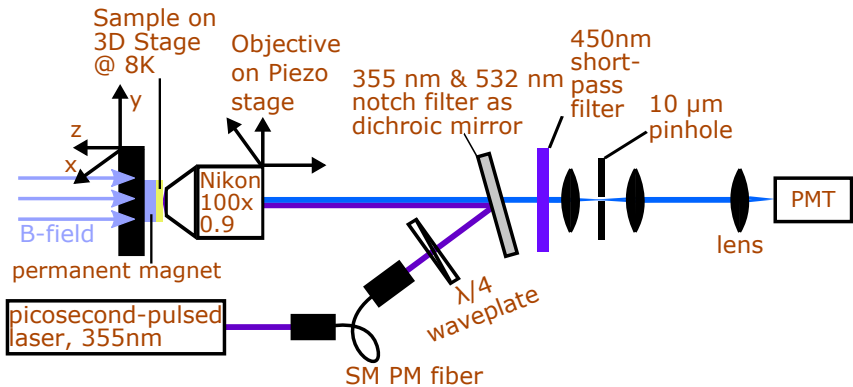

FIGURE 2.6: Sketch of the low temperature laser scanning confocal microscope setup. PMT: Photomultiplier tube. SP PM fiber: single-mode polarization maintaining fiber.

Optical excitation of Ce^{3+} :YSO was done with a home-built 355nm wavelength pico-second-pulsed laser. This laser was assembled from a dye-laser cavity, which is synchronously pumped by a 2W output power 532nm picosecond-pulsed laser (Vanguard, Spectra-Physics). Its layout is depicted in figure 2.7. For synchronous pumping, the dye-laser cavity length is adjusted to match the 76MHz repetition rate of the pump laser with a computer controlled piezo linear precision positioner. By pumping Pyridin 1 dye, radiation emitting at 710nm can be extracted from the laser. In order to obtain maximum output power and facilitate externally controlled pulse extraction from the laser simultaneously, the partially transmissive output coupler of the dye-laser cavity was omitted and replaced by a highly reflective mirror. Additionally, an externally triggerable Quartz AOM was introduced into the dye-laser cavity that allowed for intra-cavity extraction of pulses. Extracted pulses were subsequently sent through a BBO doubling crystal and converted to second harmonic 355nm wavelength pulses. By coupling the beam into a single-mode polarization maintaining fiber (Thorlabs, PANDA PM-S350-HP), a spatial mode cleaning was achieved. After passing through a $\lambda/4$ waveplate and reflecting off the multiband notch filter for 355nm and 532nm wavelength, which is used as a dichroic mirror, the excitation light is focused onto the sample by a high numerical aperture objective lens (Nikon, LU Plan Fluor, 100x/0.90NA, 1.0mm working distance). Fluorescence is collected by the same lens and passed through a 450nm short-pass filter, in order to reject parasitic emission from other impurities found in the YSO crystal. Common residual impurities in yttrium-based crystals like YSO are for example other RE ion species. The fluorescence signal was further filtered by a 10μm sized pinhole for an increase in depth resolution, characteristic for a confocal microscope. Finally, single fluorescence photons are collected by a Photomultiplier Tube (Hamamatsu, H10682-210) and detection events are counted with data acquisition hardware (NI-PCIe-6323).
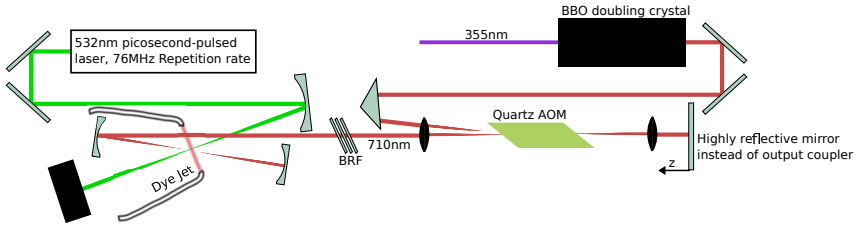
FIGURE 2.7: Sketch of the synchronously pumped dye laser. The highly reflective mirror replacing the output coupler of the dye laser is mounted on a piezo translation, which allows to fine adjust the cavity length, in order match the 76MHz repetition rate and obtain maximum peak intensities for efficient doubling. BRF: Birefringent filter.

2.3.3 Laser Scanning Fluorescence Imaging of Ce^{3+}:YSO

In laser scanning fluorescence imaging, the laser focus is scanned in as small as nanometer-sized steps throughout the sample and at each position the fluorescence signal is acquired for a certain amount of time (time bin). The typically used single photon detectors allow for retrieving a photon count per time bin and based on the particle nature of light, their noise is following a Poissonian distribution. This so-called shot noise exhibits a standard deviation which is equal to the square root of the average number of detected photons N. Accordingly, the signal-to-noise ratio is given by $SNR = N/\sqrt{N} = \sqrt{N}$. Maximizing N therefore allows for detection of small signals like the fluorescence of a single rare-earth ion.

The photon collection efficiency from a color center within a material with refractive index n is significantly reduced by refraction at the flat air-crystal interface. Due to the high refractive index of YSO with $n_{YSO} \approx 1.8$ in our case, the effictive maximum angular semi-aperture θ of the used air objective lens with numerical aperture of NA $= 0.9$ can be inferred by Snell's law $n_{YSO} \sin \theta = $ NA, resulting in $\theta \approx 30°$, for the case of a flat polished YSO crystal surface as depicted in figure 2.8 a). In contrast, if the light emitted from a point defect is propagating perpendicular to the spherically shaped
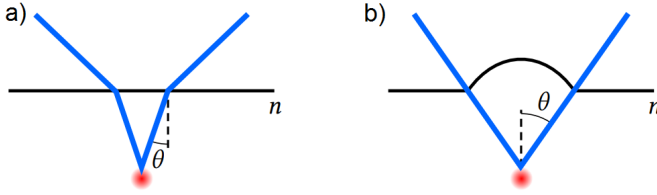
FIGURE 2.8: a) Refraction of light rays at the interface between air and a plane surface of a crystal with refractive index n. b) Refractionless transmission of light rays at the air-crystal interface in the presence of a SIL.

surface of a solid immersion lens (SIL), refraction is inhibited and the full NA-limited angular semi-aperture of the objective lens can be used for photon collection, maximizing the collection efficiency for the objective lens in use, as shown in figure 2.8 b). In the case of NA = 0.9, the lens can collect light for angles $\theta \leq 64°$. Equally as important is the fact, that the SIL improves the microscope magnification by factor n, essential for spatial isolation of single color centers.
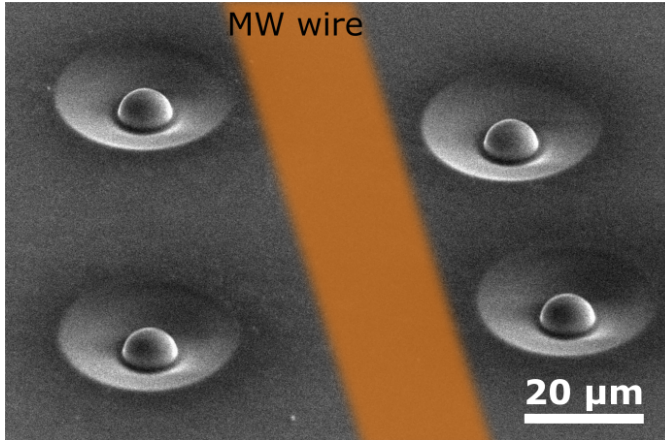

FIGURE 2.9: SEM image of SILs on a YSO crystal surface. The position of the microwave (MW) copper wire used for spin manipulation is indicated by an orange stripe.

In the context of single emitters, SILs were originally used in conjunction
with quantum dots [71], and later monolithic versions of macroscopic SILs
were also applied to color centers in diamond [72]. Their miniaturized mi-
croscale versions [73, 44, 74] emerged as versatile tool, which was used for
various crystals. Main contribution to their widespread use is the material
independent fabrication method based on FIB milling. Here, a gallium ion
beam with typically 30keV energy is focused onto the polished surface of
a crystal and is used to sputter material. When done in a controlled man-
ner, hemispherically shaped lenses can be carved into the bulk material, as
shown in figure 2.9 for a YSO crystal, fabricated with a FIB from FEI (Helios
Nanolab 600). The shown SILs have a diameter of 10μm. After gallium ion
sputtering, the YSO crystal was dry etched in argon plasma in order to re-
move the near-surface gallium content, that stays as residual impurity after
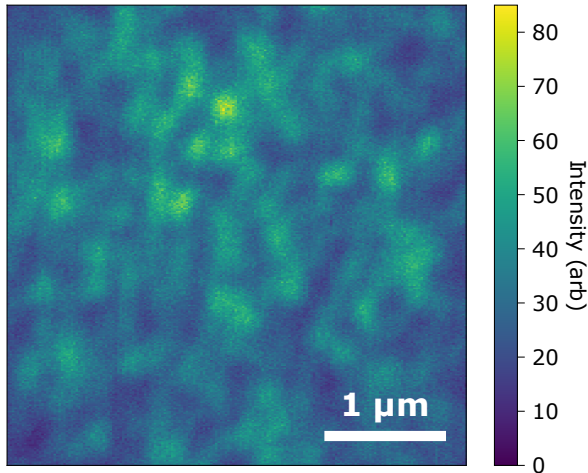the FIB process and can cause background fluorescence.

FIGURE 2.10: Laser scanning confocal scan of cerium cen-
ters under pulsed 355nm laser excitation. The scan was
taken at the focus of a SIL, 5μm below the surface.

Performing laser scanning fluorescence microscopy in the focus of the YSO
SIL at a depth of 5μm below the surface, yields a scan as shown in figure

2.10. The ultra-pure YSO crystal used for this scan was purchased at Scientific Materials Corp. Bright spots in the scan correspond to fluorescent cerium ions. From the scan it becomes apparent, that even in the purest YSO crystals, cerium is an unavoidable impurity occuring in significant concentrations considering confocal microscopy application. Residual cerium concentration in this crystal is estimated at 0.3ppb. In general, native rare-earth ion impurities, specifically the high cerium concentration is also the main contribution to background signal throughout the following experiments and can result in more than one single Ce^{3+} ion to be probed within the focal volume. Possible ways to reduce the negative impact of high impurity concentration of cerium in the crystal are the growth of even purer samples, which was not at hand for this experiment, or the use of superresolution microscopy techniques, discussed in the following.

2.3.4 Superresolution Microscopy of Ce^{3+}:YSO

The field of microscopy was revolutionized by techniques that surpass the diffraction limit, such as stimulated emission depletion (STED) [75] or stochastic optical reconstruction microscopy (STORM) [76]. These superresolution techniques allow for resolving color centers, such as fluorescent dye molecules, with spacings much closer than the Abbe limit [77]. Application of these techniques to photostable color centers in crystalline solid state hosts, such as the nitrogen-vacancy center in diamond [78, 79] opens up all-optical addressing of densely packed single quantum systems for quantum information processing. This was underlined by a demonstration of the highest resolution in all-optical imaging of fluorescent centers with STED microscopy on nitrogen vacancy centers [80]. In the context of quantum information processing, the spin of the nitrogen vacancy center represents the quantum resource and its properties are of substantial importance. Hence, the conservation of the spin properties is a prerequisite for the application of superresolution techniques in the field of quantum information processing and was confirmed for STED on nitrogen vacancy centers [81].

STED microscopy is a variant of fluorescence microscopy, where fluorophores or color centers are excited with light of a specific wavelength for example, but they can also be brought into the excited state spontaneously, by heat or a different mechanism. An essential property for the system in question to have, is the possibilty to induce the transition from excited state to ground state by light. This stimulated emission is used to deplete the fluorescent state and requires the depletion light intensity to be much larger than the saturation intensity of the transition, in order to efficiently depopulate the excited state [82]. By controlling the spatial intensity distribution of the depletion light field, the fluorophores or color centers can be selectively brought into the ground state. Typically, experimental realizations use donut shaped depletion light fields, where only the very center is not being depleted. In principle, arbitrarily sharp regions can be created with this method, which in principle follows a square root law of the saturation level for the resolving power of the microscope[82, 83]. Recently, deviations from this law were found and related to a competing depletion mechanism in form of excited state absorption [84]. In general, a complete depletion of the excited state is not required for microscopy, as long as the ground state population is large enough to be distinguished from its sharp counterpart [82].

In our experiments, the STED microscope relies on an excitation laser with a fundamental Gaussian profile of the beam superimposed with the depletion laser, that has the form of a donut-shaped beam. The experimental setup is depicted in figure 2.11. For STED on Ce^{3+}:YSO, a picosecond-pulsed 355nm wavelength excitation and a picosecond-pulsed 532nm wavelength depletion laser was used, as indicated in figure 2.12. For the picosecond-pulsed 532nm depletion, the pump laser of the home-built sychronously pumped dye laser was used. The spectral detection window for Ce^{3+}:YSO was contained to the range between 370nm and 450nm by interference filters. The experimental realization of the STED microscope had both lasers passing through their respective single mode polarization maintaining optical fiber. The donut-shaped depletion beam was then realized by sending the 532nm
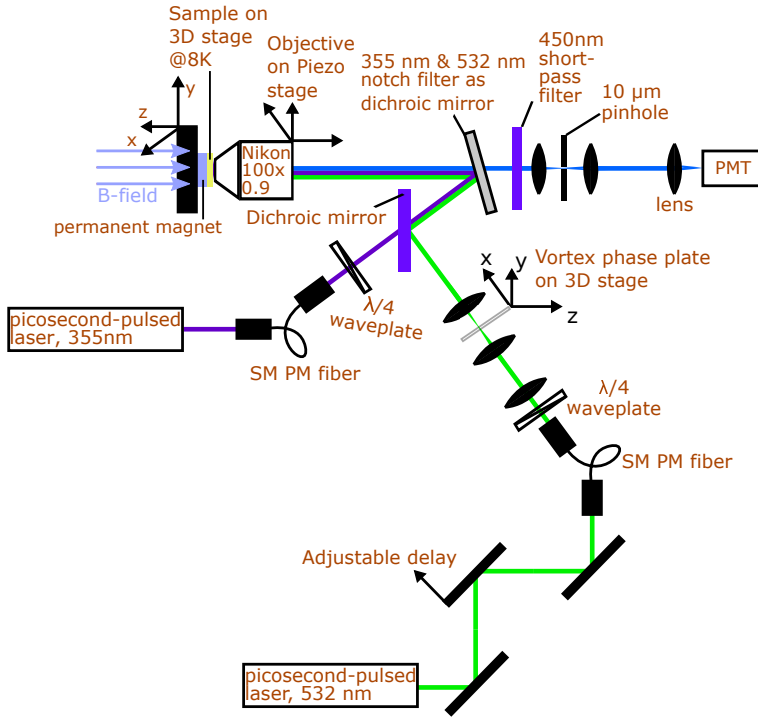
FIGURE 2.11: Sketch of the low temperature laser scanning confocal STED microscope setup. PMT: Photomultiplier tube. SP PM fiber: single-mode polarization maintaining fiber.

laser through a vortex phase plate of charge 1 (from RPC Photonics) and combining both beams on a dichroic beam splitter, a narrow multiband notch filter for 355nm and 532nm wavelength.

Performing laser scanning fluorescence superresolution microscopy in the focus of the YSO SIL at room temperature yields scans such as the one shown in figure 2.13 on the right-hand side. Under picosecond-pulsed excitation and depletion, the natural Ce^{3+} impurities in the YSO crystal showed stable emission. In order to obtain the highest increase on optical resolution, laser powers had to be adjusted with respect to each other. The depletion
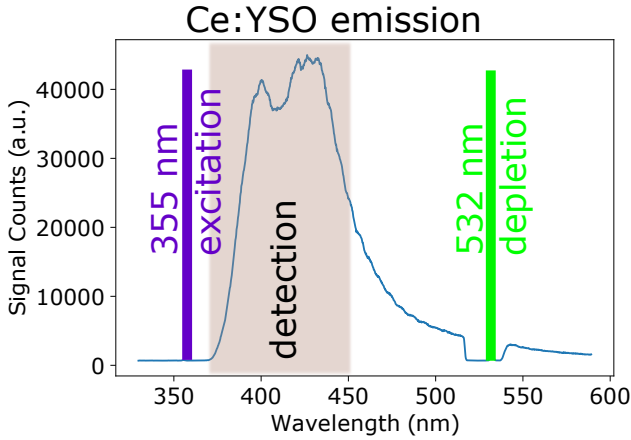
FIGURE 2.12: STED microscopy of Ce^{3+}:YSO. The spectrum of Ce^{3+}:YSO is shown, superimposed with the spectral position of the picosecond-pulsed 355nm excitation laser, the picosecond-pulsed 532nm depletion laser and the spectral detection window for Ce^{3+} fluorescence.

beam power was 45mW in front of the objective lens and the 355nm excitation was kept well below saturation threshold of the cerium ions. Also, the 532nm laser pulse arrival time had to be delayed with respect to the 355nm excitation pulse, in order to not attempt depletion of the population of the 5d excited state of cerium before it is excited in the first place. The timing was performed by adjusting the lengths of optical paths. Also, overlapping of the two laser beams and adjusting the divergence of both beams with respect to each other, such that the two wavelengths share the same focal plane after passing through the objective lens was required for increasing the spatial resolution of the microscope. This need is based in the chromaticity of the microscope objective in the UV and visible range spectral range, leading to focal depth differences on the order of several micrometers. The obtained microscope resolution for confocal STED microscopy and conventional confocal microscopy was assessed by measurement of the PSF. This was done by a two-dimensional Gaussian fit to several Ce^{3+} centers for both scans,

shown in figure 2.13. The average FWHM of the conventional confocal microscope amounted to 262nm. With the STED depletion beam, the confocal STED microscope achieved an average FWHM of 122nm. This corresponds to a resolution increase of factor 2.
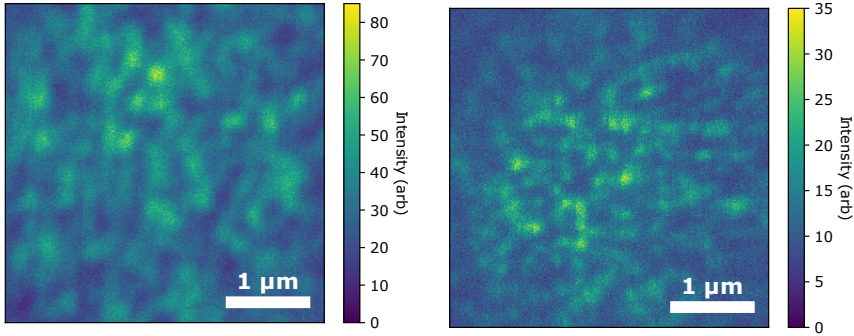

FIGURE 2.13: Two different confocal laser scans. Left image was taken without depletion laser, right image was taken with depletion laser.

For cerium in another host crystal, namely Ce^{3+} in YAG [84], STED microscopy was already demonstrated with CW laser excitation and the observed resolution scaling was slower than the expected inverse square-root dependence on the depletion laser intensity. This anomaly was linked to ESA of Ce^{3+} and to interaction with nonfluorescing crystal defects in the proximity of the single Ce^{3+} center and can be seen as competing depletion mechanisms to stimulated emission. This study was performed at room temperature, and hence no information about the preservation of the spin properties could be reported. In the picosecond-pulsed STED experiments with Ce^{3+} :YSO at cryogenic temperatures however, no magnetic resonance signals could be acquired while the high power 532nm depletion laser was used. That means, while the resolution enhancement found with STED microscopy can in principle reduce the background noise significantly, it is not applicable in conjucntion with spin manipulation. In analogy to prior findings made with the similar YAG host crystal, the high power depletion laser

for Ce^{3+} :YSO is preventing the optical spin initialization and readout most likely by ionisation of Ce^{3+} through ESA and through interaction with surrounding traps. All further spin spectroscopic experiments were thus conducted with the standard confocal microscope.

2.4 Spin Initialization and Optical Detection of Ce^{3+} Spin Resonance

Ce^{3+} in YSO is a spin $S = 1/2$ system and under application of a magnetic field the Hamiltonian presented in equation 2.1 is extended to

$$\mathcal{H}_{\text{Ce}} = \mathcal{H}_0 + \mathcal{H}_{\text{SO}} + \mathcal{H}_{\text{CF}} + \mathcal{H}_{\text{B}}. \tag{2.2}$$

The additional term $\mathcal{H}_{\text{B}}$ is due to the Zeeman interaction and is given by

$$\mathcal{H}_B = \frac{\mu_B}{\hbar} \boldsymbol{B} \cdot \boldsymbol{g}_{\text{eff}} \cdot \boldsymbol{S}, \tag{2.3}$$

where $\boldsymbol{B}$ is the magnetic field, $\boldsymbol{S}$ is the spin operator and $\boldsymbol{g}_{\text{eff}}$ the effective g-factor of Ce^{3+} . In the external magnetic field, the seven $4f$ Kramers doublets split into 14 non-degenerate energy levels and the five $5d$ Kramers doublets split into 10 non-degenerate energy levels. In the following, only the transitions between the lowest split $5d$ doublet, $\left|5d^1 \downarrow\right\rangle$ and $\left|5d^1 \uparrow\right\rangle$, and the lowest split $4f$ doublet, $\left|4f^1 \downarrow\right\rangle$ and $\left|4f^1 \uparrow\right\rangle$, are considered for optical spin initialization. When the magnetic field is aligned in parallel to the optical excitation beam, it was shown for Ce^{3+} :YAG that optical spin-flip transitions between these four levels show different oscillator strenghts under circularly polarized excitation light [37]. Based on the high symmetry of the YAG crystal, the 14 crystal field parameters for $4f$ and $5d$ states of Ce^{3+} :YAG could be extracted from optical measurements [86], and hence it was possible to
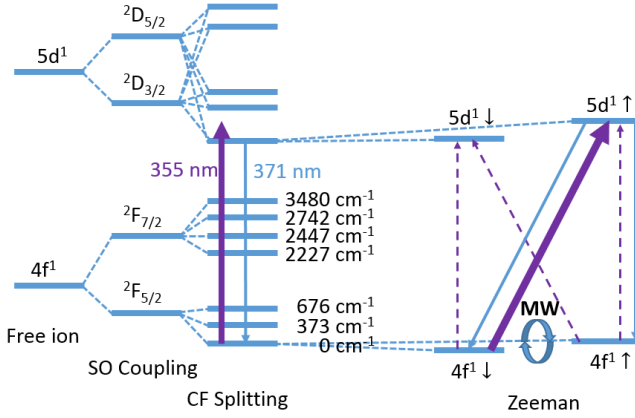
FIGURE 2.14: Electronic level structure of Ce^{3+} ion in YSO crystal. Purple arrows indicate laser excitation and blue arrows fluorescence. Under circularly polarized excitation light, directed along the same axis as the applied external magnetic field (along the b-axis of the crystal), different strengths of optical transitions between the lowest $4f$ level and the lowest $5d$ level are indicated by different widths of arrows in the right part of the depiction. Calculated $4f$ energy level data is taken from reference [85].

quantify the different dipolar oscillator strengths of circularly polarized optical transitions.

In the experiment at hand, a spin initialization of Ce^{3+}:YSO was investigated. To successfully initialize the spin, the spin-flip transition $|4f^1 \downarrow\rangle \rightarrow |5d^1 \uparrow\rangle$ for example needs to exhibit the strongest optical dipole moment under σ^+ circularly polarized excitation light out of the four possible transitions, as indicated in figure 2.14. In this case, a selective excitation into the $|5d^1 \uparrow\rangle$ level can be achieved. Since the corresponding radiative decay ends up in both $4f$ ground state spin levels with equal probability, a repeated excitation of the spin-flip transition can be used to polarize the spin in this

example into the $|4f^1 \uparrow\rangle$ state. For the Ce^{3+} :YSO system, cryogenic temperatures are needed to maintain the spin polarization in the $4f$ state for an appreciable amount of time. Circularly polarized excitation light was directed along the b-axis of the YSO crystal in initialization experiments. In order to probe these polarization selection rules, the fluorescence signal of Ce^{3+} at a temperature $T = 7.8$K is collected as a function of the laser pulse number, shown in figure 2.15. The initialization measurements capture the dynamic evolution of the fluorescence signal and show a drop with increasing number of laser pulses. This behavior reflects the optical pumping of the spin into the optically 'dark' state. Initialization contrasts are varying for different Ce^{3+} ions in the sample and were found to range between 5% and 15%, depending on the local background. For the initialization measurements, a laser pulse repetition rate of 10MHz was used. Also, in order to reach the maximum optical initialization contrast, the tilt-angle of the $\lambda/4$-waveplate was not 45°, corresponding to perfectly circularly polarized light. Instead, smaller tilt-angles of 40°, which results in slightly elliptically polarized light was used.

Both, the birefringence of the YSO crystal and also the narrow multiband notch filter for 355nm and 532nm wavelength are capable to distort the laser polarization. Tilt-angles of the $\lambda/4$-waveplate generating non-perfect circularly polarized light could compensate these distortions to some extent. In general, laser polarization distortions can lower the selectivity of the spin-flip transition and thus potentially lower initialization contrasts.

Once polarized, the Ce^{3+} electron spin can be driven with MW radiation, which is resonant with the ground $4f$ state spin transition. Flipping the optically polarized spin results in an increase in fluorescence signal, since the spin is pumped out of the dark state. A sweeping of the MW frequency therefore allows for optical detection of the magnetic resonance (ODMR). In the experiment, a magnetic field with a strength of 970Gauss was applied along the b-axis of the YSO crystal, in parallel direction to the optical beam. This
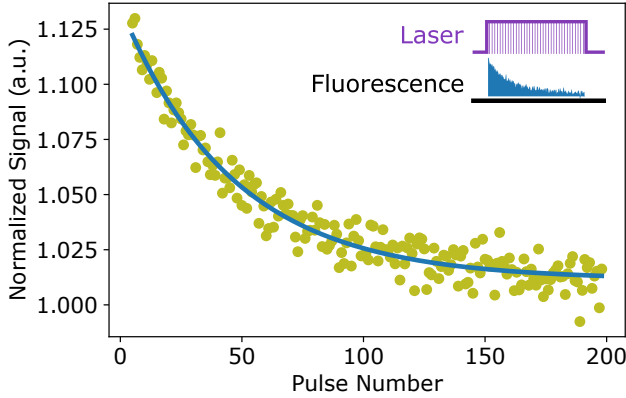
FIGURE 2.15: Fluorescence intensity as function of the laser pulse number during initialization. For coherent spin manipulation experiments, 100 pulses were used for spin initialization.
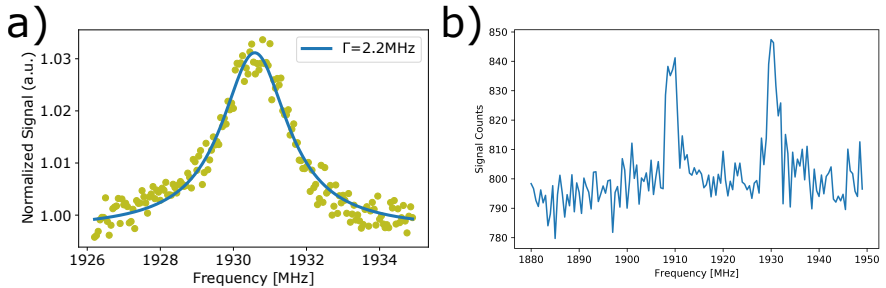
FIGURE 2.16: a) ODMR measurement of an individual Ce^{3+} ion as a function of MW frequency. A fitted Lorentzian reveals a linewidth of 2.2 MHz. b) ODMR measurement of several Ce^{3+} ions in the sample reveals two distinct magnetic resonance frequencies. The two magnetically inequivalent sites of Ce^{3+} in YSO are not degenerate for crystal orientations that slightly deviate from the b-axis.

was achieved by mounting the sample on a permanent magnet. MW radiation from a signal generator (SMT03, Rohde & Schwarz) was amplified by

a 16W high power amplifier (Mini-Circuits, ZHL-16W-43-S+) and then sent through a lithographically defined copper wire stripe in close proximity to the SILs, as depicted in figure 2.9. Sweeping the MW frequency while monitoring the fluorescence signal of individual Ce^{3+} ions results in a typical CW ODMR spectrum as shown in figure 2.16 a). Fitting a Lorentzian reveals linewidths between 2-3MHz for different Ce^{3+} ions, when measuring with low MW power in order to suppress power broadening of the ODMR linewidth. The magnetic resonance frequency of 1930.5MHz is in good agreement with the g-factor of $g \approx 1.4$ of b-cut Ce^{3+}:YSO [66]. Figure 2.16 b) shows a wide-range ODMR spectrum of several Ce^{3+} ions taken from the same crystal and reveals two distinct magnetic resonance frequencies. In general, Ce^{3+} has two magnetically inequivalent sites in YSO. For b-cut crystals, these two sites are nominally degenerate. The small frequency spacing of roughly 20MHz between the two detected resonance frequencies suggests a slight angular deviation from the perfectly b-cut crystal, which leads to the two magnetic sites to be distinguishable.

2.5 Coherent Manipulation of a single Ce^{3+}:YSO Electron Spin

In order to describe the experiments dealing with the coherent manipulation of a single electron spin, it is expedient to introduce a picture for the motion of electron spins under oscillatory and static magnetic fields [87]. As each electron possesses an intrinsic angular momentum $\hbar \boldsymbol{S}$, their magnetic moment $\boldsymbol{\mu}$ is defined by

$$\boldsymbol{\mu} = -g\mu_B \boldsymbol{S}. \tag{2.4}$$

The sum of all magnetic moments in a unit volume V is then given by

$$\boldsymbol{M} = \frac{1}{V} \sum_i \boldsymbol{\mu}_i, \tag{2.5}$$

and is called magnetization vector. Its motion can be described by the classical Bloch equations and its relaxation behavior treated phenomenologically in the same context. The equation of motion of such a spin ensemble located in a static magnetic field $\boldsymbol{B_0}$ can be described by

$$\frac{d\boldsymbol{M}}{dt} = \boldsymbol{M} \times \frac{-g\mu_B}{\hbar}\boldsymbol{B_0}, \tag{2.6}$$

where $\boldsymbol{M}$ precesses about $\boldsymbol{B_0}$ with the frequency of precession

$$\omega_{\mathrm{L}} = \frac{g\mu_B B_0}{\hbar}, \tag{2.7}$$

also called Larmor frequency. Introducing an additional magnetic field, such as a time-dependent, linearly polarized magnetic field $B_{1,x^L}(t) = 2B_1 \cos(\omega_{\mathrm{MW}}t)$, $B_{1,y^L}(t) = B_{1,z^L}(t) = 0$ with frequency ω_{MW} is readily achieved experimentally and can be treated as a superposition of a clockwise and a counterclockwise rotating rotating field $\boldsymbol{B_1^r}$ and $\boldsymbol{B_1^l}$ with

$$B_{1,x^L}^r(t) = B_{1,x^L}^l(t) = B_1 \cos(\omega_{\mathrm{MW}}t), \tag{2.8}$$
$$B_{1,y^L}^r(t) = -B_{1,y^L}^l(t) = B_1 \sin(\omega_{\mathrm{MW}}t), \tag{2.9}$$
$$B_{1,z^L}^r(t) = B_{1,z^L}^l(t) = 0. \tag{2.10}$$

When $\boldsymbol{B_1^r}$ and $\boldsymbol{B_1^l}$ are transformed into the rotating frame, which rotates in the right-hand sense with frequency ω_{MW} about the z^L-axis of the laboratory frame, we obtain $B_{1,x^L}^r = B_1$, $B_{1y^L}^r = B_{1,z^L}^r = 0$ and $B_{1,x^L}^l = B_1 \cos(2\omega_{\mathrm{MW}}t)$, $B_{1y^L}^l = B_1 \sin(2\omega_{\mathrm{MW}}t) B_{1,z^L}^l = 0$. Commonly $\omega_1 = \frac{g\mu_B B_1}{\hbar} \ll 2 \cdot \omega_{\mathrm{MW}}$ and therefore we can neglect $\boldsymbol{B_1^l}$ if the resonance condition $\omega_{\mathrm{L}} = \omega_{\mathrm{MW}}$ is fulfilled [87]. In this situation, a second precession about the MW field direction, in addition to the one about the direction of $\boldsymbol{B_0}$, with frequency ω_1 becomes apparent when asked for the equation of motion of the magnetization in the rotating frame under influence of both, static magnetic field $\boldsymbol{B_0} = \boldsymbol{e}_{z^L}B_0$ and alternating magnetic field along the x-axis of the rotating frame $\boldsymbol{B_1^r} =$

$B_1(e_{x^L}\cos(\omega_{MW}t) + e_{y^L}\sin(\omega_{MW}t))$. We then obtain

$$\frac{dM_x}{dt} = -(\omega_L - \omega_{MW})M_y = -\Omega_L M_y, \tag{2.11}$$

$$\frac{dM_y}{dt} = (\omega_L - \omega_{MW})M_x - \frac{g\mu_B B_1}{\hbar}M_z = \Omega_L M_x - \omega_1 M_z, \tag{2.12}$$

$$\frac{dM_z}{dt} = \frac{g\mu_B B_1}{\hbar}M_y = \omega_1 M_y, \tag{2.13}$$

with $\Omega_L = \omega_L - \omega_{MW}$. For resonant radiation ($\Omega_L = 0$), oriented along the x-axis of the rotating frame and applied for pulse length t_p, integrating equations 2.11-2.13 with initial conditions $M_z = M_0, M_x = M_y = 0$ allows to find the magnetization vector at time t_p:

$$M_x = 0, \tag{2.14}$$

$$M_y = -M_0\sin(\omega_1 t_p), \tag{2.15}$$

$$M_z = M_0\cos(\omega_1 t_p). \tag{2.16}$$

The resonant pulse rotates M by the flip angle $\varphi = \omega_1 t_p$ about the x-axis. The choice of the rotating frame direction, for example along x-axis, merely depends on the phase ϕ of the linearly polarized MW field, as can be seen when transforming $B_{1,x^L}(t) = 2B_1\cos(\omega_{MW}t + \phi)$, $B_{1,y^L}(t) = B_{1,z^L}(t) = 0$ into the rotating frame:

$$B_{1x} = B_1\cos(\phi), \tag{2.17}$$

$$B_{1y} = B_1\sin(\phi), \tag{2.18}$$

$$B_{1z} = 0. \tag{2.19}$$

This is commonly used experimentally, as controlling the phase of MW radiation is conveniently implemented, as discussed later in this chapter.

The precession of the magnetization vector after the application of MW pulses

generally relaxes back to the thermal equilibrium value M_0 and therefore relaxation mechanisms are added to equations 2.11-2.13. Relaxation of the longitudinal magnetization along z and of the transverse magnetization in the xy-plane are seperated. While both are modelled as an exponential process, the longitudinal relaxation happens on the order of the T_1 time, also referred to as *spin-lattice relaxation time*, and the transverse relaxation happens on the order of the T_2 time, also referred to as *spin-spin relaxation time*. They are introduced as phenomenological factors in the Bloch equations as follows:

$$\frac{dM_x}{dt} = -\Omega_{\mathrm{L}}M_y - \frac{M_x}{T_2}, \qquad (2.20)$$

$$\frac{dM_y}{dt} = \Omega_{\mathrm{L}}M_x - \omega_1 M_z - \frac{M_y}{T_2}, \qquad (2.21)$$

$$\frac{dM_z}{dt} = \omega_1 M_y - \frac{(M_z - M_0)}{T_1}. \qquad (2.22)$$

The motion of the magnetization vector can be aptly visualized by a geometrical representation, called Bloch sphere. Here, a two-level quantum system is represented by a sphere with the radius equal to the magnitude of the magnetic moment. In general, the two levels correspond to the magnetization vector aligned with the static magnetic field and aligned in the opposite direction of the magnetic field. Alternatively, a single spin is treated with the two states $|\uparrow\rangle$ and $|\downarrow\rangle$, as depicted in figure 2.17 a). In accordance with equations 2.14-2.16, MW radiation of certain amplitude and applied for certain amount of time is capable to flip the spin by $\varphi = \pi/2$ onto the y-axis. Once flipped to the xy-plane, a superposition between $|\uparrow\rangle$ and $|\downarrow\rangle$ is created, referred to as coherence and represented by a transversal magnetization. Its T_2-decay is depicted in figure 2.17 b) as the dephasing of individual spins, losing their phase relation through fluctuating magnetic fields. Such fluctuations can for example come from nuclear spins in the proximity of a Ce^{3+} electron spin and they can contribute to decoherence.

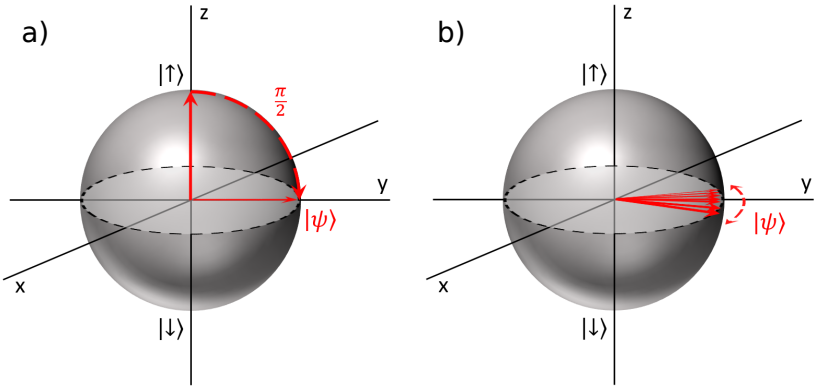For measurements of coherent manipulation of a single Ce^{3+} spin, the optical

FIGURE 2.17: Bloch sphere representation of single spin manipulation. a) Resonant $\pi/2$-pulse flips the spin around the x-axis onto the xy-plane and creates a superposition between the two states $|\uparrow\rangle$ and $|\downarrow\rangle$. b) During the free evolution of the spin, that was put into a superposition state between $|\uparrow\rangle$ and $|\downarrow\rangle$, it precesses around the z-axis and acquires a phase.

initialization of the spin is a fundamental requirement, that allows for sampling the spin starting from a well-defined point, such as the $|\uparrow\rangle$ state for example. Subsequent application of a resonant MW pulse of variable duration τ and a final readout step allows for measurements of spin Rabi oscillations. According to equations 2.14-2.16, the continuous application of a resonant MW field leads to the spin rotating around the x-axis and its projection onto the z-axis will show oscillatory behavior, also called Rabi oscillations. Experimentally, the projection onto the z-axis is realized by optically exciting the Ce³⁺ ion in the same fashion as done during the initialization. The acquired signal related to the z-projection of the Ce³⁺ spin is the fluorescence collected during the readout step for a certain amount of time, the so-called readout time and it ranged between 2-5μs, or 20-50 laser pulses in the experiments. Figure 2.18 shows the Rabi measurement and the corresponding schematic pulse diagram. An exponentially decaying cosine function with constant offset fitted to the Rabi measurement data reveals a Rabi frequency
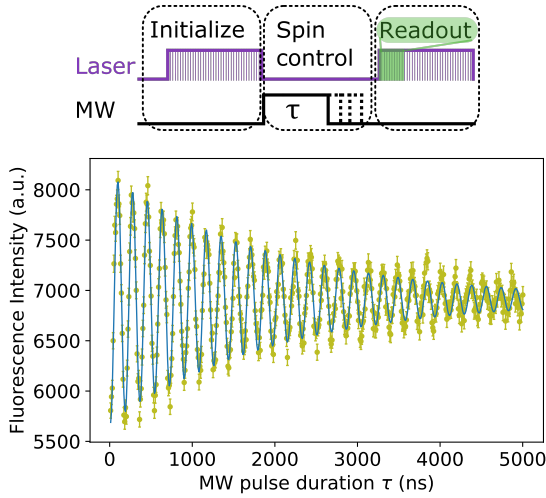
FIGURE 2.18: Top: Schematic diagram of the pulse sequence used for spin Rabi oscillation measurements. Laser repetition rate was 10MHz. Bottom: Single Ce^{3+} ion spin Rabi oscillations. Blue line is an exponentially decaying cosine function with constant offset fitted to the data, revealing a Rabi frequency of 5.6MHz and a decay time of 2μs.

of 5.6MHz and a decay time of 2μs. Generally, the spin Rabi oscillation decay can have multiple dependencies, such as the strength of the driving field, and the unique spin environment coupling to the decohering spin [88, 89]. Based on this underlying complexity, the Rabi measurements do not give significant spectroscopic information, but rather serve as a handy tool to define certain MW pulses, such as $\pi/2$, π and $3\pi/2$.

Hence, prior to performing any pulsed MW experiments discussed in this chapter, a Rabi measurement for precisely defining the MW pulses was performed. The experimental setup for this included the resonant radiation at 1930.5MHz to be generated by the signal generator (Rohde & Schwarz, SMT03). It was split by a power splitter/combiner (Mini-Circuits, ZFSC-2-372-S+) and each of the outputs were fed into their own high isolation

switch (Mini-Circuits, ZASWA-2-50DR+). The switches were controlled by a high speed programmable pulse generator (SpinCore Technologies Inc., PulseBlasterESR-PRO™). By adjusting the respective lengths of the coaxial cables between the outputs of the two separate switches and the downstream combiner (Mini-Circuits, ZX10-2-25-S+), a phase difference of 90° between the two individually controlled MW lines was achieved for the MW frequency of interest. This allowed the application of π_x and π_y pulses, needed for spin decoupling sequences. After combining the two MW lines, they were fed into the MW amplifier (Mini-Circuits, ZHL-16W-43-S+), following a MW circulator and then sent to the sample.

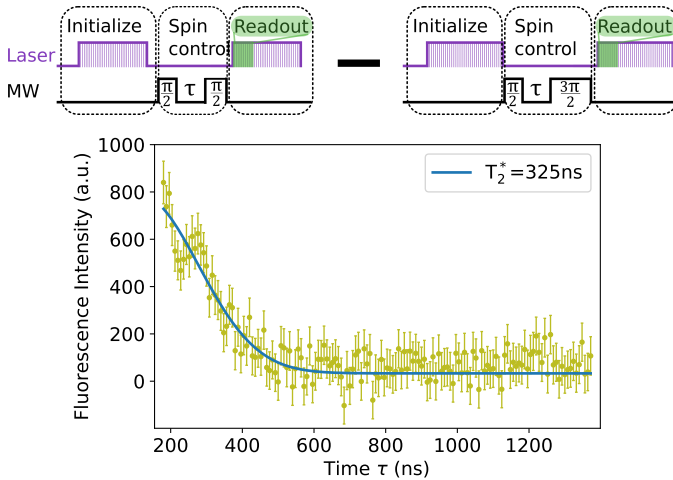## 2.6 Relaxation Times of a single Ce^{3+}:YSO Electron Spin

FIGURE 2.19: Top: Schematic diagram of the pulse sequence used for FID measurements. The difference between final $(\pi/2)_x$-pulse and final $(3\pi/2)_x$-pulse is given as fluorescence intensity. Bottom: Ramsey measurement of Ce^{3+} with Gaussian fit yielding $T_2^* = 325$ns.

Measurements with the Ramsey sequence $(\pi/2)_x - \tau - (\pi/2)_x$, reveal the FID of the Ce^{3+} electron spin. In the sequence, the first $(\pi/2)_x$-pulse creates the coherence, that subsequently decays during the waiting time τ. The last $(\pi/2)_x$-pulse serves to project the spin to the z-axis of the Bloch sphere in order to convert the remaining coherence back into a population difference, that can be measured optically. The signal acquisition, also depicted in figure 2.19, was done with a balanced measurement sequence. Here, the final pulses in the sequence were alternatingly projecting the spin to $|\uparrow\rangle$ or $|\downarrow\rangle$ by either $(\pi/2)_x$-pulse or $(3\pi/2)_x$-pulse. The two signals were subsequently subtracted from each other. The FID depends on the thermal noise of the characteristic nuclear spin bath of YSO, consisting of ^{89}Y and ^{29}Si nuclear spins and probes the inhomogeneous broadening, also referred to as T_2^* time of the Ce^{3+} spin. Figure 2.19 presents such a typical FID of Ce^{3+} and the Gaussian fit quantifies the inhomogeneous linewidth of the spin transition to $T_2^* = 325$ns. This dephasing time is agreeing well with ODMR linewith measurements. While the interacting nuclear spin bath generally acts as the main contribution to inhomogeneous broadening of the spin transition, the short-pulsed optical UV excitation of Ce^{3+} , which is capable to ionize Ce^{3+} and electron traps nearby, can induce magnetic noise fluctuations due to electron spins in traps, and can contribute to inhomogeneous broadening. These measured coherence times are short and do not show fringes, that would allow for inference about hyperfine coupled spins [90].

Measuring the spin lifetime of the spin state T_1 quantifies the fundamental time limit, during which the Ce^{3+} electron spin can be probed and allows for estimating a limitation for coherent interaction time T_2 with the follwing formula [91]:

$$\frac{1}{T_2} = \frac{1}{2T_1} + \frac{1}{T_2^*}. \tag{2.23}$$

With the help of coherent control-pulse methods, the T_2^*-related dephasing is generally reversible by dynamical refocusing, and the typically ultimate
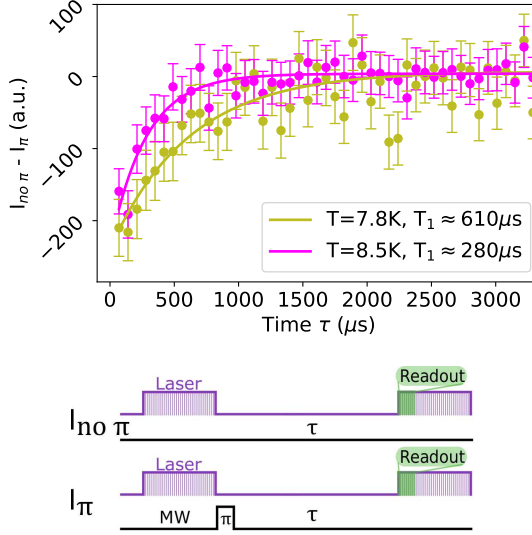
FIGURE 2.20: Top: Spin relaxation measurement shows $T_1 = 610\mu s$ and $T_1 = 280\mu s$ for sample temperatures of 7.8K and 8.5K. Bottom: Signal is the difference between the two depicted sequences.

limitation of the transverse relaxation T_2 is given by the energy relaxation with $T_2 \approx 2T_1$.

In order to measure the lifetime of the spin state T_1, fluorescence in the two pulse sequences shown in figure 2.20 was acquired and their difference plotted as signal data. During the experiment, the two sequences were alternatingly executed and in this way, laser power fluctuations related to the different waiting times τ were accounted for. These laser power fluctuations emerged on the time scale of milliseconds, and are related to the design of the synchronously pumped laser with intra-cavity pulse picking, and they were compensated by the alternating reference pulse sequence design. The T_1 pulse sequence consists of an optical initialization into a defined spin state, a

variable waiting time τ and a subsequent readout of the spin state. The microwave π-pulse ensures an initialization into the opposing spin state compared to what is found after optical initialization only and allows to extract a appreciable laser power fluctuation compensated signal. The spin-lattice relaxation time measurements reveal $T_1 = 610\mu s$ at an indicated temperature of $T_{\text{indicated}} = 3.8K$, measured at the heat exchanger of the cold-finger cryostat. By heating the sample to an indicated temperature of $T_{\text{indicated}} = 4.5K$, the measured spin-lattice relaxation time amounted to $T_1 = 280\mu s$. By comparing these values with EPR based T_1 values [92], we can readjust the indicated temperature to an actual sample temperature, which is approximately 4K higher than measured on the heat exchanger. The limited cooling power and heat conductivity are main reasons for this offset temperature.

2.7   Sensing Proximal Nuclear Spins

With the sub-microsecond-long T_2^* of Ce^{3+} , only fast fluctuations with frequencies in the few MHz regime would become aparent in Ramsey experiments. However, the T_1 time of more than half a millisecond suggests that Ce^{3+} electron spin can in principle be used to detect magnetic fields with oscillation frequencies in the range of kHz-MHz. Established methods such as spin echo sequences allow for detection of said lower frequencies, by attenuating the environmental spin noise, that leads to decoherence and by filtering signals of interest. Key to their robustness against shifts and slow variations of magnetic fields are so-called refocus-pulses, that can inverse the phase acquisition of the spin and cancel contributions that lead to inhomogeneous broadening.

2.7.1   Detection of ^{89}Y Nuclear Spins

The most fundamental spin echo sequence is the Hahn echo sequence $(\pi/2)_x - \tau - \pi_x - \tau' - (\pi/2)_x$. Analog to the Ramsey sequence, the first $(\pi/2)_x$-pulse
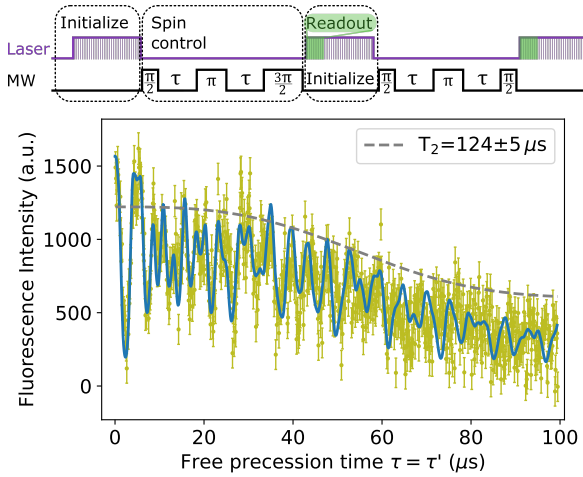
FIGURE 2.21: Top: Schematic diagram of the pulse sequence used for Hahn echo measurements, which show the difference between the final $3\pi/2$ MW pulse signal and the final $\pi/2$ MW pulse signal. Bottom: Hahn echo measurement shows collapse and revivals. The decay is fitted to $\exp\left[-(2\tau/T_2)^3\right]$ (grey dashed line), with $T_2 = 124\mu s$, plotted offset on the intensity axis to envelope the signal. Simulated coherence is plotted as blue continuous line.

creates the coherence and the spin starts acquiring a phase during the waiting time τ. The subsequent π_x-pulse flips the spin around the x-axis by $180°$, thereby inversing the phase acquisition. If $\tau = \tau'$ is fulfilled, slow (compared to τ) changes of the magnetic field in the environment are completely cancelled. For all Hahn echo experiments presented in this chapter, this condition was fulfilled. After the second waiting time τ, a final $(\pi/2)_x$-pulse or $(3\pi/2)_x$-pulse projects the spin onto $|\uparrow\rangle$ or $|\downarrow\rangle$, respectively, and enables optical readout of the population. The refocusing induced by the π_x-pulse compensates the inhomogeneous broadening and prolongs the time the Ce^{3+} electron spin is capable to coherently interacts with its environment. This allows for a more detailed spin spectroscopy of the nuclear spin environment

of Ce^{3+} ions. A representative Hahn echo measurement of a single Ce^{3+} elec-
tron spin is shown in figure 2.21. Periodic revivals related to yttrium ions in
the crystal can be observed. Yttrium has 100% abundance of isotope ^{89}Y with
a nuclear spin $I_Y = 1/2$ and magnetic moment $\mu_Y = -0.137\mu_N$. Also, the co-
herence time T_2 can be extracted by fitting $\exp\left[-(2\tau/T_2)^3\right]$ to the decaying
signal and amounts to $T_2 = 124\mu s$ [49]. The signal acquisition, also depicted
in figure 2.21, was done with a balanced measurement sequence. Here, the fi-
nal pulses in the sequence were alternatingly projecting the spin to $|\uparrow\rangle$ or $|\downarrow\rangle$
by either $(\pi/2)_x$-pulse or $(3\pi/2)_x$-pulse. The two signals were subsequently
subtracted from each other and the result corresponds to the coherence of the
electron spin at a time τ, which is defined as the transverse spin component
$S_t = |\uparrow\rangle - |\downarrow\rangle$. The blue line plotted in figure 2.21 comes from a simula-
tion based on the CCE method [50], discussed in more detail throughout this
chapter. Simulations based on this method were done in collaboration with
colleagues from Beijing Computational Science Research Center in China.

The CCE method was used to simulate the coherence of the Ce^{3+} electron
spin in an interacting bath, such as the complex nuclear spin environment
resented by the YSO matrix. In these simulations, only the ground state dou-
blet subspace of the Ce^{3+} ion located in the magnetic field was regarded,
which is merely the Zeeman-term from the system Hamiltonian, and pre-
sented in equation 2.3, with eigenstates $|+\rangle$ and $|-\rangle$. The effective g-factor
of Ce^{3+} is [66, 93]

$$\boldsymbol{g}_{\text{eff}} = g_e \begin{pmatrix} 0.6514 & 0.2629 & 0.3004 \\ 0.2629 & 0.6799 & -0.0858 \\ 0.3004 & -0.0858 & 0.9098 \end{pmatrix}, \tag{2.24}$$

where $g_e = 2.0023$ is the elctron spin g-factor. The nuclear spin environment
of Ce^{3+} is a dense bath of ^{89}Y nuclear spins and ^{29}Si nuclear spins. The inter-
action between these nuclear spins and the Ce^{3+} electron spin is described

by the magnetic dipole-dipole interaction [43]

$$H_{\text{int}} = \sum_i \frac{\mu_B \mu_0 \gamma_i}{4\pi r_i^3} \boldsymbol{S} \cdot \boldsymbol{g}_{\text{eff}} \cdot (3\boldsymbol{n}_i \boldsymbol{n}_i - \mathbb{I}) \cdot \boldsymbol{I}_i, \tag{2.25}$$

where γ_i the gyromagnetic ratio of the i-th nuclear spin, $\boldsymbol{I}_i$ is the spin operator of the i-th nuclear spin, r_i is the distance between the i-th nuclear spin and the Ce^{3+} electron spin, $\boldsymbol{n}_i$ is the corresponding unit vector, and $\mathbb{I}$ is the identiy operator. Because a $4f$ electron is considered, which is localized at the Ce^{3+} position, no Fermi contact interaction term is included. Bath interactions within the nuclear spin bath are described by the following Hamiltonian

$$H_{\text{bath}} = \sum_i \gamma_i \boldsymbol{B} \cdot \boldsymbol{I}_i + \sum_{i>j} \frac{\mu_0 \gamma_i \gamma_j \hbar}{4\pi r_{ij}^3} \boldsymbol{I}_i \cdot (3\boldsymbol{n}_{ij} \boldsymbol{n}_{ij} - \mathbb{I}) \cdot \boldsymbol{I}_j, \tag{2.26}$$

with r_{ij} as distance between two nuclear spins, and $\boldsymbol{n}_{ij}$ as the corresponding unit vector.

In the following, the investigation of the decoherence of Ce^{3+} under CPMG-N dynamical decoupling sequences is discussed.[1] Main contribution to decoherence are surrounding nuclear spins. Experimentally, the Ce^{3+} electron is initialized into a polarized state and prepared in a superposition state $(|+\rangle + |-\rangle)/\sqrt{2}$ by applying a $(\pi/2)_x$-pulse. The initial state of the nuclear spin bath is hardly polarized and can consequently be modelled as a high-temperature mixed state $\rho_{\text{bath}} = \otimes_{i=1}^N (\mathbb{I}_i / \text{Tr}[\mathbb{I}_i])$, where $\mathbb{I}_i$ is the identity operator for the i-th nuclear spin. The bath spins will evolve according to the Hamiltonian $H_\pm$

$$
\begin{aligned}
H_\pm &= \langle \pm | H_{\text{int}} + H_{\text{bath}} | \pm \rangle & (2.27) \\
&= H_{\text{bath}} \pm \frac{1}{2} \sum_i \frac{\mu_B \mu_0 \gamma_i}{4\pi r_i^3} \boldsymbol{n}_B \cdot \boldsymbol{g}_{\text{eff}} \cdot (3\boldsymbol{n}_i \boldsymbol{n}_i - \mathbb{I}) \cdot \boldsymbol{I}_i, & (2.28)
\end{aligned}
$$

---

[1]For more detailed discussion about CPMG dynamical decoupling sequences, see the following chapter 2.7.2. For N=1, we have the special case of Hahn Echo with a π_y-pulse.

where $H_{\pm}$ is conditional on the electron spin state $|+\rangle$ or $|-\rangle$, and $\boldsymbol{n}_B$ the unit vector of the magnetic field. After the coherent state $(|+\rangle + |-\rangle)/\sqrt{2}$ is prepared, it will start entangling with the conditional bath spin states governed by $H_{\pm}$. Under N-pulse dynamical decoupling, the Ce^{3+} electron spin coherence is then given by

$$L(2N\tau) = \text{Tr}_{\text{bath}} \left[e^{-iH_-\tau} \cdots e^{-iH_+2\tau} e^{-iH_-2\tau} \times \right.$$
$$\left. e^{-iH_+\tau} \rho_{\text{bath}} e^{iH_-\tau} e^{iH_+2\tau} e^{iH_-2\tau} \cdots e^{iH_+\tau} \right], \qquad (2.29)$$

with τ as the pulse interval of the CPMG-*N* sequence. Instead of calculating the many-body dynamics involving hundreds of spins, the Ce^{3+} center spin coherence $L(2N\tau)$ can be factorized into contributions $\tilde{L}_C(2N\tau)$ of different correlated nuclear spin clusters *C*, with [94, 50]

$$L(2N\tau) = \prod_{\{C\}} \tilde{L}_C(2N\tau). \qquad (2.30)$$

$\tilde{L}_C(2N\tau)$ is calculated similarly to equation 2.29:

$$\tilde{L}_C(2N\tau) = \text{Tr}_{\text{bath}} \left[e^{-iH_{-,C}\tau} \cdots e^{-iH_{+,C}2\tau} e^{-iH_{-,C}2\tau} \times \right. \qquad (2.31)$$
$$\left. e^{-iH_{+,C}\tau} \rho_{\text{bath}} e^{iH_{-,C}\tau} e^{iH_{+,C}2\tau} e^{iH_{-,C}2\tau} \cdots e^{iH_{+,C}\tau} \right]. \qquad (2.32)$$

Generally, only interactions within a cluster *C* are included in the conditional Hamiltonians $H_{-,C}$ and $H_{+,C}$. In the actual calculation, the size *K* of the cluster, defined as the number of spins in the cluster, is stepwise increased until the result converges [50]. For the Ce^{3+} electron spin in YSO matrix, it was found, that a cluster size of $K = 1$, that means CCE-1, is sufficient. Since Zeeman interaction strength and hyperfine interaction strength between the Ce^{3+} central spin and the nuclear spins are both much larger than the interaction within the bath spins in our system, a non-interacting nuclear spin bath approximation can be used.

In the specific case of the Hahn echo measurement shown in figure 2.21, the
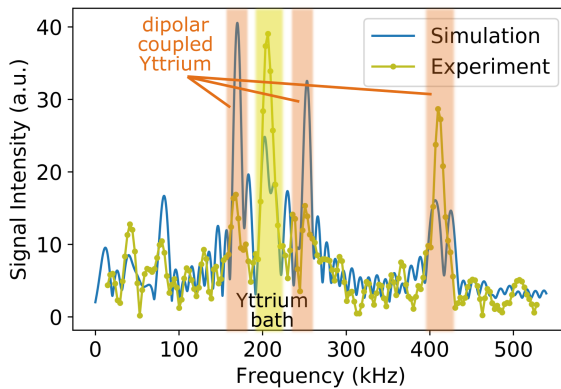
FIGURE 2.22: FFT of the Hahn-Echo signal (olive) and FFT of the simulated Hahn-Echo signal (blue). Highlighted in yellow is the yttrium bath contribution at ≈ 200kHz. Highlighted in orange are the contributions orginiating from dipolar coupled yttrium nuclear spins in close proximity to Ce^{3+}.

CCE-1 calculations plotted as the blue line agree strikingly well with our experimental results, given that the Ce^{3+} electron spin is located in a complex environment. Even more revealing is the FFT of the Hahn echo signal, shown in figure 2.22, where two particular facts can be seen. At the applied magnetic field of 970Gauss, the ^{89}Y bath is expected to evolve at a Lamor precession frequency of $\omega_{Y,Lamor} \approx 200$kHz and also to create this specific oscillating magnetic field at the Ce^{3+} location. For each individual Hahn-Echo measurement sequence, the magnitude of $\omega_{Y,Lamor}$ is different, depending on the particular realization. If the waiting time τ of the Hahn-Echo sequence (or in general decoupling sequence), which precedes the phase inverting π-pulse, exactly matches $\omega_{Y,Lamor}$, the signs do not cancel out anymore and a phase is acquired by the Ce^{3+} electron spin. This leads to a dip in the echo signal, corresponding to ^{89}Y bath induced decoherence and translates into the measured frequencies in the FFT (figure 2.22). We can see the ^{89}Y bath

related signatures in the FFT, similarly known from ^{13}C in proximity to nitrogen vacancy centers in diamond [49].

Additionally, frequency components related to strongly coupled ^{89}Y nuclear spins are seen, which interact with the Ce^{3+} electron spin based on the magnetic dipole interaction and are located in close proximity to Ce^{3+} electron spin. While the frequency components of the ^{89}Y bath $\omega_{Y,Lamor} \approx 200kHz$ are not dependent on the electron spin state, proximal ^{89}Y nuclear spins feel the back action of the Ce^{3+} spin. Experimental data and simulation show both a good agreement for the hyperfine coupling strengths, leading to a line splitting in the FFT. As the frequency compenents of the second harmonic of $\omega_{Y,Lamor}$ are phase shifted with respect to $\omega_{Y,Lamor}$, they can also be attributed to dipolar coupled ^{89}Y [87]. This can be seen as negative value of the real part in the FFT signal, shown in figure 2.23.
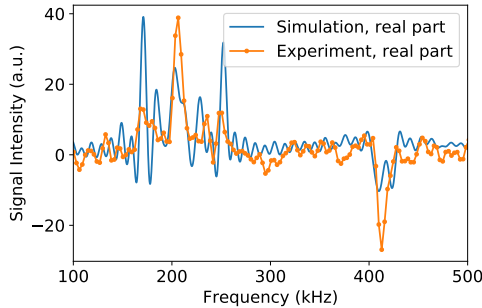
FIGURE 2.23: Real parts of the FFT of the Hahn-Echo signal (orange) and FFT of the simulated Hahn-Echo signal (blue). The negative real part represents a phase rotation from the positive real part.

Based on the stepwise increase in ^{89}Y nuclear spins during simulation, it was found, that approximately the eight clostest ^{89}Y nuclear spins nearby Ce^{3+} are hyperfine coupled to the Ce^{3+} spin. Their shift in frequency from the ^{89}Y bath can be understood from the concept of the frozen core, known from similar systems, for example ruby [95]. In our specific situation, the

strong magnetic dipole related to the Ce^{3+} electron spin affects nearby nuclear spins by shifting their respective quantization axis and in turn detuning their frequencies from the original ^{89}Y bath frequency. The region of detuned nuclear spins is then called frozen core and based on simulations, it gives the main contribution to the signals plotted in figures 2.21 and 2.22, compared to bath ^{89}Y nuclear spins located at a larger distance from the Ce^{3+} center spin. Based on equation 2.25, the expected couplings between Ce^{3+} and the eight closest yttrium nuclear spins, which contribute to the class of strongly dipolar coupled spins, can be given.

# of Nuclei	Lattice coordinates relative to Ce^{3+} (Å)	Coupling tensor $\mathbb{A}/2\pi$ (MHz)		
^{29}Si-1	[2.82,1.05,2.03]	-0.361	-0.128	-0.314
		-0.185	0.122	-0.223
		-0.450	-0.233	-0.095
^{89}Y-1	[-0.54,0.86,3.31]	0.072	0.007	-0.039
		0.027	0.061	-0.021
		0.063	-0.065	-0.131
^{89}Y-2	[2.27,2.48,-1.16]	-0.027	-0.068	0.069
		-0.088	-0.062	0.050
		0.054	0.023	0.065
^{89}Y-3	[-1.44,3.33,0.58]	0.054	0.014	0.022
		0.066	-0.053	-0.025
		0.018	0.004	0.073
^{89}Y-4	[-0.90,2.48,-2.73]	0.036	0.047	-0.009
		0.041	-0.013	0.062
		-0.018	0.103	-0.055

Table 2.3 – continued from previous page

# of Nuclei	Lattice coordinates relative to Ce^{3+} (Å)	Coupling tensor $\mathbb{A}/2\pi$ (MHz)
^{89}Y-5	[-1.44,-3.49,0.58]	$\begin{pmatrix} 0.011 & -0.066 & 0.035 \\ -0.039 & -0.092 & 0.017 \\ 0.029 & 0.014 & 0.060 \end{pmatrix}$
^{89}Y-6	[1.37,0,-3.89]	$\begin{pmatrix} 0.040 & 0.015 & 0.006 \\ 0.005 & 0.038 & 0.022 \\ 0.059 & -0.005 & -0.069 \end{pmatrix}$
^{89}Y-7	[-3.71,0.86,1.74]	$\begin{pmatrix} -0.022 & 0.027 & 0.042 \\ -0.004 & 0.040 & 0.004 \\ 0.029 & -0.007 & 0.042 \end{pmatrix}$
^{89}Y-8	[3.57,-2.55,1.74]	$\begin{pmatrix} -0.014 & 0.037 & -0.008 \\ 0.027 & 0.013 & 0.005 \\ -0.040 & 0.033 & 0.009 \end{pmatrix}$

TABLE 2.3: List of nuclear spins, that are strongly dipolar coupled to Ce^{3+}, as found in simulations reproducing the experimental results. For ^{29}Si , only the given lattice site yields highest agreement with experimental data discussed throughout this chapter. Ce^{3+} ion is set to be located at origin [0,0,0]. The respective lattice coordinates are given relative to Ce^{3+}. The corresponding coupling tensors $\mathbb{A}/2\pi$ are given in Mhz.

Table 2.3 lists the relative lattice coordinates r with respect to Ce^{3+} central spin, located at the origin and the corresponding coupling tensors (from

equation 2.25)

$$\mathbb{A} = \frac{\mu_B \mu_0 \gamma_n}{4\pi r^3} g_{\text{eff}} \cdot (3\boldsymbol{nn} - \mathbb{I}),$$ (2.33)

where $\boldsymbol{n} = \boldsymbol{r}/|\boldsymbol{r}|$ the unit vector. The dipolar coupled yttrium nuclear spins have coupling strengths of a few tens of kHz.
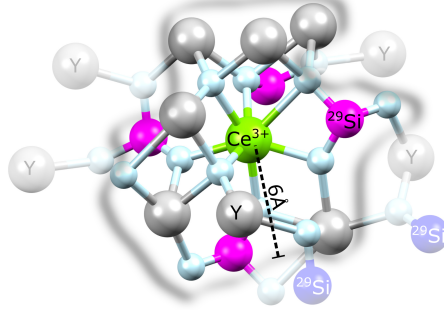
2.7.2 Detection of a Single ^{29}Si Nuclear Spin

FIGURE 2.24: Schematic of the YSO crystal with embedded Ce^{3+}. Within 6Å distance, ^{29}Si coupling is detected (magenta), more remote ^{29}Si cannot be distinguished (blue).

Apart from ^{89}Y nuclear spins, also ^{29}Si nuclear spins occur in the YSO crystal. Silicon in the YSO crystal has a natural abundance of 4.7% ^{29}Si isotope, which has a nuclear spin $I_{\text{Si}} = 1/2$ and a magnetic moment of $\mu_Y = -0.555\mu_N$. By using confocal microscopy, studying spatially resolved Ce^{3+} ions allows to probe the unique spin environments of single Ce^{3+} ions. This spin environment consists of a ^{29}Si nuclear spin as nearest neighbor with a chance of approximately 20%. Signals related to the ubiquitous ^{89}Y nuclear spin bath are expected to dominate the noise spectroscopic study of Ce^{3+} in YSO based on the sheer difference in quantity, yet under certain conditions ^{29}Si signatures can be present simultaneously. For example when located at the nearest

neighbor position (at a distance $\leq 6\text{Å}$) of Ce^{3+} , a ^{29}Si nuclear spin can exhibit a detectable hyperfine coupling based on magnetic dipole interaction, following from CCE simulations. Table 2.3 also lists the hyperfine tensor for the nearest neighbor ^{29}Si , which will be discussed throughout this section. Expected coupling strength for this ^{29}Si nuclear spin are tens to a few hundred kHz. This situation is picturized in figure 2.24. The ^{29}Si coupling signal is expected to be superimposed on the hyperfine signal emergent from closeby ^{89}Y spins and the ^{89}Y bath and its magnitude is dependent on the distance between ^{29}Si and Ce^{3+} spin.
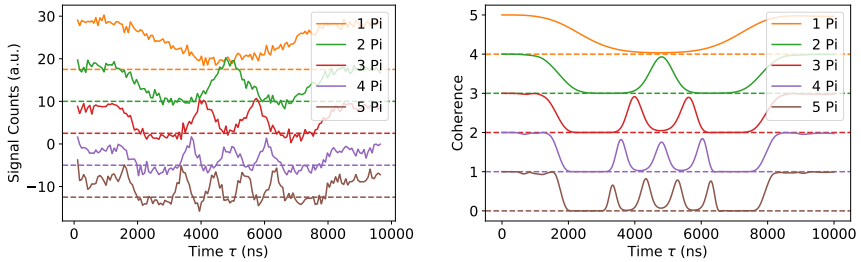

FIGURE 2.25: Measurements (left) and CCE simulation (right) for CPMG-N decoupling sequences with varying number $N = 1, \ldots, 5$ of π_y-pulses. Coherence signature is split into N dips and bandwidth of decoupling sequence is decreasing, indicative at sharper slopes of the signal.

Probing of the nuclear spin environment of Ce^{3+} is done by dynamical decoupling noise spectroscopy, which uses dynamical decoupling sequences, such as the CPMG control sequence, to directly measure the spin noise, that decoheres the central Ce^{3+} electron spin. The CPMG-N sequence consists of an initial $(\pi/2)_x$-pulse, that creates the coherence. Then a block of waiting time τ followed by a π_y-pulse, that inverses the phase acquisition and another waiting time τ is repeated N times, corresponding to the respective CPMG-N sequence. Finally, a $(\pi/2)_x$-pulse or a $(3\pi/2)_x$-pulse projects the spin to $|\uparrow\rangle$ or $|\downarrow\rangle$, where its coherence can be read out optically. In general the pulse sequence follows $(\pi/2)_x - (\tau - \pi_y - \tau)^N - (\pi/2)_x$, and for the case of

$N = 3$, this gives $(\pi/2)_x - \tau - \pi_y - 2\tau - \pi_y - 2\tau - \pi_y - \tau - (\pi/2)_x$, for example. Here, the dynamical decoupling sequence acts as a noise filter function and its bandwidths B_N generally depends on the number of pulses N and scales approximately with $B_N \propto f/(N/2)$ at a frequency $f = 1/2\tau$ [96]. This can be explained by the periodic refocusing of environmental effects via π_y-pulses, which is extending the T_2 time by suppressing the decohering noise. Nuclear spin noise precessing at a lower frequency than the pulse spacing related sampling frequency $f = 1/2\tau$ is cancelled out. In general, CPMG-N can be seen as a band-pass filter, which is leaky for higher odd harmonics [97]. Only if the sampling frequency matches the Lamor frequency of the respective nuclear spin, the decoherence is gathered by the noise spectroscopy and is reflected in a drop of coherence of the Ce^{3+} electron spin coherence signal. Measuring the Ce^{3+} electron spin (spin-1/2 system) with higher order CPMG-N sequences, causes the ^{89}Y nuclear spin signature (and also the ^{29}Si signature, as we will see further on) to split into N coherence dips, while the position of the feature stays centered around the same waiting time τ. This behavior and the bandwidth scaling can be seen in figure 2.25, where the first coherence drop of Ce^{3+} associated with ^{89}Y nuclear spins and the subsequent revival is measured for delay times up to $\tau = 10\mu s$.

In the following, CPMG-N noise spectra acquired from two distinct individual Ce^{3+} ions, labelled "ion A" and "ion B", are shown in figure 2.26 as a comparison and discussed. Specifically, CPMG-N decoupling sequences with π_y-pulse numbers $N = 1, 2, 5$ were used during the experiments. In the case of $N = 1$, "ion B" reveals a dip in coherence at a waiting time $\tau_{dip} \approx 600ns$, whereas "ion A" does not. This corresponds to the frequency $f_{dip} = 1/2\tau_{dip}$, which matches well with the gyromagnetic ratio of ^{29}Si nuclear spin $\gamma_{Si} = -8.465MHz/T$ for the given magnetic field. The ^{29}Si nuclear spin signature detected in the noise spectroscopy of "ion B" confirms the local environment of "ion B" to host a ^{29}Si nuclear spin.

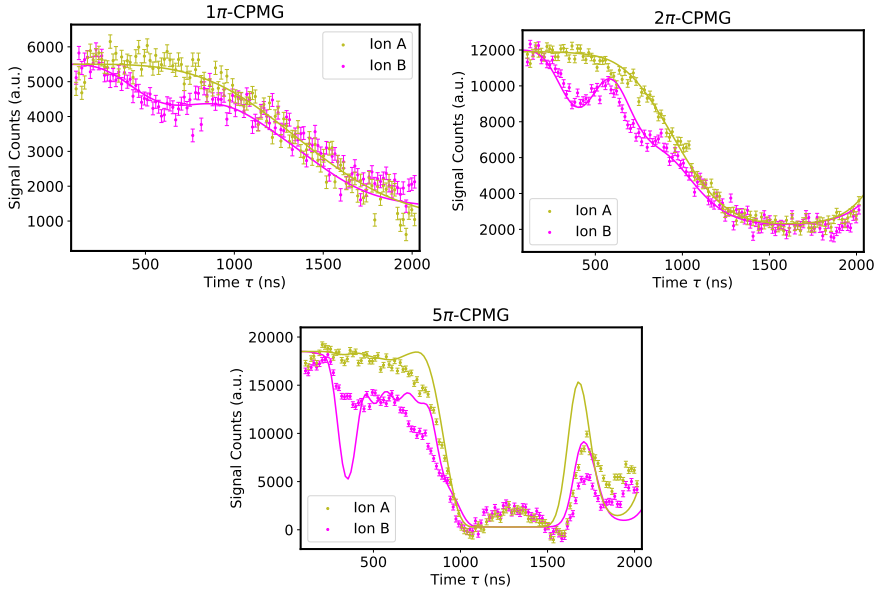Based on CCE simulations, the ^{29}Si nuclear spin signatures are expected to

FIGURE 2.26: CPMG-*N* decoupling sequences with vary-
ing number *N* of π_y-pulses. "Ion B" shows signal related
to a ^{29}Si nuclear spin close to the investigated Ce^{3+} ion.
"Ion A" shows no ^{29}Si signature. Solid lines come from CCE
based ab-initio simulations of the corresponding dynamical
decoupling sequences.

exhibit *N* pronounced coherence dips with much larger depth as seen exper-
imentally. As the experimentally observed signatures are more shallow than
these direct theoretical predictions, several experimental effects are consid-
ered for the given CCE simulations, plotted in figure 2.26. Due to the high
density of Ce^{3+} ions in the YSO crystal, the main contribution to background
signal was previously discussed to emerge from other Ce^{3+} ions. As a conse-
quence, the noise spectroscopic signal can in principle result from more than
one Ce^{3+} ion simultaneously. While different Ce^{3+} ions within the same con-
focal spot share the same ^{89}Y nuclear spin environment, their ^{29}Si nuclear
spin environment can be quite different, based on the statistical occurance of

^{29}Si . For "ion B", this was accounted for by simulating two Ce^{3+} ions within a $13 \times 5 \times 6$ nm^3 lattice, where only one Ce^{3+} ion has a proximal ^{29}Si located at a distance of 3.6Å. Simulations for "ion A" assumed only one Ce^{3+} with no proximal ^{29}Si in a distance smaller than 6Å. Based on CCE simulations,

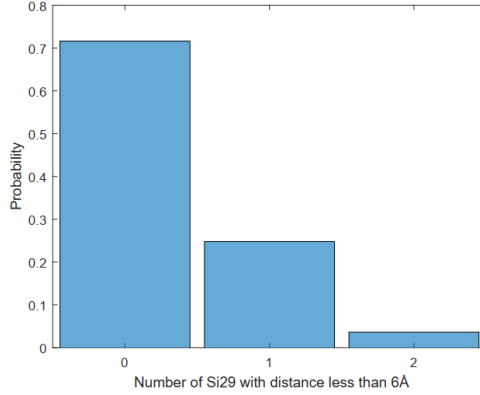
FIGURE 2.27: Probability for a Ce^{3+} ion in YSO crystal to have a certain number of ^{29}Si nuclear spins located at a distance smaller than 6Å.

we cannot distinguish between one or two coupled ^{29}Si located at a distance closer than 6Å from the Ce^{3+} ion for the performed decoupling sequences. However, it is far more likely to sense exactly one ^{29}Si nuclear spin, visualized in figure 2.27, where we have estimated the likelyhood to detect no ^{29}Si at all to more than 70%, exactly one ^{29}Si to roughly 20%, or two ^{29}Si nulcear spins to less than 5%. The given probabilities match well with experimental results, where out of a dozen investigated single Ce^{3+} ions, two showed ^{29}Si nuclear spin coupling. Further reductions in depth of signal can arise from external noise for proximal ^{29}Si , such as external magnetic field fluctuations, introduced by MW manipulation to Ce^{3+} for example. Other potential broadening mechanisms of the ^{29}Si spin include the optical initialization as described for the nitrogen vacancy center [98] and residual rare-earth Kamers ion impurities (such as Er^{3+} , Yb^{3+} ,...), which can act as a noise

source on a short timescale. In order to take external noise into account, a relaxation and dephasing mechanism were phenomenologically added to the dynamics of ^{29}Si in the following fashion [98, 99, 100]:

$$\dot{\rho} = \mathcal{L}_{\mathrm{coh}}\rho + \gamma_2^{\mathrm{Si}}\left(\sigma_{\mathrm{Si}}^z\rho\sigma_{\mathrm{Si}}^z - \rho\right) + \frac{\gamma_1^{\mathrm{Si}}}{2}\left(\sigma_{\mathrm{Si}}^x\rho\sigma_{\mathrm{Si}}^x - \rho\right) + \frac{\gamma_1^{\mathrm{Si}}}{2}\left(\sigma_{\mathrm{Si}}^y\rho\sigma_{\mathrm{Si}}^y - \rho\right), \tag{2.34}$$

where a Lindblad master equation for the density matrix of the nuclear spin ρ was derived, with $\mathcal{L}_{\mathrm{coh}}\rho = -i\left[H,\rho\right]$, $\sigma_{\mathrm{Si}}^{x,y,z}$ as the Pauli matrices of the proximal ^{29}Si nuclear spin, and γ_1^{Si} and γ_2^{Si} as the relaxation and dephasing rates. The given CCE simulations plotted in figure 2.26 use $\gamma_1^{\mathrm{Si}} = \gamma_2^{\mathrm{Si}} = 64$kHz, extracted from fitting procedures. These values range in the same magnitude as the ones found for the nitrogen vacancy center in diamond [98].
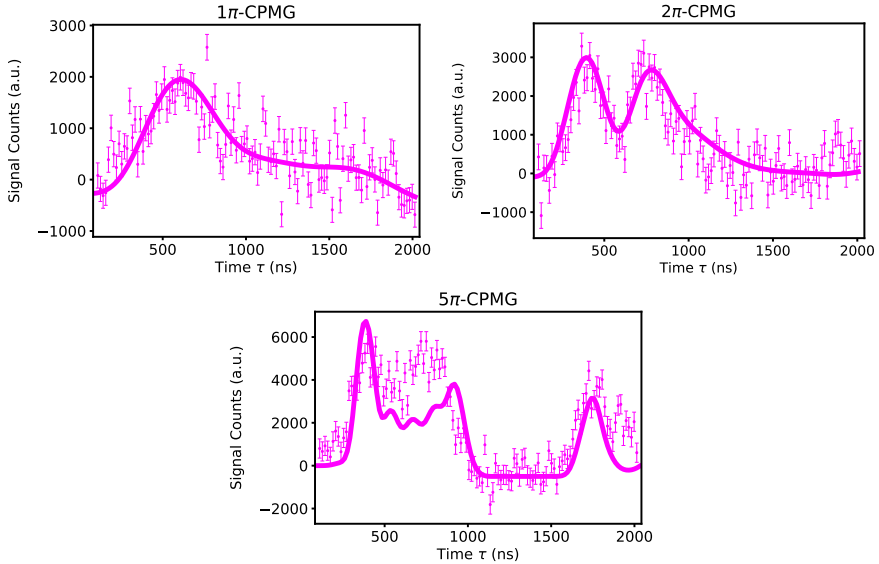

FIGURE 2.28: Differences between "ion A" and "ion B" measurement data and simulations are shown and represent only the ^{29}Si signal without overlapping ^{89}Y modulation.

In figure 2.28, the ^{29}Si nuclear spin signal is extracted by taking the difference of the signals between "ion A" and "ion B" plotted in figure 2.26. Since the ^{89}Y signal is identical for all Ce^{3+} ions, this leaves only the differences in the respective local environments of the ions under study. For $N = 2$, the expected splitting of the decoherence feature can also be seen for the case of ^{29}Si nuclear spin, similarly to what was shown for ^{89}Y in figure 2.25. For the case of $N = 5$, the CCE based simulation and the experiments show small discrepancies and represent the highest order decoupling sequence used for studying Ce^{3+} electron spin environment.

On the one hand, these measurements demonstrate the capabilities to localize a coupled ^{29}Si nuclear spin within the nearest neighbor position of Ce^{3+} ("ion B"). On the other hand, the comparison spectrum reveals information about the absence of ^{29}Si within a distance of 6Å to the Ce^{3+} ion. Finding a Ce^{3+} ion with the same nuclear spin environment as "ion A" has a probability of $\sim 70\%$.

2.8 Ce^{3+}:YSO - Conclusion and Outlook

In this chapter, we have shown measurements, that evaluate the capabilities of Ce^{3+} :YSO as optically accessible interface based on its electron spin properties for sensing single nuclear spins.

We start by demonstrating confocal microscopy and superresolution microscopy of Ce^{3+} :YSO, that allows for studying Ce^{3+} ions on the individual ion level. Based on optical polarization selection rules, we have shown optical spin initialization, optical spin readout and optically detected magnetic resonance experiments. Access to the Ce^{3+} electron spin was used for further demonstration of coherent control of individual electron spins, revealing T_2 times exceeding 100μs under spin echo sequences. These coherent interaction times turned out to be sufficiently long to probe the nuclear spin environment of single Ce^{3+} ions. Nuclear spins coupled to Ce^{3+} by magnetic dipolar interaction and located nearby the Ce^{3+} electron spin were thus measured.

The high density of ^{89}Y in the host crystal poses the challenge to distinguish spectrally between individual ^{89}Y nuclear spins in the future. One possibilty to improve the detection of nuclear spin signals, which tend to be submerged by a noisy spin bath are carefully designed dynamical decoupling sequences [101]. For a single ^{29}Si nuclear spin residing within the nearest neighbor shell, ^{29}Si sensing was demonstrated.

Any nuclear spin in proximity to the Ce^{3+} ion can be regarded as quantum resource for quantum memory protocols. In order to gain access to these spins, their initialization is an important step. One possibilty to render these spins accessible is the application of polarization transfer techniques, such as Hartmann-Hahn double resonance techniques [102]. In this context, one key concern is the coherence time of nuclear spins. Without regarding frozen core effects, which can potentially prolong nuclear coherence times [95], the ultimate limitation for nuclear spin coherence times is the interaction with the nuclear spin bath. Based on the weak dipolar interaction between nuclear spins in YSO relative to the Zeeman energy at the applied magnetic field, the only significant effect on decoherence can be caused by pure-dephasing interaction [50]. Estimated from nuclear spin dipolar interaction, the characteristic decoherence time scales are $T_{2,\text{Si}}^* \sim 10$ms for ^{29}Si nuclear spins and $T_{2,\text{Y}}^* \sim 50$ms for ^{89}Y nuclear spins.

As outlook, this work motivates the realization of controllable multispin quantum registers based on single rare-earth ions embedded in a YSO matrix. These findings are applicable to other Kramers ions doped into YSO, such as Er^{3+} , which is particularly interesting for quantum telecommunication applications. Furthermore, access to environmental spins, which act as local nodes were shown to provide extended functionality for quantum memories, such as quantum error correction [48].

Chapter 3

Deterministic Single Rare-Earth Ion Implantation Doping

This chapter deals with deterministic doping of single ions into a solid-state host material within the frame of a collaborative project, conducted together with colleagues from University of Mainz. The synergetic structure of the project combines the expertises regarding single ion implantation on the one hand, with single ion detection on the other hand, and enabled us to show unprecedented results. The experimental work is distinctly split into single ion implantation with an experimental setup developed by colleagues from University of Mainz and primarily handled by my esteemed colleague Karin Groot-Berning. The postprocessing of samples and their optical characterization was performed by me and will thus be the center of attention throughout this chapter. First, a motivation for conducting this study will be given. Then, the experimental apparatus used for ion implantation will be introduced. Further, experimental method and setup used for optical characterization of implanted samples are presented. A material annealing study

is presented, discussing the probability of rare-earth ions to obtain a fluorescent charge state after implantation doping into the host material. I conclude with a quantification of implantation device specifications, such as precision and accuracy of single ion implantations, derived from sample characterizations.

3.1 Introduction

Single quantum systems are at the heart of quantum information processing. The development of deterministic single ion implantation methods with nanometer resolution may enable the fabrication of solid-state quantum devices with scaling architectures. A prominent example of such a solid-state based single quantum system are single phosphorus dopants in silicon [103, 104] or pairs of phosphorus dopants representing two interacting spin-qubits [105, 106], which are integrated in nanometer sized control and readout electronics. Alternatively, optically accessible, dopant related single defect centers located in crystalline hosts [107, 36, 108] are also among the systems proposed for quantum information processing and allow for integration into photonic circuits [109, 110, 111, 18, 112, 19]. Based on proposed quantum applications, the deterministic placement of single dopants into nanostructured devices emerged as critical element of fabrication procedures and it motivated the development of various techniques specifically designed for the silicon material system, such as STM based lithography [113] or single ion impact detection mediated by an active substrate [114]. The crystalline host materials of rare-earth ions and spin-active color centers, however, inhibit the application of these specialized techniques, and require an alternative technique for deterministic doping.

To this end, a versatile single ion implantation method with inherently deterministic nature was developed by colleagues from University of Mainz. As sketched in figure 3.1, it is based on trapping single ions in a segmented
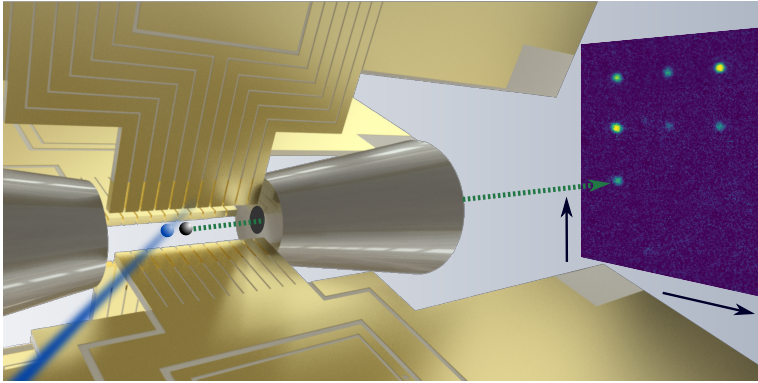
FIGURE 3.1: Placing Single Impurities into a Crystal. Sketch of the deterministic single rare-earth ion implantation technique.

Paul trap and grants substrate-independent deterministic implantation doping without need of ion substrate interaction to verify the number of implanted ions. Furthermore, a broad range of implantation energies and implanted ion species [115, 116] can be realized with the method and its application and performance is presented in the following.

3.2 Single Ion Implantation Setup Based on a Paul Trap

The experimental apparatus, which facilitates the rare-earth ion implantations is a deterministic single ion implantation setup, depicted in figure 3.2. It was developed by colleagues from University of Mainz and detailed descriptions can be found in reference [117]. In this chapter, I will merely describe key principles and requisite techniques and methods related to the apparatus, in order to give a comprehensive picture of the performed single rare-earth ion implantations, which shall be characterized by optical means thereafter. The centerpiece of the setup is an ion trap acting as a source for

single ions. As a consequence of Laplace's equation, the electric field potential has never a local maxima or minima and all extrema occur at boundaries. A three dimensional confinement of a charged particle thus cannot be accomplished by static electric fields only. The Paul trap design developed by Wolfgang Paul [118] makes use of an alternating electric field to achieve a dynamical confinement. The implementation of the ion trap follows the design of a segmented linear Paul trap, previously proposed by reference [119]. It allows for loading ions into the trap, where they in principle can be cooled to their motional ground state. In this state, their spatial uncertainty is defined by the Heisenberg limit, hence the smallest possible energy dispersion and it represents the ultimate limit on the obtainable spatial resolution for ion implantation [120].
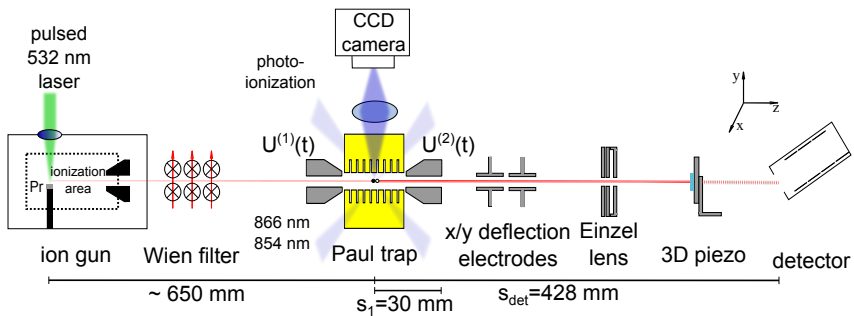
FIGURE 3.2: Sketch of the single-ion implantation setup.

The experimental procedure for single ion implantation starts with the generation and loading of ions into the Paul trap. As praseodymium is the rare-earth species of interest for optical characterization of the implantation technique, $^{141}\text{Pr}^+$ are generated in a commercially available ion gun (Specs IQE 12/38) modified to hold a praseodymium target (99.5% purity). For this, praseodymium is ablated by a laser pulse (532nm Nd:YAG laser , 1.2mJ pulse energy) and ionized under electron impact within the repeller electrode structure (figure 3.2, black dotted). Subsequently, praseodymium ions are accelerated by an extraction electrode to 600eV energy and passed through

a Wien filter. The Wien filter, in conjunction with optimized capture voltage sequences that accurately selects the mass-to-charge ratio of interest, allows praseodymium ions to enter the trap and filters out other unwanted ion species. The loading procedure for ^{141}Pr$^+$ ions then follows three precisely timed steps. First, a repulsive potential with $U^{(1)}(t) = 350$V, applied to the first endcap for $t = 40.9\mu$s, decelerates the ions. During the second step starting at $t = 41\mu$s, the first endcap is switched to $U^{(1)}(t) = -256$V in order to further decelerate ions, that leave the endcap bore. Note, that within the endcap bore, ions are shielded from electric fields. Simultaneously, a repulsive potential of $U^{(2)}(t) = 3000$V is applied to the second endcap. Both voltages during the second step are applied for 70ns and then switched to ground potential. At the same time, the third step starts by confining ions within the Paul trap in radial and axial potentials. In fact, mixed ion crystals consisting of ^{141}Pr$^+$ and ^{40}Ca$^+$ are loaded to the trap. The addition of ^{40}Ca$^+$ is achieved by trapping a random number of ions from a photoionized atomic beam of calcium emerging from a heated oven. Simultaneously, the praseodymium ions are injected. Discernible from figure 3.1, the Paul trap has an X-shaped configuration of four segmented electrodes, which are operated at a radio frequency of $\Omega_{\mathrm{rf}} = 2\pi \times 23.062$MHz with peak-to-peak amplitude $V_{\mathrm{pp}} = 572$V. This operation results in axial and radial mode frequencies of trapped ^{40}Ca$^+$ ions of $\omega_{\mathrm{ax,r1,r2}} = 2\pi \times \{0.45, 1.584, 1.778\}$MHz [115]. Once ^{40}Ca$^+$ ions are loaded to the trap, they are laser cooled on the $S_{1/2} - P_{1/2}$ transition and used to sympathetically cool the ^{141}Pr$^+$ ions.

Imaging the fluorescence of trapped calcium ions allows for accurate determination of the number of trapped ions, as shown in figure 3.3. This determination is based on an increase in inter-ion distance for a pure calcium ion crystal loaded to the trap when compared to a mixed ion crystal, consisting of calcium ions and an additional single praseodymium ion. For an ion number n in the trap of $n \geq 4$, the inter-ion distance difference is harder to observe. In these cases, the number of calcium ions in the trap is reduced by applying predefined voltage sequences to trap segments in order to ensure
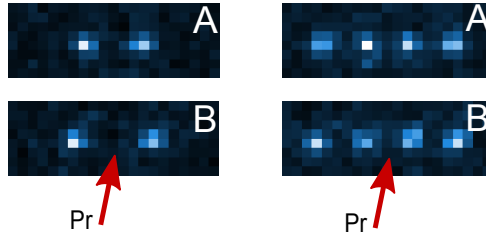
FIGURE 3.3: Fluorescence of ions imaged. (A) Pure $^{40}Ca^+$ crystals; the distance between two $^{40}Ca^+$ ions is 9.5μm. (B) Crystals containing an additional $^{141}Pr^+$ ion.

a clear identification of praseodymium. Once a loaded praseodymium ion has been verified, the number of loaded ions is reduced to exactly one $^{141}Pr^+$ and one $^{40}Ca^+$ by a predefined voltage sequence of the axial trap sequence.

Subsequently, the ions are extracted from the trap with an energy of 5.9keV, by applying an acceleration voltage of $U^{(2)}(t) = 5900$V to the second end-cap. The axial component of the potential can alter the kinetic energy of the ion and in order to avoid chromatic abberations, which can cause a broadening of the implantation spot size, the extraction is phase-synchronized with the applied radio frequency. Both, calcium and praseodymium ions are extracted together, passed through deflection electrodes for steering purpose into the center of an electrostatic einzel lens, which focuses the extracted ions into a small spot. Since the mass-to-charge ratios of the two ion species differ significantly, different ion trajectories cause $^{141}Pr^+$ to impinge upon the sample surface several μm away from $^{40}Ca^+$. In order to extract a focal spot size of the ion microscope, a profiling edge is moved through the focal plane of the ion beam by a piezoelectric translation stage and the number of transmitted ions is recorded. For this measurement, a Bayesian experimental design was used [115], which optimizes the picked positions of the profiling edge. In order to obtain a posterior likelihood function, the Bayesian approach for parameter θ estimation makes use of Bayes' theorem $p(\theta|y,\xi) = p(y|\theta,\xi)p(\theta)/p(y|\xi)$, where $p(\theta)$ represents a

prior likelihood function, and $p(y|\theta,\xi)$ represents the statistical model function of the measurement. For the specific case of measuring the focal spot size, the measurement can be modeled as convolution of the transmission function of the imaged profiling edge and the Gaussian ion beam profile. $p(y|\theta,\xi)$ then gives the probability to observe an outcome $y = \{0,1\}$ for given parameter values θ; in the case of the focal spot size the given parameters are beam position, beam radius and detector efficiency for example. The free control parameter ξ is represented by the profiling edge position and is the free optimization parameter. $p(y|\xi)$ is used for normalization, with $p(y|\xi) = \int p(y|\theta,\xi)p(\theta)d\theta$. The information gain of a measurement $U(y,\xi)$ can be quantified by the difference in Shannon entropies $U(y,\xi) = \int \ln[p(\theta|y,\xi)]p(\theta|y,\xi)d\theta - \int ln[p(\theta)]p(\theta)d\theta$ and the average over measurement outcomes $U(\xi) = \sum_{y\in\{0,1\}} U(y,\xi)p(y|\xi)$ then yields a quantity solely optimizable with ξ. The approach carries the advantage of an unfixed sample size, where further sampling can be stopped at any time based on evaluated data, while maximizing the information gain, which makes it an efficient approach compared to a stepwise or sweeping method. This is particularly useful for experiments with low repetition rate, such as the one at hand.

Spot size measurements for $^{141}Pr^+$ and $^{40}Ca^+$ are shown in figure 3.4 and they reveal a beam waist radius for calcium of $\sigma_{Ca} = 11.3 \pm 2.0$nm and for praseodymium of $\sigma_{Pr} = 30.7 \pm 8.5$nm. For calcium, the spot size was identified to be dominated by mechanical vibrations [115]. Praseodymium on the other hand exhibits a much larger beam waist radius, which can originate from an increased motional wave packet size, which is corresponding to an increased mean phonon number of radial modes. These circumstances could be explained by the reduced sympathetic cooling rate for large differences in mass-to-charge ratios of mixed-species ion crystals, ranging at $141/40 \approx 3.52$ in our specific case [121].

An average rate of approximately 1 ion per minute for loading, identification, cooling and extracting single $^{141}Pr^+$ ions was achieved during experiments
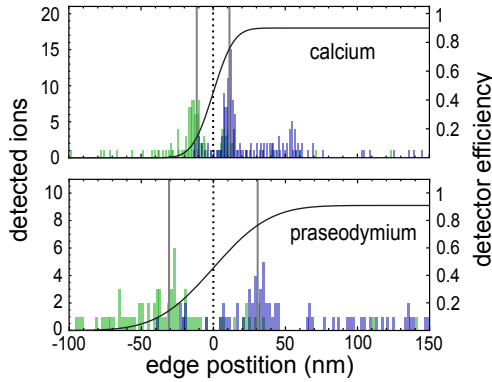
FIGURE 3.4: Histograms of the spot size measurements for $^{40}Ca^+$ and $^{141}Pr^+$ ions. The events of the single ion extraction are split into two groups. The blue group represents the detected ions and green group represents the blocked ions. The black line shows the Bayesian fit function corresponding to the last measured parameter set for beam position x_0, radius σ, and detector efficiency a. The mean value of beam positions on the x-axis is set to $x_0 = 0$ (dotted line), and the gray lines indicate the 1σ radius of the beam waist, which amounts to $\sigma_{Ca} = 11.3 \pm 2.0$nm for calcium and $\sigma_{Pr} = 30.7 \pm 8.5$nm for praseodymium. Calcium ion extraction took approximately 15 minutes for 308 ions. Praseodymium ion extraction took approximately 2 hours for 150 ions.

with the described setup. Samples were prepared by implanting $^{141}Pr^+$ into an ultra-pure YAG ($Y_3Al_5O_{12}$) crystal, which was mounted on the three-axis piezoelectric translation stage. This allowed for implantation of dot-grid patterns with an implantation energy of 5.9keV, corresponding to an implantation depth of $\sim$ 5nm [122], depicted in figure 3.5. In order for praseodymium ions to reach the fluorescent trivalent charge state, the sample was annealed in air at 1200°C for approximately one minute. The exact procedure can be found in appendix A.2.
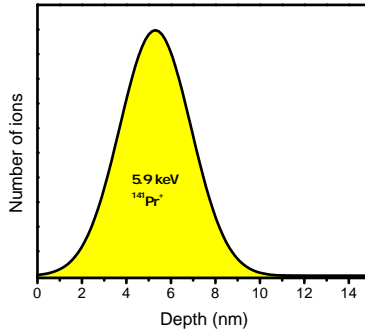
FIGURE 3.5: Ion depth distribution for ^{141}Pr$^+$ implantation
into YAG crystal with energy of 5.9keV.

3.3 Optical Microscopy of Single Pr^{3+} Ions

In general, the verification of a single ion implantation into a solid state host
material poses a challenging task due to the associated need of detecting the
single dopants. An answer to this problem is the creation of single dopant
related color-centers, that can be detected optically [107, 36, 108]. Determin-
istic color center generation in our experiments comprises the single ^{141}Pr$^+$
ion implantation and the subsequent incorporation of praseodymium into
the YAG crystal lattice in the fluorescent trivalent charge state by adequate
annealing. In order to verify this process, optical detection of Pr^{3+} on the
single emitter level is performed [36]. The microscopy method is based on
a two-photon up-conversion process [123], which allows for maximizing the
fluorescent emission by enhancing the efficiency of the excitation-emission
cycle of Pr^{3+} .

Principally, the non-linear process of upconversion by energy transfer in-
volves the emission of light with shorter wavelength, when compared to the
excitation wavelength [124]. For the system of Pr^{3+} :YAG, there are multiple
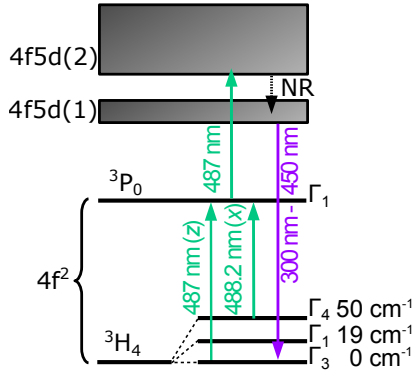ways to realize a two-photon upconverting excitation scheme [125], based

FIGURE 3.6: Electronic level structure of Pr^{3+} in a YAG crystal. The three lowest $^3H_4$ crystal field levels have symmetry representations Γ_3 ($0\,cm^{-1}$), Γ_1 ($19\,cm^{-1}$), and Γ_4 ($50\,cm^{-1}$).

on the electronic level structure shown in figure 3.6 [126]. In our experiments, we employed a two-step upconversion with a single laser at 487nm wavelength[127]. In the first step, the parity-forbidden $4f \leftrightarrow 4f$ transition originating from the $^3H_4$ ground state and ending up at the intermediate $^3P_0$ shelving state is driven. The electron exhibits a lifetime of $8\mu s$ in the $^3P_0$ state and during this time period, it can be excited further. Accordingly, the second excitation step promotes the electron from the $^3P_0$ state to the $4f5d$ level, via a parity-allowed optical transition. Through non-radiative decay, the electron ends up in the lowest $4f5d(1)$ level, from where it can decay optically to $4f$ states. These parity-allowed optical transitions yield ultraviolet emission in a spectral range between 300nm and 450nm with close to unity quantum efficiency [128].

The detection of single Pr^{3+} ions in YAG [36] in a home-built upconverting microscope is thus facilitated by two important facts. The short lifetime of the $4f5d$ level of about 18ns translates into a high emission rate of UV photons originating from the $4f5d \leftrightarrow 4f^2$ transition. Secondly, two-photon upconversion microscopy enables virtually background-free imaging. Laser light is commonly rejected by optical filters, separating the strong flux of
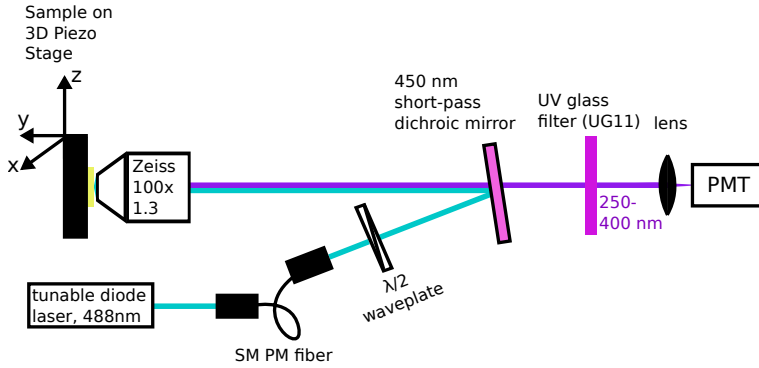
FIGURE 3.7: Experimental upconverting microscope setup for detection of Pr^{3+} in YAG. PMT: Photomultiplier tube. SM PM fiber: Single-mode polarization-maintaining fiber.

laser photons from the UV signal. Specifically, other fluorescing impurities residing in YAG apart from Pr^{3+} are typically not upconverting to the UV under 487nm excitation, but rather contribute red-shifted fluorescence to the background, which is simultaneously filtered with the laser light. The microscope setup for this experiment is shown in figure 3.7. A tunable diode laser design based on prism feedback [36] was used to obtain tunable laser emission around a wavelength of 487nm. Laser light is coupled into a single-mode polarization-maintaining fiber. The transmitted portion after the fiber was collimated, sent through a $\lambda/2$-waveplate and reflected from a 450nm short-pass dichroic mirror. The laser beam is then focused by an oil immersion objective lens (Zeiss Fluar 100x,1.30 Oil UV) with specifically high transmission in the UV. The corresponding transmission curve is plotted in figure 3.8.

The sample, mounted on a three-axis piezoelectric translation stage, was then moved throughout the focus of the laser and the UV emission of Pr^{3+} is collected with the same objective lens. UV fluorescence is passed through
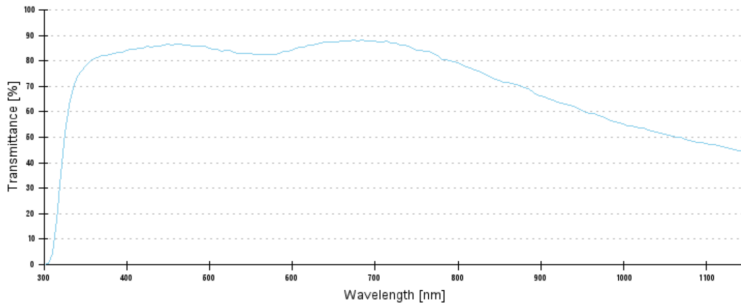
FIGURE 3.8: Transmission of the Zeiss Fluar 100x,1.30 Oil
UV objective as a function of wavelength.   From www.
micro-shop.zeiss.com

the dichroic mirror and filtered additionally by a bandpass filter (UG11, 250-
400nm), before being focused onto the photomultiplier tube detector (Hama-
matsu H11890-210, 30% detection efficiency at 400nm). The characteristic
pinhole used in confocal microscopes can be omitted in the upconversion
microscope, without losing the high resolution required for studying spatial
patterns of implantations. This is due to the non-linear intensity dependence
of the upconversion mechanism, which results in a well-confined focal plane
of the microscope.

In the context of single ion implantation, a cruicial point is the quantification
of implanted ions into the sample. In general, the fluorescence given by a
Pr^{3+} ion in YAG depends on the excitation light polarization and the specific
site of the crystal Pr^{3+} resides in, [129, 36]. An accurate measurement of
the number of fluorescing Pr^{3+} ions doped by ion implantation requires the
collected fluorescence signal of all Pr^{3+} ions to be rendered equal. In the
following, the procedure of imaging equivalently bright Pr^{3+} ions and the
related optical properties of individual Pr^{3+} ions in YAG are described.

Pr^{3+} dopants in YAG substitute Y^{3+} . In YAG crystals, six magnetically in-
equivalent orientations of Y^{3+} /Pr^{3+} sites can be found. They have a D_2

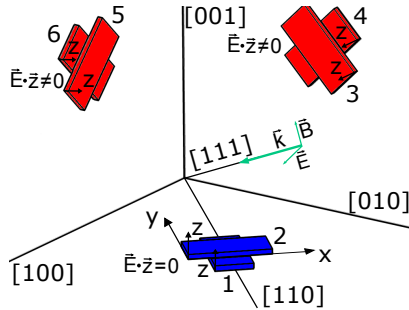FIGURE 3.9: Orientation of the six dodecahedral rare-earth ion sites in YAG, indicated by matchboxes. The polarization of the excitation laser propagating along [111] direction is adjusted such, that always two out of six sites are rendered non-fluorescent. Exemplarily shown are sites 1 and 2, which are not being excited by the laser. Simultaneously, sites 3-6 are excited with equal probability, leading to equal amount of fluorescent emission collected from these sites.

site-symmetry, where the local x, y, and z axis of site 1 of Pr^{3+} conventionally corresponds to the [110], [1$\bar{1}$0], and [001] direction, respectively. The other five sites are related by rotation about [111] and [001] axes and are labelled in analogy to site 1, with x as the longest, y the intermediate and z the shortest dimension of the matchboxes, shown in figure 3.9[130, 129]. The D_2 point group has four irreducible representations Γ_1, Γ_2, Γ_3, and Γ_4, based on the D_2 point group symmetry operations, under which the wavefunctions of Pr^{3+} must be invariant. Looking at electric dipole transitions between states with different representations, the selection rules shown in table 3.1 apply [126], which assignes the polarization direction related site axis to the dipole transition.

In general, the $^3H_4$ ground state of Pr^{3+} exhibits a nine-fold degeneracy if the free-ion is considered. The degree of degeneracy lifting depends only on the point symmetry about the ion. Due to low symmetry, the $^3H_4$ ground state of Pr^{3+} in YAG is crystal-field-split into nine levels. Out of these nine levels,

only from the lowest three levels (at $0\,\text{cm}^{-1}$, $19\,\text{cm}^{-1}$, and $50\,\text{cm}^{-1}$) absorption to higher levels was observed, even for temperatures up to 400°C [131]. This indicates, that only these lowest three levels are populated at room temperature and the next highest level exhibits a large energy seperation to the lowest three. According to calculations [126], the next higher level is located at around $500\,\text{cm}^{-1}$, inaccessible by room temperature phonons. Taking into account the symmetry representations of these three lowest $^3H_4$ crystal field levels with Γ_3 ($0\,\text{cm}^{-1}$), Γ_1 ($19\,\text{cm}^{-1}$), and Γ_4 ($50\,\text{cm}^{-1}$) and the representation of $^3P_0$ with Γ_1, we obtain either a $\Gamma_3 - \Gamma_1$ transition polarized along the z axis (blue, 487nm) or along a $\Gamma_4 - \Gamma_1$ transition polarized along the x axis (red, 488.2nm), as indicated in figure 3.6. This allows to infer the absorption

	Γ_1	Γ_2	Γ_3	Γ_4
Γ_1	-	y	z	x
Γ_2	y	-	x	z
Γ_3	z	x	-	y
Γ_4	x	z	y	-

TABLE 3.1: Electric-dipole selection rules for D_2 symmetry.

cross-section for a dipole transition with respect to the excitation light polarization, given by the projection of the dipole direction onto the electric field vector of the excitation light.

In our specific case, the YAG crystal surface is perpendicular to the [111] direction and the electric field vector of the excitation light lies in the same plane as the crystal surface, as indicated in figure 3.9. When working with the z dipole, perfectly circularly polarized light can in principle excite all six magnetically inequivalent sites with equal efficiency. This can be seen from all z dipole projections onto the [111] direction being equal and thus their projection onto a surface perpendicular to [111], representing the plane of the electric field vector of the circular polarized light, must also be equal. Based on distortions emerging from the objective lens and the dichroic filter used in the microscope setup, the circular polarization of the light can degrade and

cause systematic errors. For this reason, linearly polarized excitation light was used during investigation of single Pr^{3+} and for the [111]-cut YAG we find a threefold symmetry, where two out of six z dipoles are always aligned parallel. If the light polarization is chosen such that two sites are yielding no fluorescence (extinction), the other four are found to have equal brightness. By collecting laser scans for all three excitation polarizations, we can thus obtain quantifiable fluorescence data from all six possible sites of Pr^{3+} by adding up the scans. The x dipoles on the other hand are unpractical for quantification purpose. Using the x dipoles, only one site can be rendered dark, for one specific linear excitation light polarization. This would leave a six-fold symmetry to adjust light polarization based on extinction of single Pr^{3+} ions. More importantly, however, is the fact, that Pr^{3+} ions would yield unequal fluorescence even after averaging over all six linear polarizations. This behavior prohibits accurate quantification.

Adding up scans for quantification only works, if the individual Pr^{3+} ions are all located at the same depth. This is exactly the case for the ions of interest, as the implantation depth of $\sim 5.3 \pm 1.6$nm is the same for all of them and their longitudinal distribution is well within the z-resolution of the microscope.

Following the procedure of taking three scans and adding them up, an up-converting laser scan is obtained and shown in figure 3.10. The optical resolution of the microscope was determined from the average width c of two dimonesional Gaussian fits to single Pr^{3+} ions based on the following expression:

$$f(x,y) = A \cdot \exp\left(\frac{-(x-x_0)^2 - (y-y_0)^2}{2c^2}\right) + B, \tag{3.1}$$

where A represents the amplitude, B the offset, and (x_0, y_0) the center of the Gaussian function. A resolution of $c = 115 \pm 3$nm was found. In Figure 3.10, implanted Pr^{3+} ions can not be distinguished from other Pr^{3+} impurities, naturally found in the crystal, which is the main limitation of imaging quality
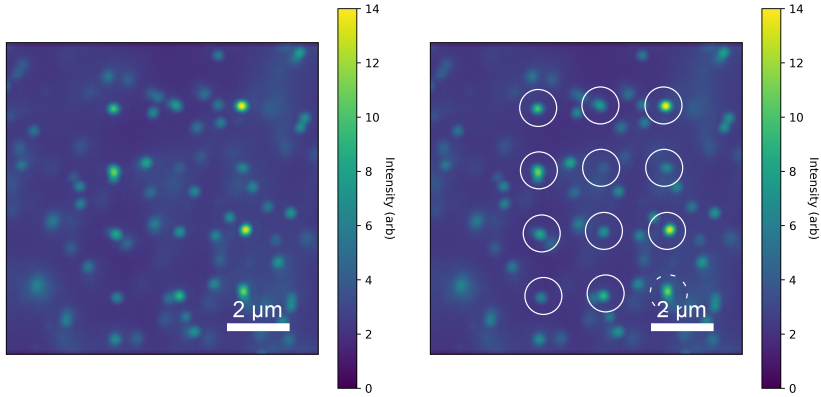
FIGURE 3.10: Upconverting laser scan taken at an implanted location (area *A*) of the crystal. In the image on the left side, implantation locations cannot be determined undoubtedly, since implanted Pr^{3+} ions can not be distinguished from other Pr^{3+} impurities, naturally found in the crystal. In the image on the right side, white circles are drawn to suggest implantation locations.

and prevents accurate quantification. Within approximately the first $1.5\mu m$ below the surface, we determine a background density of Pr^{3+} ions of 6×10^{11} cm^{-3} or 0.04ppb relative to yttrium.

3.4   Nanometer-Resolution Color-Center Generation

Preexisting, native Pr^{3+} ions are indistinguishable from implanted ones and represent a significant source of error for quantification of implantation-doped Pr^{3+} . It is therefore necessary to mitigate the influence of background Pr^{3+} ions by mapping their position prior to the praseodymium ion implantation. With precise knowledge about location and brightness represented by a background map, a background subtraction can be performed on scans, taken after implantation and subsequent annealing.

To this end, a high-resolution background map covering an area of 90 ×
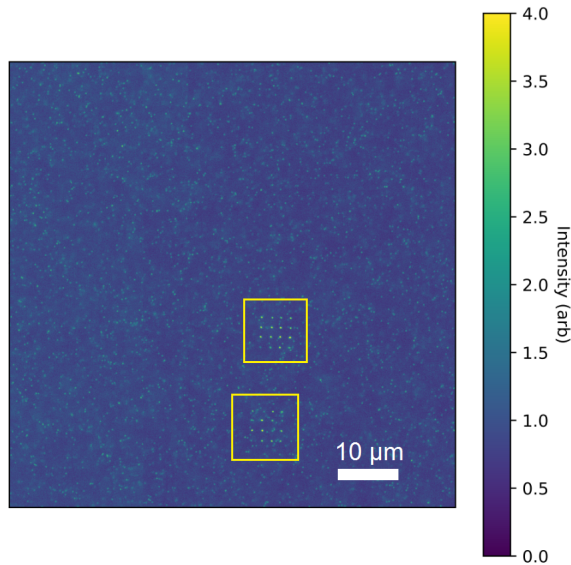
FIGURE 3.11: Background map: High-resolution upconverting microscopy scan taken at a designated location of the sample covering an area of $90 \times 90 \mu m^2$. Two 4×4 grid patterns are discernible, which are preceding single ion implantation dopings, utilized for marking the location of interest and as point of reference for the depth of implantation doped Pr^{3+} ions during optical characterization. Grids are marked with yellow squares.

$90 \mu m^2$ was taken, and is shown in figure 3.11. In order to obtain only information about preexisting Pr^{3+} ions at the depth of interest, 4×4 grid patterns were created by single ion implantation doping and annealing prior to background mapping, marked with yellow squares in figure 3.11. The grid patterns feature bright spots at the depth of implantation and they were used as reference points, which allowed to account for spatial drifts in the experimental setup throughout optical characterization. Specifically, by autofocusing on the same spot in regular intervals, the drift was quantified and

compensated. Also, the annealing step at up to 1200°C needed for the creation of Pr^{3+}, inhibited the use of metal markers on the surface of the YAG crystal. Instead, the grid patterns were used as landmarks to designate the location of the background map.
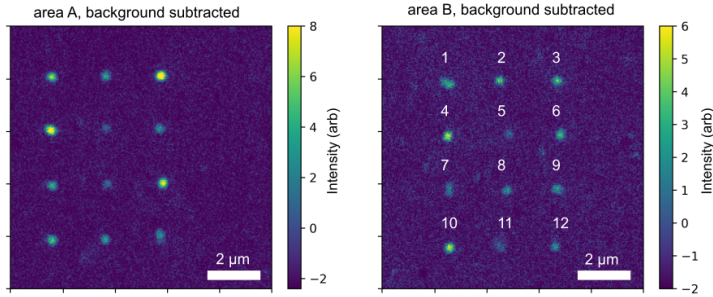
FIGURE 3.12: Upconverting microscopy scans of area *A* (left) after subtraction of the background map. Right: Area *B*, after subtraction of the background map.

After recording the background map, the sample was implanted with single praseodymium ions on two specific locations. Area *A* was implanted with eight praseodymium ions per spot on a 4×3 grid pattern and an additional spot with three ions, which makes in total 99 implanted ions. Area *B* was implanted with four praseodymium ions per spot on a 4×3 grid pattern, except of spot no. 12 (see numeration in figure 3.12), where only two ions were implanted, which makes in total 46 ions for this area. After the annealing procedure, the implantation patterns on neither area *A*, nor *B* are clearly visible in upconverting microscopy scans shown in figure 3.10 (area *A*) and in figure A.1 (area *B*). Through application of the background subtraction procedure (detailed information are given in appendix A.3), we can extract the signal of the newly generated Pr^{3+} ions for areas *A* and *B*, shown in figure 3.12. By summing up the collected Pr^{3+} fluorescence on each individual spot of the bachground-subtracted data and comparing it to the average summed up single Pr^{3+} ion fluorescence, we find approximately integer multiples of

the single Pr^{3+} ion count rates on the implanted spots. For experiments on area A, the average single ion fluorescence amounts to $C_A = 395 \times 10^3$ counts and on area B, it amounts to $C_A = 334 \times 10^3$ counts. The spot number dependent fluorescence signal for areas A and B is given in figure 3.13. Detailed lists of data used in this figure are also given in the appendix A.2 and A.3. Accordingly, each spot is assigned an integer number of optically active Pr^{3+} ions, generated by deterministic single ion implantation.
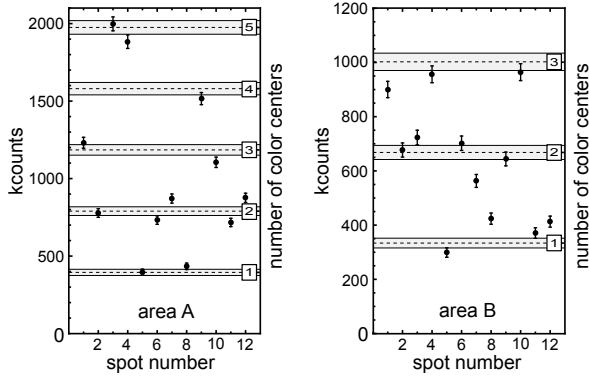
FIGURE 3.13: Summed up fluorescence signal (background-subtracted, in units of 10^3 counts $\equiv$ kcounts for 6ms integration time) of each implanted spot for areas A and B. The observed count rate is consistent with the discrete nature of the integer number of Pr^{3+} emitters located in each spot. For the error bars, we assume Poissonian photon-counting statistics.

Based on this assignment, we can give the associated implantation yields for both areas, with 32% on area A and 50% on area B. Previously found implantation yields of Pr^{3+} ranged between 91% for a 300keV high-energy implantation and 30% for a 75keV implantation, both with a dose of 10^{12} ions/cm^2 [21]. In this context, the results can also be compared to vacancy-based defect centers, such as the nitrogen vacancy in diamond, for which implantation yields between 2.5% [132] and 33% [133], with optimized annealing and creation procedure for an implantation energy of 30keV, were reported. Also,
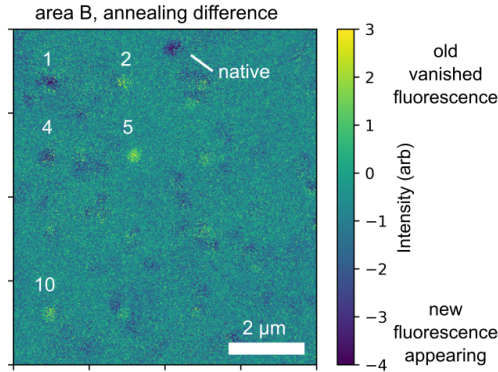
FIGURE 3.14: Difference between Pr^{3+} fluorescence signal before second annealing step and after. Map was taken on area *B*. Changes occuring on implantation sites are marked with the number of the spot.

for the silicon vacancy defect center in diamond, an implantation yield of approximately 2.5% was reported [134].

As the implanted praseodymium ions are known to be activatable into the fluorescent trivalent charge state with close to unity yield, the annealing process for the 6keV-implanted ions is investigated further. To this end, we annealed the implanted sample a second time under the same conditions, and imaged the implantation area *B* again afterwards. By taking the difference between Pr^{3+} ion fluorescence signals *before* and *after* annealing $\Delta C = C_{before} - C_{after}$, we can track changes in fluorescence that are related to the annealing step. The difference image is shown in figure 3.14 and was taken on area *B*. Apparent changes induced by the additional annealing step are predominantly located at the sites of implantation. At spots two, five, and ten, the observed fluorescence decreased by about the amount of fluorescence a single Pr^{3+} ion gives. Hence, the annealing step caused these ions to lose their fluorescent state. In spots one and four, respectively, an

additional Pr^{3+} ion appeared. Apart from activity observed on implantation sites, exactly one native Pr^{3+} ion emerged in an unimplanted location on a scanned area of approximately $100\mu m^2$. This allows the conclusion, that the annealing procedure has only a marginal effect on the native Pr^{3+} ions in the host material and that the background subtraction for obtaining implantation-specific fluorescence maps is a valid procedure. The fact, that the annealing step can cause both, native and implanted, ions to reach or lose their fluorescent state can in general be explained by diffusion. The diffusion rate at a temperature of $1200°C$ for praseodymium in YAG is approximately $2 \times 10^{-21} m^2/s$ [135]. Taking into account the annealing procedure (listed in appendix A.2), a lower boundary for the diffusion length can be estimated to approximately 1nm. Praseodymium ions located at a depth of 6nm can thus diffuse towards the surface and stabilize in a nonfluorescent charge state. While not at hand for our experiments, in principle, shorter annealing times can help to suppress this effect. The increased mobility of Pr^{3+} ions found in implanted sites can also stem from the elevated level of crystal damage, caused by implantation of ions. Even at a low implantation energy of 5.9keV, the crystal damage can be quantified to approximately 70 vacancies per implanted praseodymium ion [122], which need to be healed out at the elevated temperature of $1200°C$.

In the following, the implantation method will be characterized based on the upconversion microscopy scans shown in figure 3.12. Key measures of the doping method at hand are related to the spatial quality of placing single ions into the host material and can be divided into two parameters. Firstly, the spatial *precision* of the method will be discussed, which describes the statistical dispersion of ion locations under repeated implantation into one and the same spot, and quantifies the influence of random errors. And secondly, the spatial *accuracy* of the method describes the proximity of the implanted location to the true, projected location, and it takes into account the systematic errors.
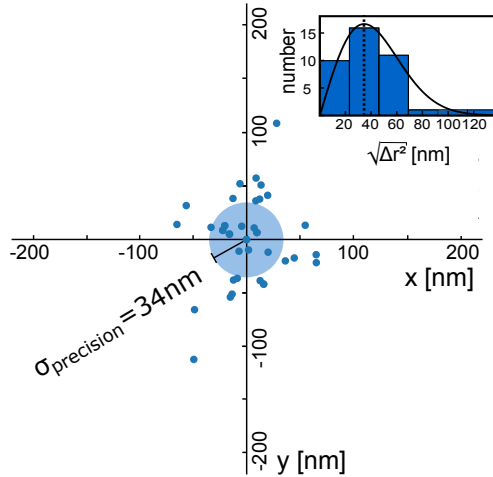
FIGURE 3.15: Precision of deterministic single ion place-
ment. Data points represent the Pr^{3+} ion locations with re-
spect to the centroid of each respective implantation site, ob-
tained from fitting two dimensional Gaussians. The mode
$\sigma_{precision} = 34$nm of the Rayleigh distribution is a measure
for the precision of ion placement. Inset: Histogram of the
radial distances of implanted ions to their center of mass.
Black curve represents the Rayleigh distribution of the data
found with the maximum likelihood method and the dotted
line the mode $\sigma_{precision}$.

In order to quantify the spatial precision, we extract the spatial variabil-
ity when implanting into a particular spot by fitting the data with a multi-
Gaussian, whereas the number of Gaussians corresponds to the number of
fluorescent praseodymium ions residing in the spot. According to the PSF of
the upconverting microscope, previously found by fitting two dimensional
circular Gaussians (see equation 3.1) onto native single Pr^{3+} ions, the multi-
Gaussians consisted of the sum of PSFs with a set width of 115nm. From
the fitting, we extract the positions of the PSFs, and plot their respective dis-
tances to the center of mass of the implantation site in figure 3.15. The shown
data set includes only Pr^{3+} ions located in spots with at least two ions and
it excludes data from implantation spots one, seven, and nine in area *B* and

spot twelve in area A. They were not accounted for, because these spots suffer from drifts far larger than the standard deviation of the rest of the implanted spots. We conjecture, that the probability to find such outliers is related to the overall settling duration of the implantation on one specific spot. Due to a low rate and high settling duration during this experiment, facility related external noise such as elevator induced vibrations can cause outliers to be implanted. Shown in the inset of figure 3.15 is a histogram of the radial distance to the center of mass of the studied Pr^{3+} ions in each respective spot, superimposed with a Rayleigh distribution found with the maximum likelihood method [136]. The mode of the distribution represents the value most likely to occur and amounts to $\sigma_{\mathrm{precision}} = 34$nm. It is indicative for the positioning stability of implanting several Pr^{3+} into the same spot and thus quantifies the precision of the technique.

The multi-Gaussian fitting method used for extracting the precision is furthermore examined with respect to the error it yields. Error estimations were done by Monte Carlo simulation of measurement data and a subsequent application of the fitting method under study. In detail, data spots containing between two and five ions were generated and randomly seeded noise with measurement-equivalent amplitde was added in each iteration separately. The results of the multi-Gaussian fitting to the datasets were statistically analysed and their positional variance, respective to the number of ions in the spot is given as the error of the method, shown in figure 3.16. Here, the dependence of the error σ on the mean ion distance from the center of mass $\sqrt{\Delta r^2}$ was investigated. The analysis does not quantify the actual position of ions, but their average distance to the center of mass given by the multi-Gaussian fitting. If the fitting does not reproduce the actual position, but finds the same average distance to the center of mass, it also results in a low error. For the cases of two-ion spots and three-ion spots, representing 65% of the optical measurement results, the uncertainty of the method is not a function of the inter-ion distance. For four ions per spot, however, this
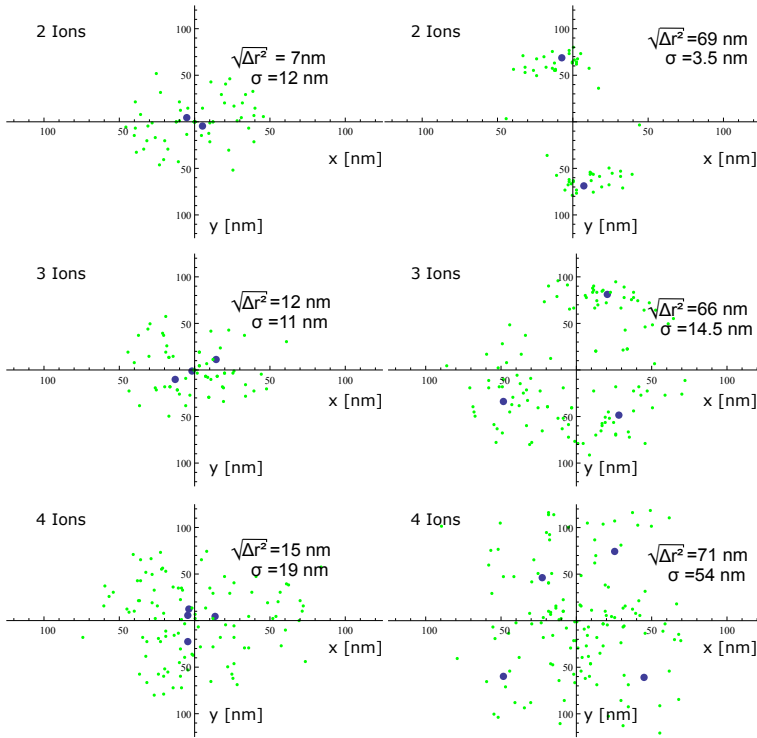
FIGURE 3.16: Monte Carlo simulations of fitting multi-Gaussians to two, three, and four ions per spots. The spatial variance, that quantifies the error of the method depends on the inter-ion distances. Blue data points mark the fixed positions of Pr^{3+} ions with respect to the center of mass. The green data points are fitted positions.

method shows an increase in uncertainty for the cases of large inter-ion distances. An average ion-number specific estimation error can be given with $\sigma_{2ions} = 6nm$, $\sigma_{3ions} = 20nm$, $\sigma_{4ions} = 24nm$, and $\sigma_{5ions} = 30nm$, for two, three, four, and five ions per spot, respectively. By taking into account the number of Pr^{3+} ions hosted in each optically measured spot, we find a total

error of the precision estimation method of $\sigma_{\text{precisionerror}} = 18\text{nm}$. In summary, the measured position stability of $\sigma_{\text{precision}} = 34 \pm 18\text{nm}$ is mainly influenced by the praseodymium beam size of about 30nm. Furthermore, uncertainties emerging from straggling and annealing-induced migration can potentially add to this value in a limited manner.
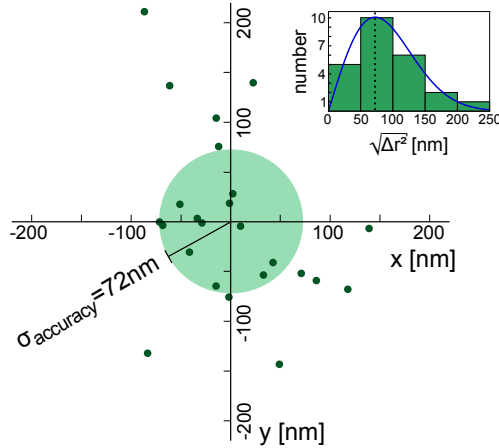
FIGURE 3.17: Calculated position difference between the implanted spots and the ideal grid positions. The mode $\sigma_{\text{accuracy}} = 72\text{nm}$ of the Rayleigh distribution is a measure for the accuracy of ion placement. Inset: Histogram of the radial distances of implantation spots to their ideal grid position. Black curve represents the Rayleigh distribution of the data found with the maximum likelihood method and the dotted line the mode σ_{accuracy}.

The patterning accuracy of the implantation method was quantified by estimating the deviation of the position of implantation spots from the desired grid. To this end, two dimensional Gaussian functions were fitted to the optically measured spots and based on their center positions, the distance difference to the ideal grid was calculated. The ideal grid has a spacing of exactly $2\mu m$ and the first implanted spot, acting as starting point, was not taken into account. The position differences are plotted in figure 3.17 and from the Rayleigh distribution of the radial differences we can find the mode

of the distribution $\sigma_{\mathrm{accuracy}} = 72\mathrm{nm}$, which characterizes the accuracy for array writing. To a large extent, the systematic errors, that contribute to the found uncertainty, come from nonlinearities of the piezoelectric translation stages (SLC-1720-S positioners, SmarAct GmbH), used for moving the YAG sample through the focus of the ion beam. According to manufacturer specifications, distortions of about 40nm are reasonable for the desired dot-grid spacing used in the experiment. Additionally, it should be noted, that the accuracy of placement on area B was noticeably worse in the y-direction, than for the x-direction. This suggests, that systematic long-term thermal drifts additionally influence the found accuracy.

3.5   Single Rare-Earth Ion Doping - Conclusion and Outlook

In this chapter, deterministic ion implantation and array writing of optically active, trivalent praseodymium ions in YAG was demonstrated. The spatial quality of placing these rare-earth ions and the generation yield was studied with upconversion microscopy.

We find between 30% and 50% of all implanted praseodymium ions to yield a photoactive Pr^{3+} color center. By annealing the sample, we can track down behavior of color center formation and relate it to implantation sites. The described method can act as tool to optimize annealing specific parameters on the single ion level in order to further improve generation yield and enable not just deterministic implantation, but also deterministic color center formation.

The characterization of the implantation method shows a positioning accuracy of 72nm and precision of $34 \pm 18\mathrm{nm}$. The achieved positioning accuracy is already sufficiently high for realizing arrays with 100-500nm separation, recently proposed for ^{31}P flip-flop qubits in silicon, which are based on electron-nuclear spin states [137]. Also, deterministic implantation of

single rare-earth ions into nanostructured hosts without residual rare-earth content, such as TiO_2, allows for precise engineering of emitter-photon coupling when working with optical cavities [111, 23]. With slight improvements in positioning accuracy, the method can be used to create topologically protected quantum optical systems based on subwavelength-spaced two dimensional photonic structures in solid state hosts [138]. With a few times improvement in the spatial quality of placement, single spins coupling to superconducting circuits [139] and direct coupling of ^{31}P nuclear spin qubits within 15nm distance, according to the Kane proposal, come into reach [140]

In the light of the technical reasons, such as the piezoelectric translation stage and thermal drifts, that are dominating the present accuracy of the technique, resolving discussed systematic errors can be anticipated. By additionally improving the symathetic cooling of trapped Pr^+ ions prior to extraction, one can reach the positioning regime, which is dominated by implantation-induced straggling. For an implantation energy of 5.9kV, the implantation depth and the corresponding depth uncertainty amounts to 5.3 ± 1.6nm. Related to lateral positioning, the radial range and corresponding uncertainty amounts to 1.8 ± 1.0nm [122]. A reduction of the acceleration voltage leads to lower implantation-induced positioning uncertainty. The current optical characterization technique will be of limited use for improved poisitioning quality. The application of superresolution microscopy techniques, which is available for Ce^{3+} in YAG, should allow for an implementation of a more suited optical characterization [84].

Chapter 4

Rare-Earth Ions Coupled to Microcavities

4.1 Introduction

The investigation of rare-earth ions in resonators in the context of quantum networks was largely motivated by a proposal from Kimble [15], originally written in the light of advances made in the field of trapped atoms in cavity quantum electrodynamics (CQED) experiments. In an analogy to trapped gas phase atoms fulfilling the key aspect of long coherence times due to their isolation from the environment, $4f$ electrons of rare-earth ions barely interact with their surroundings in the solid state. This makes them an attractive choice for integration into photonic structures. In this chapter, two different experimental platforms will be presented, both with their specific emphasis on solutions for realizing on-chip rare-earth ion based quantum architectures.
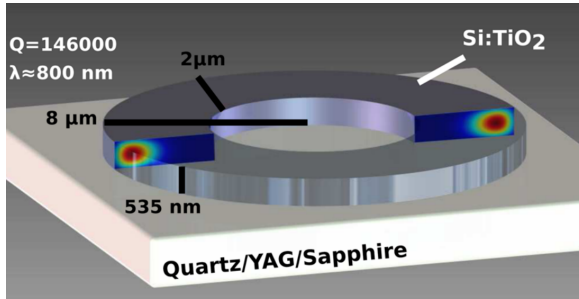
FIGURE 4.1: Resonator model with calculated electric field
profile of fundamental mode.

4.2   Basics: Rare-Earth Ions Coupled to Cavities

In this section, I briefly introduce the theoretical background pertinent to ap-
preciating the effect, that the presence of a cavity has onto an ion. Starting
with a very general picture, that describes any quantum decay, I will derive
the spontaneous emission rate of an ion in free space. The model will then
be used to understand how the spontaneous emission of the ion is modified
under addition of a weakly coupled cavity. In this context, the Purcell effect
is discussed and how cavities with low mode-volumes and high quality fac-
tors can be interfaced with rare-earth ions. FEM simulation-based resonator
and rare-earth emitter engineering is shown, which allows to maximize ex-
perimentally obtainable Purcell enhancements.

4.2.1   Spontaneous Emission without and with Cavity

The following treatment is inspired by Steck's notes on Quantum Optics
[141] and Fox's textbook [5], which both provide fine resources for this topic.

We start with a general picture of a two-level system with an initial state $|i\rangle$
and a final state $|f\rangle$. Here, $|i\rangle$ and $|f\rangle$ are eigenstates of the corresponding

rotating-frame free-evolution Hamiltonian:

$$\mathcal{H}_0 = \hbar\omega_{fi} |f\rangle \langle f| , \tag{4.1}$$

where $\hbar\omega_{fi} := E_f - E_i$ is defined as the energy difference of the initial and final states, with $E_i = 0$. Transitions of the system from $|i\rangle$ to $|f\rangle$ are induced by a constant perturbation Hamiltonian $\mathcal{H}_{\text{int}}$, that can be modelled by dipole interaction and is given by

$$\mathcal{H}_{\text{int}} = -\mathbf{d} \cdot \mathbf{E} \tag{4.2}$$

$$\underset{\text{RWA}}{=} \frac{\hbar}{2} \left(\frac{\langle f| \hat{\epsilon} \cdot \mathbf{d} |i\rangle E_0}{\hbar} |i\rangle \langle f| + \frac{\langle i| \hat{\epsilon} \cdot \mathbf{d} |f\rangle E_0}{\hbar} |f\rangle \langle i| \right), \tag{4.3}$$

where $\mathbf{d}$ is the atomic dipole operator and $\mathbf{E}$ the interaction field. The dipole operator is defined by the electron position $\mathbf{r}_e$ as $\mathbf{d} = e\mathbf{r}_e$ and based on parity arguments gives rise to vanishing diagonal matrix elements and can be decomposed into $\mathbf{d} = \langle i| \mathbf{d} |f\rangle |i\rangle \langle f| + \langle f| \mathbf{d} |i\rangle |f\rangle \langle i|$. It is the interaction field $\mathbf{E}(t) = \hat{\epsilon} E_0 \cos(\omega t)$ with angular frequency ω, that defines the transformation into the rotating frame, where $\hat{\epsilon}$ is the unit polarization vector of the field. The spatial dependence of the field can be omitted based on the dipole approximation, which assumes the wavelength of the field to be much longer than the size of the system, which, for example, is an ion with dimensions of Å. With the assumption $|\omega - \omega_{fi}| \ll \omega + \omega_{fi}$, the rotating-wave approximation can be made, which leads to fast optical frequencies being replaced by their zero average value. We thus obtain the rotating-wave approximated dipole interaction Hamiltonian in the rotating frame in equation 4.3.

The system state can be written as

$$|\psi\rangle = c_i |i\rangle + c_f |f\rangle , \tag{4.4}$$

where c_i and c_f contain the state's time dependence. The time evolution of the system can then be obtained by solving the time-dependent Schrödinger

equation $i\hbar\partial_t|\psi\rangle = (\mathcal{H}_0 + \mathcal{H}_{int})|\psi\rangle$, which yields a pair of coupled differential equations, and after decoupling by differentiation results in

$$\left(\partial_t^2 - i\omega_{fi}\partial_t + \frac{|\langle i|\,\mathcal{H}_{int}\,|f\rangle|^2}{\hbar^2}\right)c_i \;=\; 0 \tag{4.5}$$

$$\left(\partial_t^2 - i\omega_{fi}\partial_t + \frac{|\langle i|\,\mathcal{H}_{int}\,|f\rangle|^2}{\hbar^2}\right)c_f \;=\; 0. \tag{4.6}$$

Solving for the initial conditions of the system $c_i(0) = 1$ and $c_f(0) = 0$, we find the transition probability of the system to the final state as

$$P_f(t) = \frac{4|\langle i|\,\mathcal{H}_{int}\,|f\rangle|^2}{\hbar^2\omega_{fi}^2}\sin^2\left(\frac{\omega_{fi}t}{2}\right), \qquad (t \geq 0), \tag{4.7}$$

where the interaction was treated as a weak interaction, such that $|\langle i|\,\mathcal{H}_{int}\,|f\rangle| \ll |\omega_{fi}|$. In the long time limit for large t, we can replace the ω_{fi}-dependence by a delta function when normalizing in the following fashion $1/\omega_{fi}^2\sin^2(\omega_{fi}t/2) \to \pi t/2\,\delta(\hbar E_i - \hbar E_f)$. We obtain the transition rate from the time derivative, also known as *Fermi's Golden Rule*, as

$$\Gamma_{i\to\mathcal{F}} = \frac{2\pi}{\hbar}|\langle i|\,\mathcal{H}_{int}\,|f\rangle|^2\rho(E_f), \tag{4.8}$$

where the delta function was evaluated by integrating over a continuous range of energies. This implicit coupling to a set of final states $\mathcal{F}$ clears away the coherent Rabi oscillations induced by coupling to only one discrete state. Accordingly, the density of states $\rho(E) := dn/dE$, or the photon modes in free space in a large volume V is given by

$$\rho(E_f) = \frac{\omega_0^2 V}{\pi^2\hbar c^3}, \tag{4.9}$$

with $E_f = \hbar\omega_0$ as relevant energy of the initially excited ion. With only the vacuum field

$$E_{vac} = \sqrt{\hbar\omega_0/2\epsilon_0 V} \tag{4.10}$$

contributing to the electric dipole interaction, we find the transition rate in free space as

$$\Gamma^{\text{free}} = \Gamma_{i \to \mathcal{F}} = \frac{d_{if}^2 \omega_0^3}{3\pi\epsilon_0 \hbar c^3}, \tag{4.11}$$

where the factor $1/3$ emerges from averaging over a spherically symmetric ion, and $|\langle i| \mathcal{H}_{\text{int}} |f\rangle|^2 = E_{\text{vac}}^2 \cdot |\langle i| d |f\rangle|^2 = E_{\text{vac}}^2 \cdot d_{if}^2$ defines the transition moment d_{if}.

The free space transition rate of an ion can now be compared to the transition rate of a cavity-coupled ion. The cavity is assumed to have exactly one mode at frequency ω_c with a linewidth $\Delta\omega_c$ given by the quality factor $Q = \omega_c/\Delta\omega_c$. The density of states function $\rho(\omega_0)$ for the cavity (in resonance with the ion) is given by a Lorentzian of the form

$$\rho(\omega_0) = \rho(E)\hbar = \frac{2}{\pi\Delta\omega_c} \frac{\Delta\omega_c^2}{4(\omega_0 - \omega_c)^2 + \Delta\omega_c^2} \underset{\omega_0 = \omega_c}{=} \frac{2Q}{\pi\omega_0}. \tag{4.12}$$

The *Purcell factor* F_P is defined as the ratio between Γ^{free} and cavity-coupled transition rate $\Gamma^{\text{cav}} = \xi^2 (2Q d_{if}^2/\hbar\epsilon_0 V)$ (from Fermi's Golden Rule, equation 4.8), where the volume of the cavity is V [142]:

$$F_P = \frac{\Gamma^{\text{cav}}}{\Gamma^{\text{free}}} = \frac{3Q(\lambda/n)^3}{4\pi^2 V} \xi^2. \tag{4.13}$$

Here, $c/\omega = (\lambda/n)/2\pi$ with λ as the free space wavelength. The normalized dipole orientation factor is given by

$$\xi = \frac{|\mathbf{d} \cdot \mathbf{E}|}{|\mathbf{d}||\mathbf{E}|}. \tag{4.14}$$

It becomes aparent, that for $F_P > 1$, the spontaneous emission rate is enhanced by the cavity and the rate enhancement depends foremost on cavity-specific parameters, such as the mode volume V and the quality factor Q,

according to equation 4.13. Also, the resonance frequency of the cavity is required to match with the transition frequency of the ion, according to equation 4.12 and the dipole alignment with respect to the mode field is important to consider according to equation 4.14. The emission rate enhancement can be understood by the comparison of the density of states under the two different circumstances (free space, intra-cavity). The high density of states at the cavity resonance frequency is contrasted to the constant free space density of states. In analogy, a suppression of emission can be found for the off-resonant case, where the absence of photon modes inhibits spontaneous emission.

4.2.2   Whispering Gallery Mode Resonators

Whispering gallery modes were first described by Lord Rayleigh for sound waves travelling close to the walls of the spherically shaped St Paul's Cathedral [143]. His description explained, why whispers could be heard all across the gallery, hence the naming. The analogy for electromagnetic waves propagating in a spherically shaped dielectric material, shaped as a ring, disk or sphere and surrounded by air for example, can be understood by an optical mode confinement. A continuous total internal reflection at the interface between dielectric and air traps the light onto a whispering-gallery mode. Comprehensive treatments of whispering gallery modes are found in [144, 145], and [146].

As a solution of the Helmholtz equation in spherical coordinates, whispering gallery modes are conventionally divided into transversal electric TE ($\mathbf{E} \cdot z = 0$) and transversal magnetic TM ($\mathbf{H} \cdot z = 0$). When considering a cylindrical geometry, appropriate for microdisks and microrings, the Helmholz equation $(\nabla^2 + k^2)E_z = 0$ can be written for the axial field of a TM mode in cylindrical coordinates:

$$\left(\frac{\partial^2}{\partial r^2} + \frac{1}{r} \frac{\partial}{\partial r} + \frac{1}{r^2} \frac{\partial^2}{\partial \varphi^2} + k^2 \right) E_z(r, \varphi) = 0 \tag{4.15}$$

Separation of variables leads to two equations, one for the radial and one for the azimuthal dependence. These equations will be connected by the azimuthal mode number m, an integer number corresponding to the number of optical cycles the light field completes when travelling around the cyclinder-shaped resonator with radius R. Constructive intereference of light trapped within the cavity, in other words, resonances are possible when the condition

$$2\pi R = m \cdot \frac{\lambda}{n} \tag{4.16}$$

is met. Here, n is the refractive index.

From equation 4.15, the azimuthal part becomes

$$\left(\frac{\partial^2}{\partial \varphi^2} + m^2 \right) E_z(\varphi) = 0, \tag{4.17}$$

and has the solution $E_z(\varphi) = e^{\pm im\varphi}$. The equation for the radial part becomes

$$\left(\frac{\partial^2}{\partial r^2} + \frac{1}{r} \frac{\partial}{\partial r} + k^2 - \frac{m^2}{r^2} \right) E_z(r) = 0. \tag{4.18}$$

Solutions of Bessel's equation 4.18 are well-known and are either of the first kind J_m or second kind Y_m. Linear superpositions of these solutions $H_m^{(1)} = J_m + iY_m$ and $H_m^{(2)} = J_m - iY_m$ correspond to outward and inward propagating cylindrical waves. When only the outward propagating solution is considered, we find two solutions. One for within the resonator boundary ($r < R$) and one exterior to the boundary ($r > R$) [147]

$$\begin{align} E_z(r < R) &= A_m J_m(\widetilde{k}_1 r) \tag{4.19} \\ E_z(r > R) &= B_m H_m^{(1)}(\widetilde{k}_2 r), \tag{4.20} \end{align}$$

where A_m and B_m represent coefficients and $\widetilde{k}_j = n_j\widetilde{\omega}/c$ represents a complex mode propagation constant and frequency, with n_1 as refractive index within the resonator boundary and n_2 outside. They are obtained by solving the complex WGM dispersion relation (assuming an infinite cylinder), which follows from boundary conditions for $E_z(r)$ and its derivative at the interface $(r = R)$:

$$A_{1m}J_m(\widetilde{k}_1 R) = A_{2m}H_m^{(1)}(\widetilde{k}_2 R) \tag{4.21}$$

$$\widetilde{k}_1 A_{1m}J_m'(\widetilde{k}_1 R) = \widetilde{k}_2 A_{2m}H_m^{'(1)}(\widetilde{k}_2 R). \tag{4.22}$$

The dispersion relation then has the form

$$\widetilde{k}_1 \frac{J_m'(\widetilde{k}_1 R)}{J_m(\widetilde{k}_1 R)} = \widetilde{k}_2 \frac{H_m^{'(1)}(\widetilde{k}_2 R)}{H_m^{(1)}(\widetilde{k}_2 R)}. \tag{4.23}$$

As it is not a trivial task to solve the roots of such a dispersion relation, it is not uncommon to retreat to numerical simulations, in order to obtain the eigenvalue k of the complex propagation constant. The imaginary part of k represents the decay of a given mode, as the radiation can dissipate at the curved surface of a WGMR. This is quantified in the definition of the radiative quality factor

$$Q_{\text{rad}} = \frac{\text{RE}\,k}{2\text{Im}\,k} \tag{4.24}$$

In general, the quality factor defines the amount of dissipation present in a resonator and is defined as the lifetime τ of energy stored in it, as

$$Q = \omega\tau = \frac{\omega}{\Delta\omega}. \tag{4.25}$$

In the above equation, ω is the resonance frequency and the last expression was already introduced above with $\Delta\omega$ as linewidth of the resonance. There are several loss contributions, that ultimately define the photon lifetime in

the resonator:

$$Q^{-1} = Q_{mat}^{-1} + Q_{surf}^{-1} + Q_{coupler}^{-1} + Q_{rad}^{-1}, \tag{4.26}$$

where Q_{mat}^{-1} is determined by intrinsic absorption and scattering of the resonator material. Bulk material absorption typically emerges from residual impurities and charge carriers [148]. Material scattering can happen when nanocrystallites are present, as discussed for TiO_2 [149, 150, 151]. For high quality crystals, the material scattering should be negligible. With α_{mat} as the material loss coefficient, it is only the distance traveled in the material, which governs the material loss rate

$$\gamma = \frac{c}{n_{eff}} \alpha_{mat} = \frac{\omega}{Q_{mat}}, \tag{4.27}$$

where n_{eff} is the effective refractive index. Estimating the material Q-factor can then be done with

$$Q_{mat} = \frac{2\pi n_{eff}}{\lambda \alpha_{mat}}. \tag{4.28}$$

Q_{surf}^{-1} is determined by surface absorption and scattering of the WGMR. Surface absorption can originate from adsorbed water for example. Typically the most impactful and limiting factor, however, is the surface scattering. For integrated microrings and microdisks, residual surface inhomogeneities, which originate from the fabrication process with a root mean square size σ (for $\sigma \ll \lambda$), determine the surface scattering-limited Q-factor [152, 153]:

$$Q_{surf} = \frac{3\lambda^2 m^{10/3}}{16\pi^5 \sigma^2 n_{eff}^2 l^{5/2}}. \tag{4.29}$$

A brief example for the radial mode number $l = 1$ (corresponding to a fundamental WGM), $\lambda = 1\mu m$, $n_{eff} = 2.2$ and a surface roughness of $\sigma = 50nm$

puts two different resonator sizes in perspective:

$$Q_{\text{surf}} \quad \approx 1 \times 10^5, \quad \text{for } m = 80 \, (R \approx 7\mu\text{m}), \tag{4.30}$$

$$\approx 2 \times 10^8, \quad \text{for } m = 800 \, (R \approx 70\mu\text{m}). \tag{4.31}$$

It becomes apparent, that the surface roughness has a larger impact the smaller the radius of a WGMR. Optimized fabrication procedures, however, can overcome these limits.

Q_{coupler} is determined by the loss due to coupling to an external mode, such as a waveguide mode. Modes of integrated WGMRs are typically accessed by an integrated waveguide located at a certain distance from the resonator. Depending on the distance, a resonator can be loaded by the waveguide in different regimes. The overcoupled regime can be found, when the waveguide is located too close to the resonator. In this situation, the external loss induced by the nearby waveguide is larger than all other contributions to loss. The critically coupled regime is achieved when coupling loss and all other loss are exactly equal. In order to obtain highest quality factor values, it is expedient to work in the undercoupled regime, which is defined by the coupling loss being smaller than other contributions, hence not limiting the quality factor.

Other commonly used measures for optical resonators are subsequently given for the class of WGMRs. The spectral distance between two resonances is called free spectral range (FSR) and is defined as

$$\Delta\nu_{\text{FSR}} = \nu_{\text{m}+1} - \nu_{\text{m}} \approx \frac{c}{2\pi R n}. \tag{4.32}$$

The FSR is linked to the linewidth of a resonance $\Delta\omega$ by the definition of finesse $\mathcal{F}$:

$$\mathcal{F} = \frac{2\pi\Delta\nu_{\text{FSR}}}{\Delta\omega} = \frac{\Delta\omega_{\text{FSR}}}{\Delta\omega}. \tag{4.33}$$

4.2.3 Device Design of Whispering Gallery Mode Resonators

Prior to delving into experimental details about fabrication of devices, this section discusses structural and device design choices, targeted at reaching significant cavity-emitter coupling, which allows for measurements of an enhancement of the spontaneous emission rate. Here, maximizing the ratio of quality factor to mode volume, the Q/V-ratio, is an apparent goal derived from equation 4.13. Equally important, however, is the fundamental principle of scalability in the fabrication process for our design choice, which will be illuminated in the following.

Integrated optical resonators come in various shapes and sizes, such as Fabry-Pérot cavities, Bullseye cavities [154], WGMRs, and photonic crystal cavities. A commendable overview of various resonator geometries is given by [155]. Fabry-Pérot-like cavities are widely used in material systems, that allow for epitaxial growth of 2D layers, such as semiconductor heterostructures. In these approaches, planar distributed Bragg reflectors made out of GaAs and AlAs for example, are alternatingly stacked into a Fabry-Pérot-like cavity and then shaped by reactive ion etching into micropillars[156]. This way, highly efficient single-photon devices based on self-assembled quantum dots and strong coupling in the microcavity-quantum dot system was realized [157, 158]. The vertical emission characteristic of micropillars, however, does not comply well with scalability concerns. But more importantly, adequate epitaxial growth capabilities of rare-earth host crystals acts as bottleneck to the micropillar approach in the rare-earth domain.

Especially small mode volumes can be obtained with the photonic crystal cavity design, which was orginially realized in semiconductors like InGaAsP [159, 160]. This design has a particularly small footprint and finds widespread application across various materials used in quantum information science,

such as diamond [161, 162] and silicon carbide [163, 164, 165]. The fabrication of these cavities is challenging based on their small dimensions and susceptibility to fabrication imperfections [164]. The two rare-earth related approaches, which realized photonic crystal cavities can be divided into a non-scalable design, which is based on focused ion beam milling of YVO_4[17, 19, 20]. And the second approach makes use of photonic crystal cavities made out of silicon, which are then transferred onto YSO [18].

The last class of photonic resonators introduced in these considerations are on-chip microring resonators or integrated WGMRs. Their application ranges from the field of modern-day telecommunication networks, where reconfigurable optical add-drop multiplexer based on microring resonators are targeted at dense wavelength division multiplexing [166, 167, 168, 169, 170, 69, 171] to a multitude of emerging applications and fundamental studies. Noteworthy topics are their use as integrated optical parametric oscillators for frequency comb generation [172, 173, 174, 175], capabilities of ultra-high quality factors of up to $Q = 10^8$ [176], Raman lasing [177], biosensing [178], and single-photon level frequency conversion [179]. Also, WGMRs have already been succesfully applied in studies in the field of cavity quantum electrodynamics [180, 181]. A distinct advantage of integrated WGMRs over photonic crystal cavities are their somewhat relaxed fabrication requirements due to their inherently larger dimensions when compared to photonic crystal cavities. This reason ultimately determined the design choice to work with WGMRs, as rapid fabrication procedures were found key in the assessment of different photonic platforms, which are discussed throughout this chapter.

Further, we will consider different emitter locations relative to the resonator. The most common approach is an emitter placement in the material, which is fabricated into an optical resonator [182, 180, 183, 19]. Under certain circumstances however, the emitters are located outside the shaped material. Typical reasons for this choice are, for example, when the active substrate, which hosts the emitter, cannot be shaped into resonators out of practical reasons. This is the case for hard and inert materials, such as sapphire, YAG,

or YSO, which can barely be shaped based on reactive ion etching, but are excellent host materials for quantum emitters. A prominent example for this approach is reference [18], where etched silicon resonators were transferred onto a YSO substrate for CQED experiments on single rare-earth ions. Also, a high-Q WGMR out of Si_3N_4 was used to study rare-earth ions located in an active SiO_2 substrate [181]. These approaches rely on evanescent coupling between the cavity mode and the emitter. This is clarified by observing the position-dependent electric field intensity of the cavity mode, which defines the obtainable Purcell enhancement. Following equation 4.14, $|\mathbf{E}(\mathbf{r})|$ as the electric field of the cavity mode at position $\mathbf{r}$ can be used to estimate ξ^2, the normalized dipole orientation factor. Hence, the key measure is the variation of the electric field intensity $|\mathbf{E}|^2$ over the cross-section of the resonator mode.

Using FEM-based COMSOL software, the variation of the electric field intensity of a fundamental resonator mode in the emitter-containing substrate can be simulated. In this example, a WGMR consisting of a material stack $SiO_2/LiNbO_3/SiO_2$ with refractive indices of $n_{SiO_2} = 1.45$, and $n_{LiNbO_3} = 2.2$ was investigated, shown in figure 4.2. Here, $LiNbO_3$ is the waveguiding material and SiO_2 the rare-earth host, with emitters coupling evanescently to the WGMR. Fitted with an exponential decay, we can observe the relative electric field intensity $|\mathbf{E}|^2/|\mathbf{E}_{max}|^2$ in the SiO_2 substrate to drop rapidly depending on the depth. During emitter engineering by means of implantation doping, it is therefore expedient to create them close to the interface between waveguide material ($LiNbO_3$ in this example) and substrate material (SiO_2), which is possible with low energy ion implantation.

Further optimization of the device design with respect to the Purcell enhancement is concerned with reducing the mode volume of the WGMR to an ideal minimum. As we decrease the size of a WGMR, radiative losses increase, following from simulations shown in figure 4.3. As a rule of thumb given by [184], these radiation losses on the curved surface are negligible, if the circumference of the resonator exceeds several tens of wavelengths. At
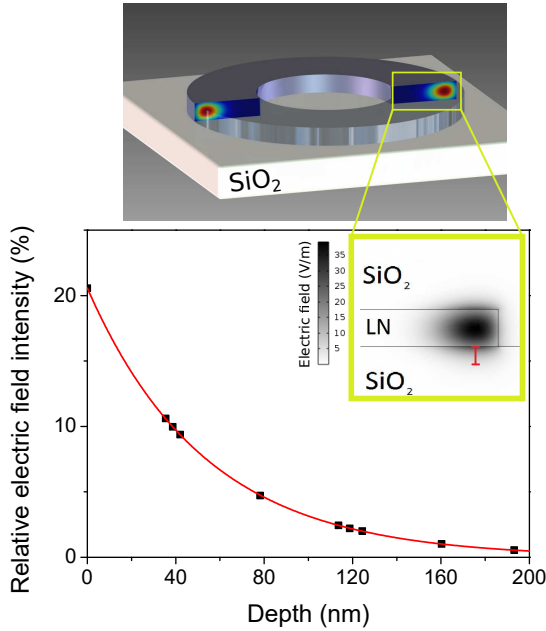
FIGURE 4.2: Relative electric field intensity of the cavity mode $|\mathbf{E}|^2/|\mathbf{E}_{\max}|^2$ dependent on the depth in the SiO_2 substrate, indicated by the red scale in the inset. Inset: Electric field amplitude of a fundamental mode of a simulated WGMR.

what resonator dimensions exactly we can dismiss radiative losses shall be investigated henceforth. In this example, a WGMR consisting of a material stack YAG/TiO_2/air with refractive indices of $n_{YAG} = 1.8$, $n_{TiO_2} = 2.2$, and $n_{air} = 1.0$ was investigated. Through FEM simulations, complex wave numbers k of WGMRs of different dimensions were obtained. They were studied for three particular wavelengths, namely 489nm, 800nm, and 1500nm, as shown in figure 4.3. As the microring radius is increased linearly, the radiative quality factor is rising exponentially. In order to not be limited by radiative losses, optimal resonator sizes can then be predetermined accordingly.
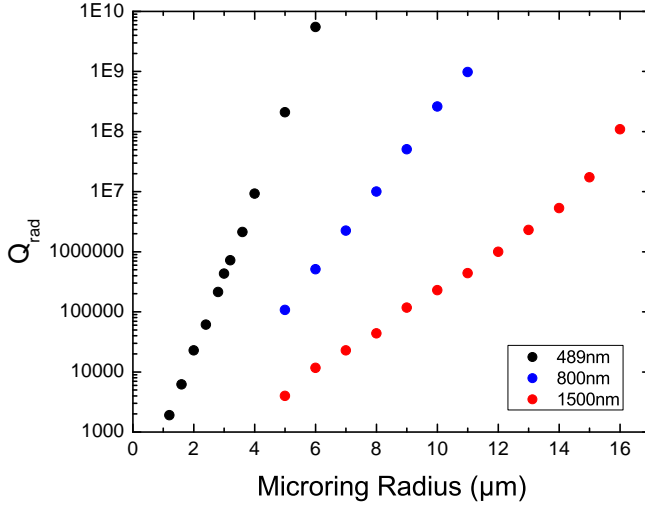
FIGURE 4.3: Radiative quality factor obtained from FEM-simulations of WGMRs on a material stack YAG/TiO$_2$/air with refractive indices of n_{YAG} = 1.8, n_{TiO_2} = 2.2, and n_{air} = 1.0. Q_{rad} is plotted as a function of WGMR radius for three different wavelengths, 489nm, 800nm, and 1500nm.

4.3 Amorphous Silicon-Doped Titania Film Platform

The creation of integrated nanoscale and microscale photonic structures in a certain material directed at CQED experiments with rare-earth ions is a multilayered question. Typical trade-offs include scalability, ease of fabrication, rare-earth ion properties, projected ion-cavity coupling, and tunability. As optical transitions of rare-earths are oftentimes found at visible wavelengths, only materials with a large enough transparency window were considered in the choice of material. The following material systems, amongst others, have already been proposed and investigated as photonic platforms in the visible

spectral region: AlN [185], diamond [186, 187, 177, 188], SiN [189, 190], and TiO$_2$ [151, 191, 192, 193, 150, 194]. Also studied was SiO$_2$ [195, 196], however, its refractive index is too low to support waveguiding on a vast number of materials. Due to the fact, that diamond with high optical quality is not available for deposition in a conventional manner, it is also ruled out as a solution. All other mentioned material systems above are viable solutions. The waveguiding platform based on amorphous silicon-doped titania films is particular suited based on the fruitful collaboration with our colleagues from 3D-OXIDES and their chemical beam vapor deposition technique. The idea of the 'amorphous silicon-doped titania films'-project is to access rare-earth ions located in host crystals, which are hardly compatible with integrated photonics, such as YAG or YSO. For that, it is required to deposit high quality films of a material with higher refractive index than the substrate material. With a refractive index of $n_{\text{YAG,YSO}} \approx 1.8$ for YAG and YSO, a deposited dielectric with $n > 2$ is sufficient. This film (when shaped into cavities) can then facilitate resonator interaction with emitters embedded in the substrate host crystal based on evanescent coupling. This approach has shown the advantage of preserving the spectroscopic properties of emitters [110]. In the following, thin film deposition on various substrates, its structuring into photonic elements, optical characterisation and also rare-earth doping of photonic elements made out of Si:TiO$_2$ films is discussed.

4.3.1   Combinatorial Si:TiO$_2$ Films

In the following, favorable properties of titanium dioxide for use as photonic platform in rare-earth based CQED experiments are listed. TiO$_2$ crystallizes in three different polymorphs: rutile, anatase and brookite. Rutile, known as the most stable phase, has a bandgap of 3.0eV, and anatase has a bandgap of 3.2eV[149]. Little is known about brookite. The large bandgap provides a large transparency window from UV to near infrared, matching well with optical transitions of many rare-earth ions. The high refractive index of TiO$_2$ between 2.3 and 2.4 as thin film provides compatibility to various rare-earth

host materials when the evanescent coupling approach is considered (discussed in section 4.2.3). Additionally, TiO_2 can be deposited as thin films with various methods, such as atomic layer deposition [193], RF magnetron sputtering [150], laser molecular beam epitaxy [197], reactive DC sputtering [191], and ion beam sputtering [198].

However, deposited titanium dioxide films tend to form nanocrystallites with grain sizes of 30-40nm[149], which can cause scattering loss [150, 151] and significantly reduce the achievable quality factor of fabricated WGMRs. The nanocrystallization during growth of TiO_2 thin films prompted the study of amorphous versions, which alleviate this problem [151, 191, 192, 193, 150, 194]. An alternative way to prevent nanocrystallite formation of deposited TiO_2 thin films is the co-doping with silicon [199]. The $Si:TiO_2$ thin film creation throughout this work was performed with the chemical beam vapor deposition technique. It was already reported on the amorphization of TiO_2 with additional Si doping based on this technique [200]. In accordance with other studies, the silicon doping leads to a slight decrease in the refractive index of the film [201]. We will find, that the refractive index of created films is high enough to conveniently support waveguiding on high-index optical crystals, like YAG and sapphire.

A detailed description of the deposition process of combinatorial $Si:TiO_2$ thin films can be found in [200] and deposition procedures conducted for samples discussed in this work can be found in appendix A.4. The films were investigated in a TEM (Tecnai Osiris microscope) as cross-sectional images, where thickness and growth morphology information were obtained. The total thickness variation for films deposited on 4" glass wafers was found to be $\pm 2\%$. Typical TEM images of a sample film on glass substrate are shown in figure 4.4. The high-angle annular dark-field image (figure 4.4 a) shows a homogeneous film. In the inset, the selected area electron diffraction pattern as well as the high resolution TEM image (figure 4.4 b) and the corresponding FFT confirm the amorphous phase of the film and show no sign of crystal structure.
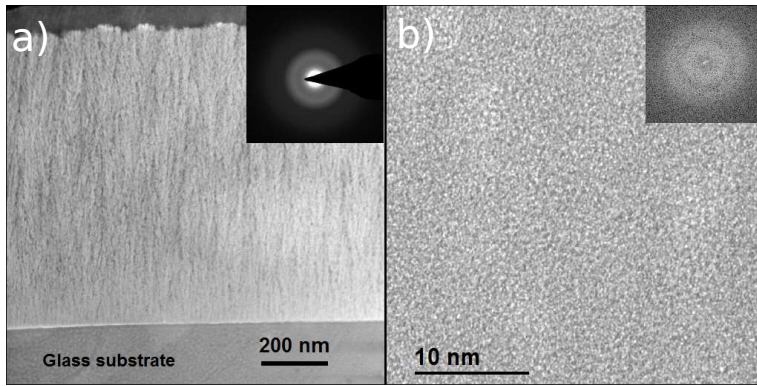
FIGURE 4.4: Cross-sectional view by TEM of a Si:TiO$_2$ deposited on a glass substrate. a) High-angle annular dark-field imaging scanning transmission electron microscope image. Inset: selected area electron diffraction pattern. b) High resolution TEM image. Inset: FFT.
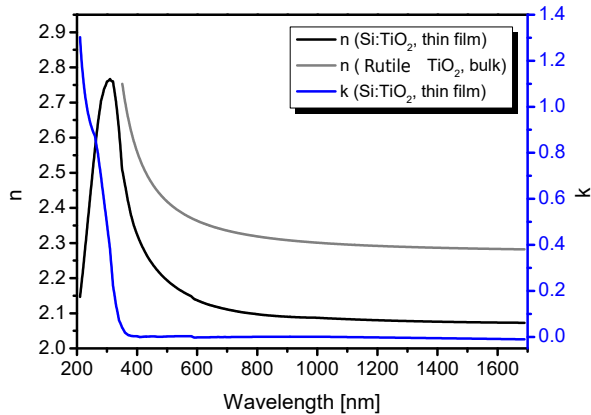

FIGURE 4.5: Refractive index for an unpatterned Si:TiO$_2$ film on silica sample and for comparison the refractive index of bulk rutile TiO$_2$[202]. *n* and *k* denote the refractive index and the extinction coefficient, respectively

Ellipsometry measurements (taken on a variable angle spectroscopic ellipsometer from J. A. Woollam Co.) on an unpatterned Si:TiO$_2$ film are shown

in figure 4.5. The measured film had a thickness of 535nm and measured dispersion shows the refractive index to range between 2.3 and 2.1 within the transparency window starting at 400nm wavelength and extending all the way to the infrared. As expected, the absorption losses quantified by the extinction coefficient *k* are insignificant.

4.3.2 Structuring of Si:TiO$_2$ Films

In order to assess the optical quality of the film, photonic structures such as waveguides and monolithic WGMRs were fabricated and tested. The generic fabrication process based on a lift-off procedure is depicted in a sequence diagram in the appendix in figure A.3 and was used in an adapted manner for various thin film stacks throughout this chapter. It starts with an electron-beam lithography patterning step performed on a double-layered positive tone PMMA electron beam resist. Here, the bottom layer (200K) has a shorter polymer chain length than the top layer (950K), which causes an undercut of the resist mask when exposed by the electron beam. This behavior is caused by differing exposure sensitivities between the two layers and aims for a metal mask lift-off step with a minimum of roughness at edges. After patterning, a nickel mask with a thickness of 50nm was deposited and the subsequent lift-off step was performed. Next, a RIE step in an Ar/CF$_4$/O$_2$ atmosphere with respective flow rates of 4/16/3sccm and an RF power of 100W (PlasmaPro 80 RIE, Oxford Instruments) was used to etch out the metal mask pattern into Si:TiO$_2$ film [203]. During the etch process, the bias voltage was 387V and the process pressure was 15mTorr. Total dry etch process time was 24min and 535nm Si:TiO$_2$ was etched during this duration. After the dry etch process, the remaining nickel mask was removed by wet etching nickel in an aqueous 1M solution of nitric acid. The fact, that nickel remained present after the etch process, indicates an etch selectivity of at least 1:11.

The last process step was an annealing treatment in air atmosphere of the structured Si:TiO$_2$ films, in order to restore surface termination, as fluorine
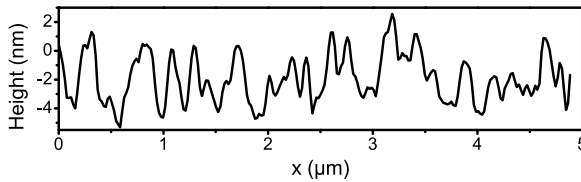
FIGURE 4.6: Surface height profile of deposited film after annealing measured with AFM. Film surface roughness is approximately 3 nm.

terminated surfaces originating from fluorine based reactive ion etching showed increased optical absorption. During annealing tests with temperatures up to 650°C , the films showed no sign of formation of nanocrystallites. The inherent thermal instability of amorphous TiO_2 films [204] is therefore resolved to some extent for Si:TiO_2 films under investigation. For annealing temperatures above 800°C however, the film changed visually, suggesting recrystallization. The final annealing step performed on structured films had a temperature of 500°C and a duration of 4h. After the annealing, AFM measurements on the film showed a roughness of approximately 3nm, which is identical to the unannealed film. The corresponding measurement is shown in figure 4.6. Also, no change in refractive index was seen upon annealing.

A resulting structure from the described procedure is shown in figure 4.7. The image was taken with an SEM and displays a WGM microdisk resonator with radius of 5μm and an evanescently coupled waveguide with length of 30μm. The ends of the waveguide are attached to a 100μm^2 pad with incoupling holes to inject light into the waveguide. The gap between waveguide and WGMR is around 400nm.

4.3.3   Si:TiO_2 Thin Film on Quartz

Throughout this study, fabricated photonic structures such as waveguides and monolithic WGMRs are characterised in a home-built bifocal microscope setup. A schematic diagram of the characterisation setup is shown in figure
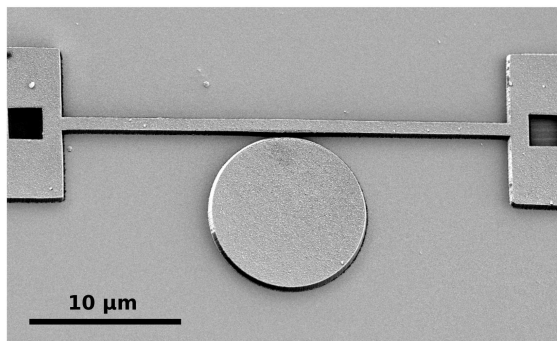
FIGURE 4.7: SEM image of a Si:TiO$_2$ WGMR evanescently coupled to a straight optical waveguide.
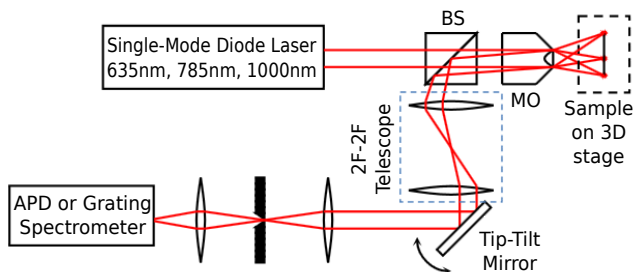
FIGURE 4.8: Schematic of the confocal microscope used as characterisation setup. The sample is mounted on a 3D nanopositioner and can be moved through the laser focus. Light emission is collected with the same objective lens, which is used to focus the light onto the sample. Collected light is sent through a 2F-2F telescope and a tip-tilt mirror onto the pinhole selecting the observation point on the sample. Single photon counting avalanche photodiode (APD) and grating spectrometer equipped with cooled CCD camera can be used as detectors. MO: Microscope Objective.

4.8. An important difference between the confocal microscope setup shown in figure 2.6 is the detection path, which is equipped with a 2F-2F telescope. This gives the additional ability to scan the point of detection in the vicinity of the laser focus position [205]. A high numerical aperture (NA) objective lens (Olympus 0.95×50) was used to focus the laser onto the sample, which results in a tight focusing with a spot size of $\lambda/(2NA) = 0.53\lambda$.

The characterisation of samples is mainly focused on the spectral width of resonances of microring and microdisk resonators coupled to a nearby waveguide. These characterisations are achieved with several tunable single frequency diode lasers, which could be coarsely tuned over wide ranges and mode-hop-free for smaller fine-tuning ranges. The following home-built diode lasers in Littrow configuration were used:

1. Laser 1: Coarse Range: 770-810nm, mode-hop-free fine-tuning range: 30GHz

2. Laser 2: Coarse Range: 970-1070nm, mode-hop-free fine-tuning range: 130GHz

All lasers mentioned above had a spectral linewidth below 1 MHz.

During characterisation, the laser output is incoupled into the waveguide by focusing the light onto the end of a waveguide. The residual light scattering at the waveguide end results in light injection into the waveguide. No further optimizations with respect to coupling efficiency were undertaken, as the amount of light propagating in the waveguide was found sufficient for characterisation purpose. As shown in figure 4.9 a), once the finely tuned laser matches the resonance frequency of the WGM, the rim lights up. This is residual scattering on film imperfections of the structures and can be captured by CCD camera or the confocal microscope setup as signal.

Figure 4.9 b) shows the resonator model and a fundamental mode of the particular structure shown in figure 4.9 a), a ring resonator with outer radius of $R = 8\mu$m, a thickness of 535nm and a rim width of 2μm. The Si:TiO$_2$
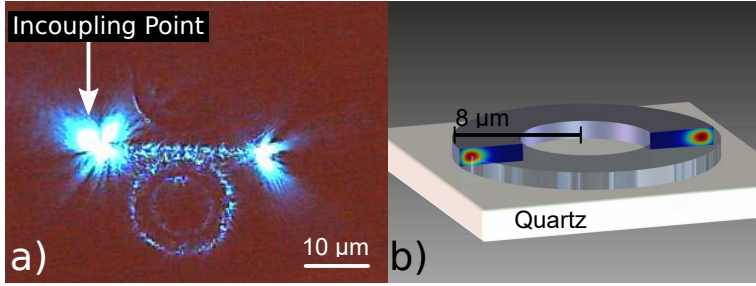
FIGURE 4.9: a) Camera image of a structure excited on resonance. The left end of the waveguide was used as input. The cavity mode is visualized by the residual scattering of the laser, in resonance of the WGM. Tunable blue diode laser was used for visualization. b) Resonator model with simulated electric field profile of the fundamental mode at 790nm.

thin films are on top of a quartz substrate with a refractive index of quartz at 790nm of $n_{\text{quartz}} = 1.45$. Based on refractive index measurements (see figure 4.5), fundamental modes of this geometry can be obtained with FEM-simulation. Furthermore, the free spectral range of $\Delta\lambda_{\text{FSR}} = 5.60$nm can be extraced from simulations.

Next, the scattering signal on the rim of the resonator was detected as a function of the laser frequency, in order to obtain the linewidth of WGM resonances. Figure 4.10 a) shows the result of the spectral measurement of one such mode of the structure shown in figure 4.9. From fitting with the Fano model [206], we can extract the linewdith of $\Delta\nu_{\text{788nm}} = 2.6$GHz for a mode at 788nm, which corresponds to the narrowest line we found on fabricated resonators. As expected, the gap between resonator and waveguide was sufficiently large, such that the system was in the undercoupled regime and the quality factor was not affected by waveguide damping. This qualitative assessment is done by comparing the amount of light, that couples from the waveguide into the resonator for structures with different gap sizes. The spectral width of 2.6GHz corresponds to a quality factor of $Q = 146000$. In
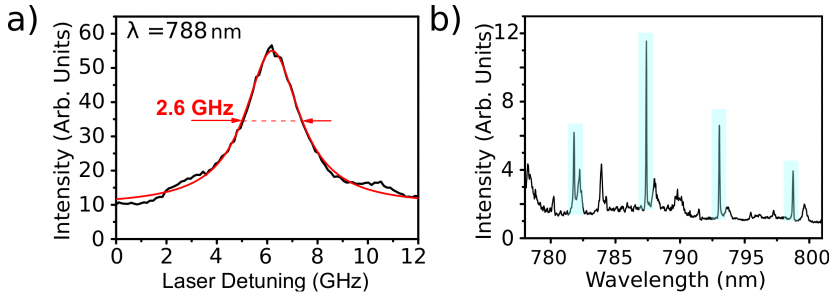
FIGURE 4.10: a) The spectral shape of the cavity mode at 787.98nm. It was obtained by sweeping a single-mode laser through the cavity resonance. b) Typical mode spectrum of the studied resonator geometry between 780nm and 800nm obtained with a broadband light source. Mode width measurement is limited by the resolution of the spectrometer for fundamental modes, which are highlighted in blue.

order to confirm the FSR value, a mode spectrum of the resonator geometry was obtained by coupling a broadband light source into the waveguide and detecting signal on the resonator rim with a high resolution spectrometer. Figure 4.10 b) shows the broadband measurement and confirms the simulation result. Based on the FSR value around 790nm, we can estimate the effective index of this particular mode with

$$n_{\text{eff}} \approx \frac{\lambda^2}{2\pi R \Delta\lambda_{\text{FSR}}} = 2.18. \tag{4.34}$$

This allows us to give an estimate on the overall propagation losses $\alpha = 5.1\text{db/cm}$ around 790nm based on the measured quality factor (from equation 4.28) with $\alpha = 2\pi n_{\text{eff}}/Q\lambda$. In table 4.1, different waveguiding structures based on TiO$_2$ thin films are compared regarding their propagation loss. In a trade-off for the silicon doping-dependent decrease of refractive index, the Si:TiO$_2$ film shows benchmark propagation loss at 800nm. Figure 4.11 a) shows an SEM image of the best performing WGMR-waveguide system. Low sidewall roughness of structures made from the amorphous Si:TiO$_2$

film can be qualitatively seen in a close up of the waveguide-resonator gap, shown in figure 4.11 b).

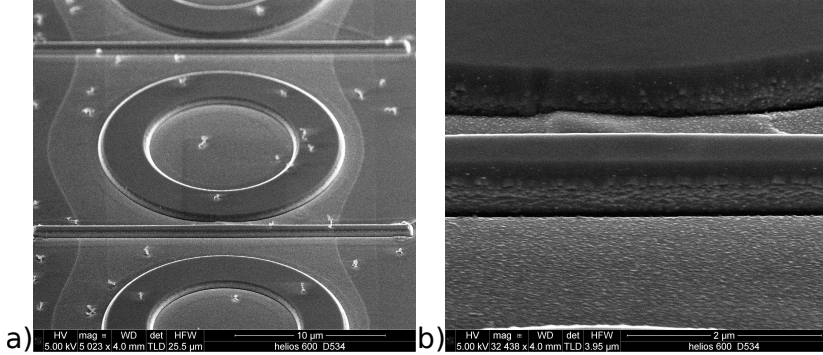FIGURE 4.11: a) SEM image of WGMR with a measured linewdith of $\Delta\nu_{788nm} = 2.6$GHz. White particles are post-process contamination of unknown origin and were not identified to cause additional scattering. b) SEM image of gap between waveguide and cavity. Sidewall roughness can be qualitatively seen.

Deposition method	loss at 800nm	loss at 1550nm	Reference
RF magnetron sputtering	9	4	[150]
laser molecular beam epitaxy	57	-	[197]
atomic layer deposition	-	2.4	[193]
reactive DC sputtering	5.6	1.2	[191]
ion beam sputtering	-	5.4	[198]
chemical beam vapor deposition	5.1	-	this work

TABLE 4.1: Comparison of propagation loss in dB/cm for TiO_2-based thin film waveguiding structures. A categorization for different deposition techniques for thin films is given.

Additionally, a characterisation of structures at wavelengths around 1000nm was performed. Figure 4.12 a) shows the measurement of a resonance at 1013.3nm with a linewidth of $\Delta \nu_{1013.3nm} = 5.9$GHz for the cavity-waveguide system with the largest available gap size. This corresponds to a quality factor of $Q_{1013.3nm} = 50000$. Compared to the result at 800nm, the resonators show deteriorated quality factor. This suggests waveguide damping for fabricated structures for measurements around 1000nm, based on small gap size. Alternatively, the decreased quality factor can be caused by small resonator geometries, which can amplify surface scattering loss based on equation 4.29, where the $\propto m^{10/3}$-dependence ($\propto R^{(10/3)}$) beats the $\propto \lambda^2$-dependence. It must be mentioned, that equation 4.29 does not consider axial confinement, which is present in integrated WGMRs, but rather completely spherically shaped resonators. This conjecture has to be taken with a grain of salt, as no systematic assessment of this effect was undertaken. The reasoning of increased scattering loss at 1000nm for the fixed WGMR geometry is further supported by the scattered light intensity, shown in figure 4.12 b). Here, no waveguide scattering is visible and only the rim of the resonator lights up in the camera image. When compared to figure 4.9 a) for blue light, uniform scattering was seen.
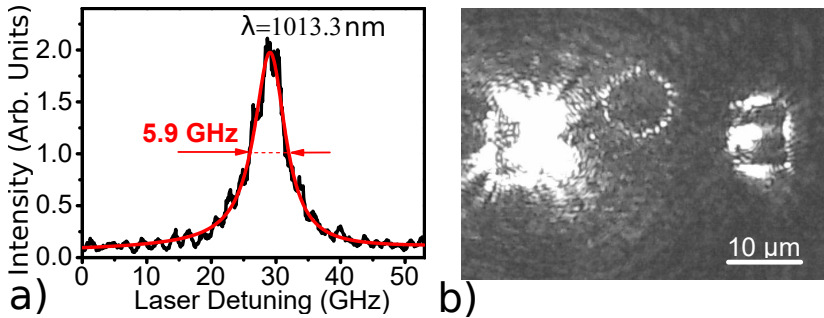
FIGURE 4.12: a) The spectral shape of the cavity mode at 1013.3nm. It was obtained by sweeping a single-mode laser through the cavity resonance. b) Camera image of 1013nm light incoupled into the waveguide and on resonance with the cavity. Geometry of the photonic structure is the same as shown in figure 4.7. Note that no light scattering on the waveguide is visible for this wavelength, however, the WGMR is lighting up brightly, because the laser is in resonance with a cavity mode and light is scattered on the resonator rim.

4.3.4 Si:TiO$_2$ Thin Film on Sapphire and YAG Substrates
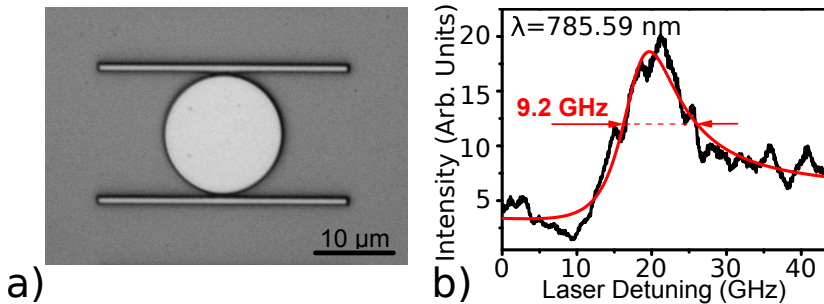

FIGURE 4.13: a) Microscope image of the fabricated add-drop filter out of Si:TiO$_2$ thin film on sapphire. Resonator radius is 7μm. b) Spectral shape of a cavity mode at 785nm of the add-drop filter structure shown in a).

Directed at the realization of a scalable photonic platform for CQED experiments with rare-earth ions, Si:TiO$_2$ thin film was deposited on sapphire and YAG substrates. Especially YAG is a well-studied host crystal with respect to single rare-earth ions [36, 37, 43]. Their respective refractive indices around 800nm are $n_{\text{sapphire}} = 1.76$ and $n_{\text{YAG}} = 1.82$. This is sufficiently low to maintain waveguiding in low mode-volume WGMRs out of the thin film. Measurements of structures fabricated on top of bulk sapphire are shown in figure 4.13 and confirm waveguiding. Figure 4.13 a) shows a microscope image of the fabricated add-drop filter geometry, which exhibits two waveguides, one to 'add' or inject light and one to 'drop' or detect it. This provides the option to conveniently measure cavity resonances on the output of the dropping port when sending light through the adding waveguide. Resonance linewidth measurements are shown in figure 4.13 b). From the Fano fit, we can extract a spectral width of $\Delta\nu_{785\text{nm}} = 9.2\text{GHz}$, which corresponds to a quality factor of $Q_{\text{sapphire}} = 41500$.
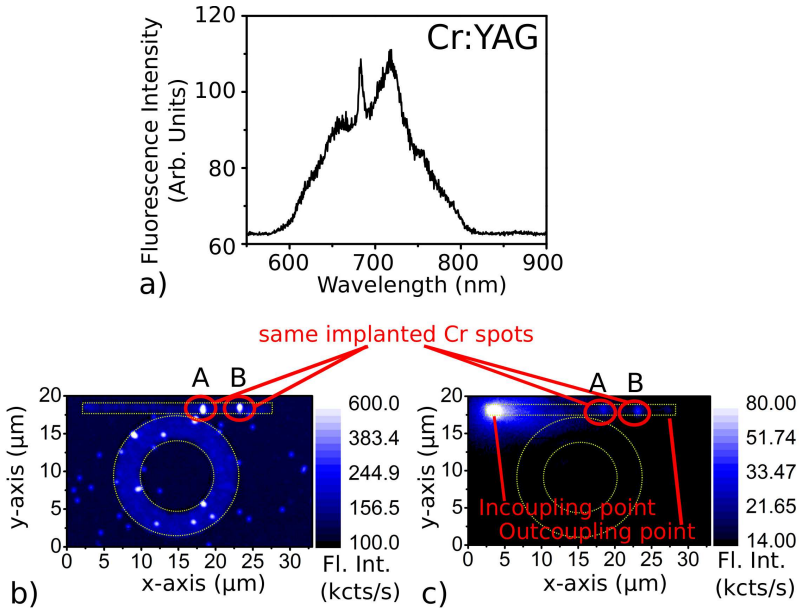
FIGURE 4.14: a) Spectrum of fluorescence signal of implanted Cr spots in a YAG crystal. b) Laser scanning confocal microscope image. Excitation and detection point were coinciding. Bright spots correspond to fluorescence of implanted Cr spots in YAG. Indicated in red and labelled A and B are two spots underneath a waveguide structure. Yellow dashed line indicates the geometry of the photonic structure, which is the same as shown in figure 4.11. c) Tip-tilt mirror scan of the same structure as shown in image b). Laser was injected into the waveguide on the left end (located at 3μm on the horizontal axis and labelled "Incoupling point") and shows a strong signal. Indicated in red are the two same spots A and B, showing fluorescence signal while being evanescently excited by the laser in the waveguide mode.

Waveguiding tests for Si:TiO$_2$ films on YAG crystals were combined with experiments on evanescent coupling of emitters located in the YAG matrix. For demonstration of evanescent coupling between waveguide and emitter, light is injected into the waveguide and light from evanescently excited emitters

is collected by the microscope. To this end, the YAG crystal was implantation doped with chromium ions through a perforated copper mask with an average hole diameter of $\approx$400nm. The fabrication procedure of perforated copper masks is described in [21]. Cr ion implantation energy was 100keV and the fluence was 10^{13}cm^{-2}. As a result, Cr ions ended up in the YAG crystal in a depth of $\approx$55nm with a depth-straggle of 22nm[122]. The YAG crystal was annealed at 1200°C to heal out implantation damage and stabilize implanted Cr ions in the YAG matrix. Subsequently, a Si:TiO$_2$ film was deposited and shaped into waveguides and resonators. As a transition metal and not a rare-earth, Cr regardlessly serves the purpose of being an emitter when doped into YAG crystals, as demonstrated in figure 4.14 a), where a spectrum of the fluorescence signal of an implanted Cr spot is shown. Figure 4.14 b) shows a laser scanning confocal microscope image of the Cr doped sample with photonic structures on top. For the scan, excitation and observation point were coinciding. Bright spots represent fluorescence of implanted spots. As indicated with red, two Cr spots are located underneath a fabricated Si:TiO$_2$ waveguide. The laser scanning microscope images were taken with a laser excitation source for Cr ions at 600nm (tunable Rhodamine 6G dye laser, Coherent 599) and a 640nm long-pass optical filter was used to reject laser light spectrally.

By injecting laser light into the waveguide and scanning the tip-tilt mirror (scanning the point of detection while laser position is fixed), we obtain figure 4.14 c). Here, the bright spot located at around 3μm on the horizontal axis corresponds to the incoupling point. Due to low coupling efficiency into the waveguid mode and the existant residual Cr impurities in YAG, strong fluorescence is detected on the input end of the waveguide. Based on simulations shown in figure 4.2, one would expect laser light propagating in the waveguide to evanescently excite Cr spots underneath with roughly 7% efficiency, based on the implantation depth. As pointed out in red in figure 4.14 c), the two spots singled-out in figure 4.14 b) show fluorescence in the tip-tilt mirror scan, located at around 18μm and 23μm on the horizontal axis. Cr

emission can also be detected at the output of the waveguide. Since the laser was not in resonance with the cavity, no signal from the resonator is seen in the tip-tilt mirror scan. This experiment confirms the evanescent coupling of light between emitters and waveguide.
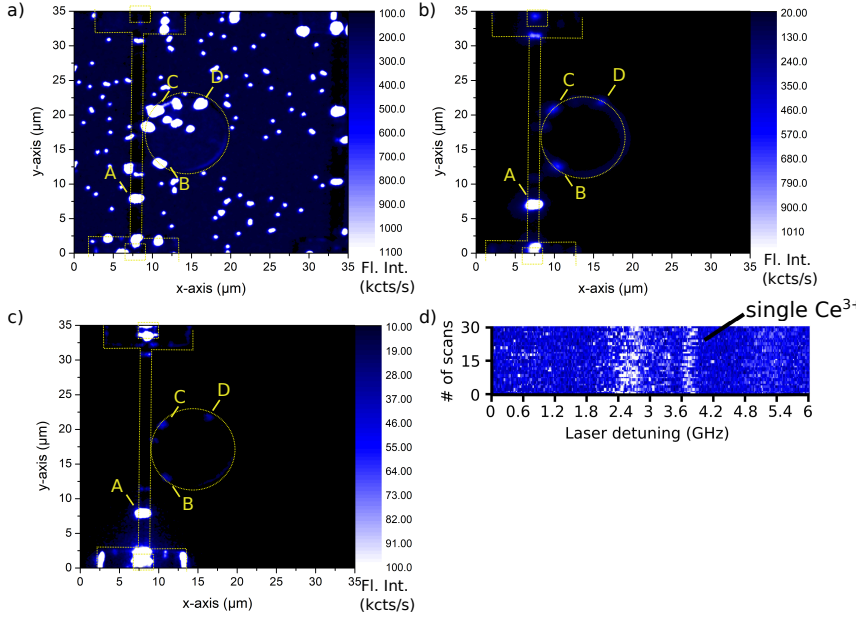
FIGURE 4.15: a) Laser scanning confocal microscope image. Excitation and detection point were coinciding. Bright spots correspond to fluorescence of implanted Ce spots in YAG. Indicated in yellow are four spots (A, B , C, D) underneath the waveguide and resonator structure. Indicated with yellow dashed lines is the geometry of the photonic structure, which is the same as shown in figure 4.7. b) Tip-tilt mirror scan with stationary laser position of the same structure as shown in image b). Laser is injected into the waveguide on the bottom end and is in resonance with the cavity. Indicated in yellow are the four same spots showing fluorescence signal while being evanescently excited by the laser in the waveguide and resonator mode. c) Laser scanning dynamic tip-tilt mirror scan. While excitation point was scanning, the tip-tilt mirror was moved relative to the laser position, such that the output end of the waveguide at $(x, y) = (7, 3)\mu$m was detected stationarily. d) 30 successive photoluminescence excitation sweeps of Spot A with a single mode laser at 4K temperature.

In order to confirm unperturbed emitter properties after conducting the entire sequence of fabrication procedures, which includes implantation doping, annealing, thin film deposition, and structuring, we resonantly studied cerium emitters at cryogenic temperatures in photoluminescence excitation studies in the fashion of [44]. To this end, cerium ions were implanted into a YAG crystal through a perforated copper mask with the same implantation energy as for Cr, mentioned previously, and a fluence of $5 \cdot 10^{11} cm^{-2}$. As a result, Ce ions ended up in the YAG crystal in a depth of $\approx$30nm with a depth-straggle of 10nm[122].

Annealing at 1200°C in a reducing atmosphere stabilized the Ce ions in the trivalent charge state and rendered them photostable under CW excitation, as discussed in [21]. A typical conversion yield of roughly 20% results in approximately 100 fluorescent Ce^{3+} ions per spot. Once waveguide and resonator structures were fabricated, cerium was excited with a diode laser at around 450nm wavelength, tunable via external cavity [37], and laser light is rejected by a 475nm long-pass filter, such that only cerium fluorescence is detected as signal. Also, a 600nm short-pass filter is used to reject parasitic chromium emission emerging from the YAG sample as a uniform background due to high impurity concentrations. A laser scanning confocal microscope image with excitation and detection point coinciding is shown in figure 4.15 a). Bright spots correspond to implated cerium spots, four of them are labelled with A, B, C, and D. The photonic waveguide (dark stripe at $x = 8\mu$m) and cavity are barely visible. In figure 4.15 b), a tip-tilt mirror scan is shown, where the excitation point was stationary at the end of the waveguide, such that light is injected. Since the laser was tuned into resonance with the cavity mode, the WGM is visible, as residual cerium emission is scattered at the resonator rim. Spots underneath the resonator structure are excited by the laser and show fluorescence.

In figure 4.15 c), a laser scanning dynamic tip-tilt mirror scan is shown. Here, the excitation point was scanned, while the tip-tilt mirror position

was moved relative to the laser position. While the excitation point is be-
ing scanned, the entire sample is moved, which shifts also the detection
point. The goal in this experiment was to track the output of the waveg-
uide at $(x, y) = (7, 3)\mu$m. In order to do so, the tip-tilt mirror is moved in
such a way, that the point of detection compensated for the sample move-
ment to stay stationary on the output of the waveguide. For example, when
the laser was located at spot A and exciting cerium ions within, the fraction
of cerium fluorescence, which is coupled into the waveguide mode and cou-
pled out at the end of the waveguide is detected by this measurement. In
this way, 'hotspots' which are coupled to the cavity-waveguide system can
be detected. Spots A, B, C, and D are all detected by this technique. As ex-
pected, the evanescent coupling in the waveguide-emitter system is invari-
ant to the propagation direction (detection of fluorescence at waveguide end
while exciting from top (1) or detection of fluorescence from top while ex-
citing from waveguide end(2)), and thus spatial filtering can be achieved in
various ways. Depending on the amount of fluorescence coupled to the pho-
tonic structures, either approach (1) or (2) promises more signal. In the situa-
tion for cavity enhanced emission, approach (1) is expected to perform better
than approach (2) due to the fact, that cavity-enhanced emission is expected
to be emitted into the resonator mode, which is coupled to the waveguide.

Furthermore, the sample was cooled down to cryogenic temperatures of
around 4K to investigate whether the optical properties of emitters suffer
due to nanofabrication procedures. Ce^{3+} ions hosted in YAG exhibit a ZPL
at 489nm [207] with an inhomogeneous width of 550GHz [44]. A single
mode laser at a wavelength of 489nm is used to resonantly excite cerium
ions. Based on the inhomogeneous width of the ZPL and the reported tran-
sition linewidth of single cerium of about 150MHz, with approximately 100
fluorescent Ce^{3+} ions in an implanted spot, it is possible to detect a single
Ce^{3+} ion under resonant excitation. Measurements of successive photolu-
minescence excitation sweeps on spot A are shown in figure 4.15 d). An
optical transition linewidth of 200Mhz is detected and attributed to a single

implanted cerium ion located within spot A, in good agreement with previous studies [44]. This confirms, that emitter properties do not suffer from the close proximity to the surface and the deposited thin film, as well as the nanofabrication.

4.3.5 Doping of Si:TiO$_2$ Resonators with Erbium
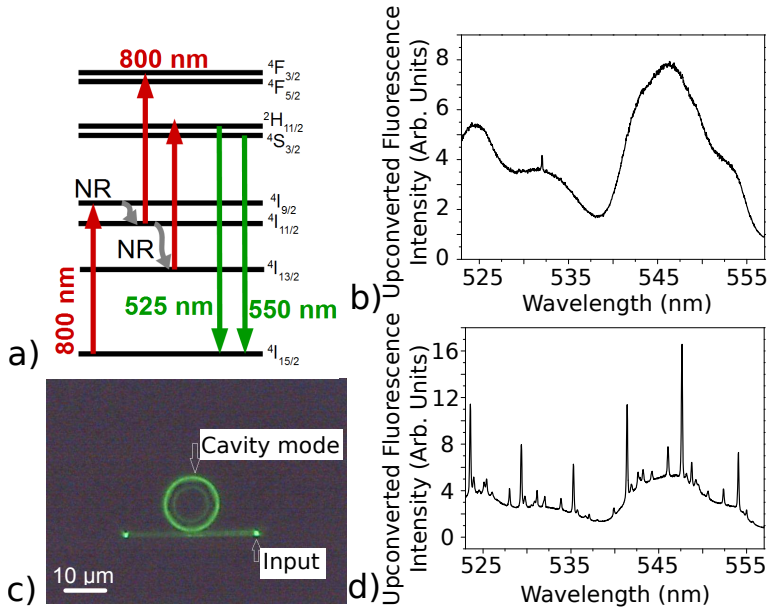
FIGURE 4.16: a) Energy-level diagram for the Er^{3+} ion and its two-step upconversion with 800nm excitation. NR denotes nonradiative relaxation. b) Spectrum of upconverted fluorescence of erbium in Si:TiO$_2$ film. Excitation wavelength is 785nm. c) Cavity mode visualized by upconverted fluorescence. The excitation laser is in resonance with one of the infrared resonator modes. d) Spectrum of upconverted fluorescence of erbium in Si:TiO$_2$ film, collected at the end of the waveguide. The smooth background is due to the fluorescence of the waveguide. Sharp peaks correspond to resonances of the cavity.

This section discusses the implantation doping of erbium into $Si:TiO_2$ thin film. It can be regarded as adding functionality to the thin film, which can be harnessed in applications like on-chip lasers or amplifiers. Alternatively, the creation of rare-earth emitters within a thin film resonator also promises larger coupling to the WGM in the context of CQED experiments, based on the position dependence of the normalized dipole orientation factor ξ^2 (equation 4.14). The robust optical properties of rare-earth ions in most crystalline and glassy transparent media allows for implantation doping with high yield of fluorescent species [21]. Erbium was chosen based on its known upconverted fluorescence in the visible under infrared excitation [208, 209, 210, 211]. The two-step upconversion used to detect green fluorescence from trivalent erbium ions is depcited in figure 4.16 a) and requires a laser to be tuned to the $^4I_{15/2}$-$^4I_{9/2}$ transition of erbium at around $\lambda \approx 800$nm. After this first excitation step, a nonradiative decay into the $^4I_{13/2}$ or $^4I_{11/2}$ level of erbium enables the second excitation step with the same wavelength populating either $^4F_{13/2}$ or $^2H_{11/2}$. From there, green emission originates from transitions between $^4F_{13/2}$ or $^2H_{11/2}$ and the $^4I_{15/2}$ ground state level [208].

Erbium ions were implanted into $Si:TiO_2$ thin film on quartz with an energy of 2MeV and a fluence of 10^{14}ions/cm^2. This leads to a depth of $\approx$ 350 ± 78nm and a maximum local erbium density of $5 \times 10^{18}cm^{-3}$, according to SRIM simulations [122]. Since the erbium depth is close to the center of the structured film, light propagating in the waveguide and resonator can efficiently excite erbium ions. This is particularly important, as the two-photon upconversion processes with metastable intermediate states require higher powers to saturate compared to single step excitations. After erbium ion implantation, the film changed its appearance from pink to gray. We conjecture, that implantation-induced damage caused this change. Also, no Er^{3+} fluorescence was detected right after implantation. Only after postimplantation annealing in air at $500°C$ for 4h, the film resored its original appearance. This behavior is attributed to implantation damage being healed out. Erbium emission was detected after annleaing. The spectrum of upconverted

Er^{3+} emission is shown in figure 4.16 b), in good agreement with previous studies on erbium in glassy environment [212, 213].

In the next step, WGMR structures and a coupled waveguide were fabricated. Based on the fact, that upconversion resonances of Er^{3+} located in glassy environment are spectrally broad ($\approx$ 10nm), several infrared resonator modes can lead to upconverted fluorescence. By tuning the laser into resonance with one such WGM, green erbium emission can be detected on the resonator rim, as shown in figure 4.16 c). To obtain this image, the infrared excitation laser was filtered out. Measuring the fluorescence spectrum on one of the waveguide ends while the laser is resonant with a cavity mode yields the result shown in figure 4.16 d). The mode structure of the resonator is apparent, superimposed on the broad emission of Er^{3+} , which comes from Er^{3+} ions located in the doped waveguide. Hence, infrared excitation light can be coupled to the cavity and simultaneously, green erbium emission can be extracted from the same cavity. The measurement of the linewidth of the resonances is limited by the spectrometer resolution to 140GHz. Linewidth measurements on this particular structure were carried out with a 636.5nm single mode laser. They reveal a spectral width of 34GHz, shown in figure 4.17. One would expect linewidths in the green spectral range to range between these two values. A lower limit for the quality factor is set by the spectrometer resolution of 140GHz, corresponding to $Q_{\text{erbium,green}} = 4000$.

Above results demonstrate, that erbium ions can retain their optical properties after implantation doping into Si:TiO_2 thin film, while the thin film maintains its waveguiding capabilities.

4.4 Thin Film Lithium Niobate on Insulator Platform

The creation of integrated photonic structures targeted at CQED experiments with rare-earth ions was discussed in the previous section on the example of
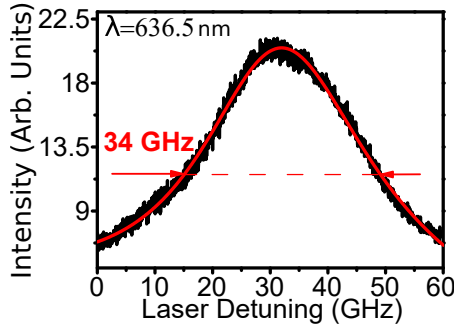
FIGURE 4.17: Spectral width of cavity mode measured at a wavelength of 636.5nm obtained by sweeping a single-mode laser through the cavity resonance.

Si:TiO$_2$ thin films, which specifically allow for enabling typical host crystals of rare-earth ions, such as YAG and YSO. The absence of any considerable second-order nonlinear susceptibility of the Si:TiO$_2$ thin film platform translates into a limited device tunablity. This can be seen as drawback in the pursuit of a scalable photonic platform and sparked the idea to combine rare-earth based CQED experiments with the recently developed and commercialized thin-film LN(LiNbO$_3$)-on-insulator technology. The most recent advances made with the LN-on-insulator (LNOI) platform harness the nonlinear and electro-optic properties of LN for various purposes, such as the realization of an electronically programmable photonic molecule [214], electro-optic frequency comb generation based on integrated LN resonators [215], and integrated LN electro-optic modulators [216]. These demonstrations underline the potential of the platform and provide valuable examples for the development of integrated rare-earth photonics with thin-film LNOI.

The outline of the investigation is the fabrication of rare-earth doped resonators with high Q/V-ratio and to subsequently use the electro-optical tuning capabilities of the material to achieve active device tuning, as first demonstrated by [217] for the integrated LN platform.

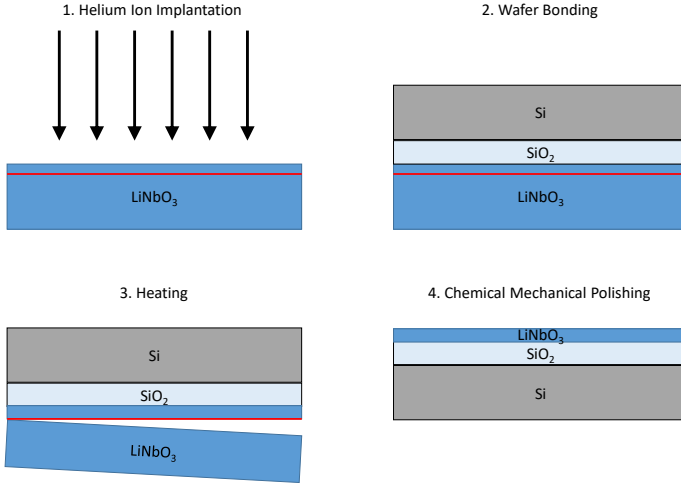## 4.4.1 Fabrication of Microcavities out of Lithium Niobate on Insulator

FIGURE 4.18: Process steps for production of LNOI wafers. 1. High energy helium ion implantation to produce damaged layer (red). 2. Wafer bonding to a substrate wafer, such as $Si(450\mu m)/SiO_2(2\mu m)$ for example. 3. Heating to induce breaking at damaged layer. 4. Chemical mechanical polishing of surface in order to obtain a low roughness LN thin film.

Before delving into the details of creating photonic devices out of LNOI, it is expedient to briefly illuminate the fabrication method of the platform itself. This also gives context for understanding how the previously mentioned advances made with LNOI were enabled. Conventionally, waveguides in LN are realized by titanium indiffusion proton exchange (Tipe) [218], resulting in a core-to-cladding index contrast of $\Delta n_{\text{Tipe}} \approx 0.1$, or by reverse proton exchange (RPE) [219] with index contrast of $\Delta n_{\text{RPE}} \approx 0.02$. Typical applications of these bulky waveguides, with lengths in the range of 5-10cm, are wavelength conversion based on periodically poled lithium niobate waveguides [220] and electro-optic modulators [221]. The low index contrast comes with

large optical mode sizes on the order of several microns and also large bend-ing radii in the range of millimeters, prohibitive for high Q/V-ratio cavities. The development of thin film LNOI based on the ion slicing technique [222, 223, 224] initiated a shift of paradigm, as high index contrasts, tight light con-finement, and larger light-matter interaction became an option. Ion slicing works as an epitaxial liftoff of single-crystal materials, and it typically uses high energy hydrogen or helium ion implantation to create a buried damage layer emerging from the inflicted implantation damage. The thin film LNOI production process is depicted in figure 4.18. In an annealing treatment fol-lowing the implantation, a damage and annealing stress-induced splitting then results in a thin LN film of high crystalline quality with a thickness defined by the implantation energy. For a helium ion implantation with an energy of 500keV into LN, the depth distribution of produced vacancies is given in figure 4.19, simulated with SRIM [122]. A confined damage layer with up to an order of magnitude more produced vacancies becomes aparent from these simulations.
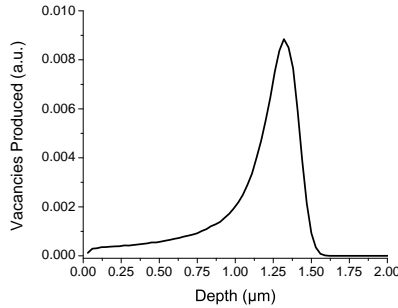
FIGURE 4.19: Simulated produced vacancies from a helium ion implantation with an energy of 500keV into LN as a function of depth. SRIM was used for simulations [122].

If the split-off thin film with refractive index of $n_{\text{LN}} \approx 2.2$ [225, 226] is bonded to a low index material, such as SiO_2 ($n_{\text{SiO}_2} \approx 1.5$), a high index contrast, needed for tight light confinement, is obtained. Typical specifications of

commercially available (NanoLN) LNOI wafers used within the context of this project are (from bottom to top layer): 450μm p-doped silicon, 2μm of thermally grown silicon dioxide, 470nm z-cut LN.
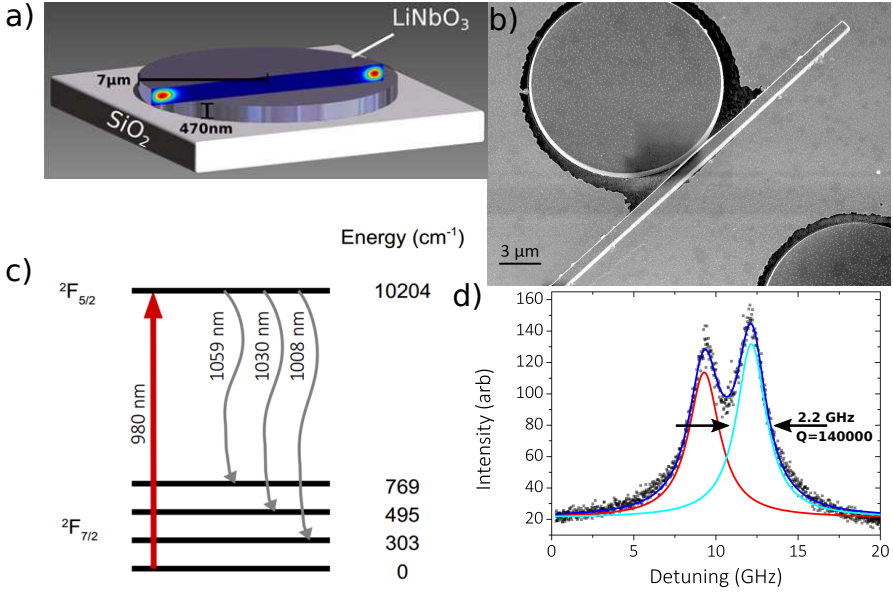

FIGURE 4.20: a) Finite element method simulation of fabricated resonator geometry with a radius of 7μm. b) Secondary electron microscopy image of a fabricated LNOI resonator and an evanescently coupled waveguide. c) Electronic level structure of Yb^{3+} in $LiNbO_3$ of the $^2F_{7/2}$ ground state and its four crystal-field levels and the lowest crystal field level of the $^2F_{7/2}$ excited state [227]. d) Measurement of the spectral width of cavity modes realized by sweeping a single-mode laser through resonances. Laser was injected into the waveguide and the detected signal is Yb^{3+} fluorescence from the WGM. A measured spectral width of 2.2GHz corresponds to a Q-factor of 140000.

In order to obtain a high Q/V-ratio, FEM simulations were carried out for light with 980nm wavelength (due to ytterbium doping discussed below) to

find a suitable radius for microdisk resonators, such that fabricated structures do not suffer from radiative loss. The geometry shown in image 4.20 a) was subsequently chosen and converted into a mask design.

The fabrication process is based on a lift-off procedure with slight adaptations to the sequence diagram shown in figure A.3 in the appendix. LNOI samples were covered with 30nm titanium by electron-gun evaporation and subsequently covered with a double-layered positive tone PMMA electron beam resist. The purpose of the titanium layer was to prevent the PMMA resist from cracking due to electron beam exposure when structures were defined. After exposure and resist development, 160nm of nickel-chromium (ratio of 80/20) mask was evaporated onto the sample and patterns were obtained through a lift-off procedure. These patterns were then transferred into LN through RIE with SF_6 plasma[228, 229]. Process pressure was 7mTorr and the DC-bias ranged at about 450V (PlasmaPro 80 RIE, Oxford Instruments). The high etch selectivity between nickel-chromium hard mask and LN caused the metal mask to sustain the etching of 470nm LN. The remaining nickel-chromium was dissolved in acidic chromium etchant mixed with nitric acid in a 1:1 ratio at elevated temperatures of roughly 60°C . The remaining titanium was removed in a subsequent acid piranha (1:1 to 2:1 ratio mix of H_2SO_4 and H_2O_2) cleaning step to facilitate efficient light propagation without metal induced light absorption. An SEM image of a typical structure is shown in figure 4.20 b). The black halo around the microdisk corresponds to the subjacent silicon dioxide, which appears at the surface in proximity to the edges of the disk due to increased dry etching speed.

After light propagation in fabricated structures was confirmed, implantation doping of Yb with an energy of 56keV and a fluence $F_{Yb,56keV} = 10^{15}$ ions/cm² was carried out. Rare-earth doping of LN was studied previously [230, 231, 232] and it is known, that optically active rare-earth ions replace lithium [231]. Subsequent annealing at 550°C for 8 hours in ambient atmosphere after the ion implantation resulted in detectable Yb^{3+} fluorescence under 980nm wavelength excitation, matching the electronic level structure

of Yb^{3+} in LN [227] (depicted in figure 4.20 c). Fluorescence of Yb^{3+} was filtered with a 1000nm long-pass filter in order to reject excitation laser light. Optical characterisation of a representative disk resonator around 980nm wavelength yields two spectrally almost degenerate cavity modes. Shown in figure 4.20 c) is the linewidth measurement of a WGM-pair. From a Lorentzian function fitting, which yields a width of 2.2GHz, we can estimate the loaded quality factor $Q = 1.4 \cdot 10^5$. A known problem of the fluorine-based dry etching of LN is the formation of non-volatile lithium fluoride, which results in LiF re-deposition and a corresponding increase in sidewall roughness [233]. We conjecture, that the LiF-induced sidewall roughness represents the main limitation for the measured quality factor of fabricated WGMRs.

4.4.2 Electro-Optical Tuning and Rare-Earth Implantation Doping of LN Microcavities

Since the early days of optical fiber communication, the material choice for electro-optic modulators is lithium niobate, owing to its outstanding properties - such as a large electro-optic coefficient, high intrinsic bandwidth (a THz operating bandwidth was demonstrated [234]), and wide transparency window ranging from 350nm to 5μm [225]. In the context of electro-optic microcavity resonance tuning, the large second order electro-optic coefficient ($r_{33} = 34$pm/V in the case of z-cut LN) enables the experiments discussed in the following. Estimation of the maximum change of the refractive index Δn_{eo} based on the electro-optic effect in the material can be done with the following relation [225]:

$$\Delta n_{\mathrm{eo}} = \frac{n^3}{2} r_{33} E_{\mathrm{z}}, \tag{4.35}$$

where n is the refractive index and E_{z} is the amplitude of the electric field applied along the microdisk axis, coinciding with the z-axis of the LN crystal in our case. The coercive field defines the field strength at which a ferroelectric domain reversal in LN occurs. To avoid uncontrolled polarization

of domains in LN, the coercive field is defined as maximum electric field in these considerations. For a coercive field strength of $E_{\text{coercive}} = 21\text{kV/mm}$ for congruent lithium niobate [235, 236, 237], the corresponding maximum change of refractive index is $\Delta n_{\text{eo,max}} \approx 3 \cdot 10^{-3}$. Here, congruent LN refers to the nonstoichiometry of the grown crystal defined by the parameter X_c as the ratio of Li content to the total amount of cations Li+Nb. Congruent LN is grown from lithium deficient melt with $X_c = 48.6\%$, which is also the conventionally used material [238, 239]. It was shown, that intrisic defects related to the nonstoichiometry has a strong influence on the nonlinear optical properties of LN, hence worse performing crystals grown from melts with stoichiometric composition $X_c = 50\%$ are less common[239]. In terms of LN composition, oftentimes around 5% magnesium oxide is doped into congruent LN, as it was shown to help reduce photorefraction, or optical damage when congruent LN is subjected to high optical intensities for applications involving nonlinear optics [240], such as periodically poled lithium niobate for example. The MgO doping results in replacement of the congruent LN crystal's point defects [241], which is accompanied by a decreased coercive field compared to undoped LN, reducing the poling fields to engineer ferroelectric domains [242].

In order to study the electro-optic tuning of fabricated cavities, the sample material stack depicted in figure 4.21 a) was made. It was realized by spin coating an SU-8 photoresist layer onto fabricated LN resonators and subsequently depositing indium tin oxide (ITO) of around 30nm by magnetron sputtering. SU-8 photoresist material has the beneficial properties of a high dielectric strength of 4.4MV/cm [243] and can conveniently be removed by acid cleaning, if required, as it is a purely organic material. ITO is an optically transparent oxide with electrical conductivity and served as top electrode in our experiments. The counter electrode was represented by the p-doped silicon substrate, such that an electric field could be applied across the material stack. With a dielectric strength of 5.6MV/cm for silicon dioxide [244], the

coercive field strength of 21kV/mm of LN is the main limitation to the maximum applied voltage and the tuning range of the fabricated device. When all three layers (silica, LN, SU-8) depicted in figure 4.21 a) are considered serially connected capacitors, we can estimate the maximum applied electric field by assuming charge conservation:

$$
\begin{aligned}
Q &= Q_{\text{silica}} = Q_{\text{LN}} = Q_{\text{SU}-8} & (4.36)\\
&= C_{\text{silica}} \cdot V_{\text{silica}} = \frac{\epsilon_{\text{Silica}} A}{d_{\text{silica}}} V_{\text{silica}} & (4.37)\\
&= C_{\text{LN}} \cdot V_{\text{LN}} = \frac{\epsilon_{\text{LN}} A}{d_{\text{LN}}} V_{\text{LN}} & (4.38)\\
&= C_{\text{SU}-8} \cdot V_{\text{SU}-8} = \frac{\epsilon_{\text{SU}-8} A}{d_{\text{SU}-8}} V_{\text{SU}-8}. & (4.39)
\end{aligned}
$$

Here, Q denotes the charge accumulated in each layer, C the capacitance of the respective layer, V the voltage drop at the respective layer, A the area of the layer, d the thickness of the individual layer, and ϵ the permittivity. For SU-8 the relative permittivity is $\kappa_{\text{SU}-8} = \epsilon_{\text{SU}-8}/\epsilon_0 \approx 3$ [245], for silica the relative permittivity is $\kappa_{\text{Silica}} = \epsilon_{\text{Silica}}/\epsilon_0 \approx 3.9$ [246] and for LN, it is $\kappa_{\text{LN}} = \epsilon_{\text{LN}}/\epsilon_0 \approx 28$[225, 226]. The thicknesses are $d_{\text{silica}} = 2000$nm for silica, $d_{\text{LN}} = 470$nm for LN, and $d_{\text{SU}-8} \approx 800$nm for SU-8. With a maximum voltage drop of $21\text{kV/mm} \cdot 470\text{nm} = 9.87$V in the LN layer, we find the maximum voltage V_{total} one can apply before repolarization of LN domains based on $V_{\text{total}} = V_{\text{silica}} + V_{\text{LN}} + V_{\text{SU}-8} = V_{\text{LN}}(1 + C_{\text{LN}}/C_{\text{silica}} + C_{\text{LN}}/C_{\text{SU}-8}) = 468$V.
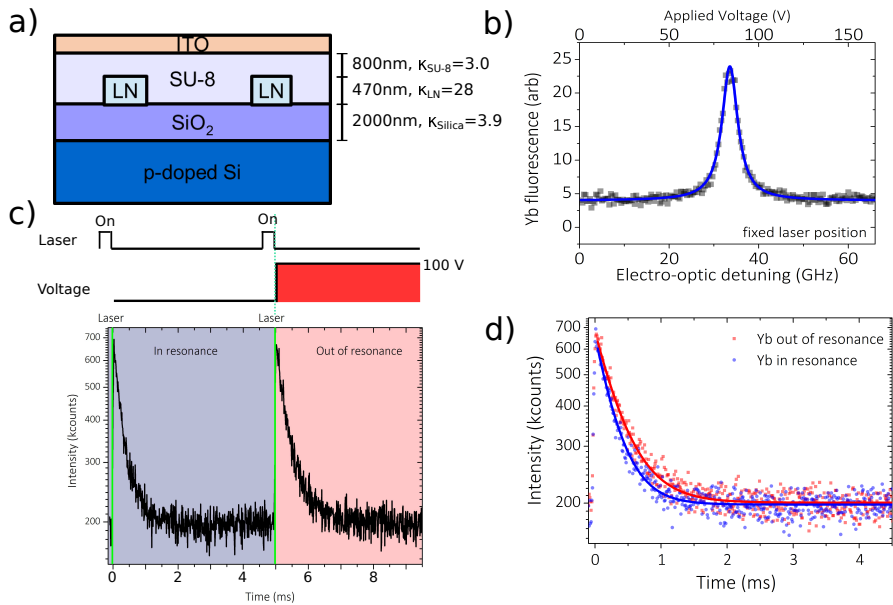
FIGURE 4.21: a) Sample material stack that allowed for electro-optic detuning experiments. The thicknesses and relative permittivities of the silica layer, LN layer and SU-8 layer are given. b) Demonstration of the electro-optic detuning capabilities for LNOI resonators. Yb^{3+} fluorescence was detected from the disk while an applied electric field was swept between 0V and 160V and while the single-mode laser was kept at a spectrally fixed position and was injected into the waveguide. c) Measurement sequence used to obtain electro-optically modulated optical lifetime measurements of Yb^{3+}. d) Electro-optically modulated optical lifetime measurements of Yb^{3+}. The single-mode laser was exciting a diffraction limited spot of Yb^{3+} on the resonator while the resonator mode was electrooptically shifted in and out of the laser frequency.

In order to stay well below the repolarization threshold and avoid uncontrolled electrical shorts in the sample, applied voltages were restricted to 160V in experiments. In figure 4.21 b), the electro-optic detuning experiment is shown. In this demonstration, the single-mode laser was kept at fixed

spectral position while coupling into the waveguide and the applied voltage was simultaneously swept between 0V and 160V. These voltage sweeps translate into electro-optic tuning of the resonator mode and also brought the cavity in resonance with the laser. Accordingly, Yb^{3+} located in the cavity is excited by the laser and fluorescence related of the cavity tuning can be detected on the rim of the cavity. The observed electro-optic resonator tuning in this experiment amounts to 400MHz/V for the studied sample stack.

In order to estimate the expected maximum lifetime shortening based on the Purcell effect, the necessary items of equation 4.13 are collected in the following. The loaded quality factor of the cavity is $Q = 1.5 \cdot 10^5$. Based on FEM simulations (shown in figure 4.20 a), we obtain a mode volume for the disk resonator with $7\mu m$ radius of $V \approx 80 \cdot (\lambda/n)^3$. Accordingly, fabricated disk resonators can in principle provide an emission rate enhancement of $F_P = 125$. Due to the fact, that implanted Yb^{3+} ions are not located at the maximum of the WGM electric field, a decrease in obtainable emission rate enhancement can be estimated. Based on SRIM simulations, the Yb ions, implanted with 56keV, are located 19nm below the surface [122]. This corresponds to a reduction of approximately factor 3 in Purcell enhancement. Futhermore, based on the electronic level structure of Yb^{3+} in LN, we have to consider the branching ratio $\beta \approx 0.25$ due to the four-fold crystal field splitting of the $^2F_{7/2}$ ground state. Maximum expected lifetime shortening of Yb^{3+} in the fabricated LN cavity is then $F_{P,Yb} = F_P \cdot \beta \cdot \frac{1}{3} \approx 10$. This value, however, assumes an optimal alignment of local cavity polarization with the dipole moment orientation of the emitter, thus maximizing $|\mathbf{d} \cdot \mathbf{E}|$ (from equation 4.14). In an ensemble measurement, this dipole moment orientation will be averaged, contributing a foreseeable decrease in lifetime shortening by a factor 3. Ultimately, an ensemble lifetime shortening by a factor 10/3 is expected.

To confirm these estimations, the excited state lifetime shortening of Yb^{3+}

ions was investigated. We resonantly excited only a diffraction-limited sub-section of Yb^{3+} ions located in the disk resonator and measured their fluorescence lifetime at cryogenic temperature of around 4K. For Czochralski grown Yb:LN samples, these temperatures are sufficiently low to observe homogeneous emitter linewidths of up to 40MHz [230]. Electro-optical tuning of the resonator then allowed for controlled measurements of lifetime shortening of one and the same subsection of Yb^{3+} ions, by shifting the resonator mode accordingly, while the excitation laser stayed spectrally fixed. The measurement sequence is shown in figure 4.21 c), where a lifetime measurement in the fashion of a short excitation laser pulse followed by signal acquisition time is alternatingly taken with and without applied voltage of 100V. Figure 4.21 d) depicts the corresponding lifetime measurements. In the comparison it becomes apparent, that only a minor lifetime shortening of Yb^{3+} ions is obtained. Exponential fittings reveal the lifetime of Yb^{3+} out of resonance $\tau_{off} = 0.389$ms and the lifetime of Yb^{3+} in resonance $\tau_{on} = 0.305$ms. The fact, that the measured ensemble Purcell enhancement stays far below the expected value can be explained by the high peak concentration of Yb^{3+} ions in our devices based on the fluence of 10^{15}ion/cm^2. With a peak Yb concentration of 2.6%, dipolar interaction between neighboring Yb ions plays a dominant role and induces dephasing, which can lead to broadened optical transitions of implanted Yb^{3+} ions [26]. In this scenario, the Q-factor of the cavity would not be the limitation to the obtainable Purcell enhancement, but rather the 'emitter-Q' or spectral width of the optical transition of Yb^{3+} ions. Then, only a small fraction (the least interacting ones) of Yb^{3+} ions would experience a Purcell-effect induced lifetime shortening, overshadowed by a majority of quasi unaffected emitters.

Several observations indicate the emitter-Q to be the issue: At low temperature under single mode laser excitation, the expected amount of fluorescent Yb^{3+} ions should be considerably lower than at room temperature, provided the laser is not much broader than several tens of MHz. Taking the lower limit of reported values for the inhomogeneous linewidth of Yb^{3+} :LN for

Czochralski-grown single crystals (which should have higher crystallinity compared to ion-sliced and implanted thin films) $\gamma_{\text{inhom}} \approx 30\text{GHz}$ and the upper limit of the homogeneous linewidth $\gamma_{\text{hom}} \approx 40\text{MHz}$, one would expect a decrease in signal on the order of $\gamma_{\text{inhom}}/\gamma_{\text{hom}}$ which ranges between $10^2 - 10^3$ [230]. In our experiments, however, the signal decrease stayed below factor 10, indicating that a large fraction of implanted Yb ions participate in signal generation, even at low temperature under single mode laser excitation.
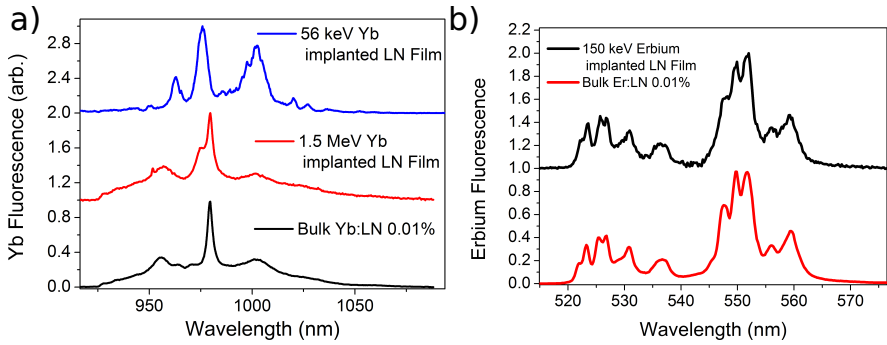

FIGURE 4.22: a) Fluorescence spectra of different Yb^{3+} :LN samples, taken at room temperature and plotted offset vertically for clarity. b) Fluorescence spectra of different Er^{3+} :LN samples, taken at room temperature.

A second observation, that indicates optical transitions of 56keV-implanted Yb^{3+} ions are broader than expected, is related to the fluorescence spectra, which were taken on different Yb^{3+} :LN samples and are shown in figure 4.22 a). Spectra are plotted offset vertically for clarity and were taken on 56keV-implanted LNOI, 1.5MeV-implanted LNOI with a fluence of $3 \cdot 10^{13}\text{ions}/\text{cm}^2$, and a Czochralski-grown 0.01% Yb:LN sample, obtained from colleagues led by Laszlo Kovacs (from Wigner Reseach Center, Budapest, Hungary) at room temperature. Both implanted thin film samples were annealed in ambient atmosphere at 550°C for 8 hours. It has to be noted, that annealing temperatures above 550°C led to uncontrolled breaking of the thin

LN film in annealing experiments, most likely caused by the large difference in thermal expansion coefficients between LN and the subjacent silica. The thermal expansion coefficients for LN are $\alpha_\parallel = 4.1 \times 10^{-6}$/K parallel to the z-axis of the LN crystal and $\alpha_\perp = 14.8 \times 10^{-6}$/K perpendicular to the z-axis of LN crystal [247]. In the case of our z-cut thin film LN, $\alpha_\perp$ is the relevant quantity, which is deviating strongly from the thermal expansion coefficient of silica with $\alpha_{\text{silica}} = 0.56 \times 10^{-6}$/K [248]. Annealing temperatures above 1000°C are known to facilitate Yb diffusion in LN and is discussed as alternative to doping during crystal growth [249]. Also, the same temperature range is used to heal out implantation damage and incorporate implanted rare-earth ions into the LN matrix [232]. However, it is an open question to what degree annealing at temperatures up to the 550°C -limit can restore bulk-like optical properties of Yb^{3+} . When taking the bulk crystal spectrum shown in figure 4.22 a) as reference, the 1.5MeV-implanted Yb^{3+} fluorescence shows striking similarities. Merely an additional 'shoulder-peak' appears in the implanted thin film spectrum at 975nm wavelength, which can be related to Yb ions reaching into the silica layer during implantation (according to SRIM simulations [122]). This comparison suggests that a majority of high-energy implanted Yb ions are located in an environment comparable to their counterparts in the Czochralski-grown bulk sample. Contrary to the high energy Yb ion-implanted thin LN film with a peak Yb concentration of 0.01%, the low energy Yb ion-implanted thin LN film with peak concentration of 2.6% deviates strongly from the bulk emission spectrum. The differences in the emission spectra shown in figure 4.22 a) suggest, that crystal damage was not healed out completely for the 56-keV implanted thin LN film, presumably due to too high implantation fluence and too low annealing temperature. In this scenario, the LN host can resemble a glassy environment, such as SiO_2, where a steep temperature dependence of the homogeneous linewidth of incorporated Yb^{3+} ions has been shown. Also, the degree to which Yb^{3+} ions in glassy SiO_2 host can maintain their initial dipole direction (dipole polarization) during the lifetime measurement is known to decrease exponentially with rising temperature [181]. Too high temperatures during

Purcell enhancement measurements shown in figure 4.21 c) can therefore not be excluded as a reason for the unexpectedly low lifetime enhancement, that was observed. Further spectroscopic studies of implanted Yb^{3+} :LN, presumably at temperatures down to the millikelvin range, could illuminate the currently unclear optical properties of implantation-doped Yb ions.

Low rare-earth concentrations in LN created by ion implantation were observed to yield bulk-like emission spectra for Yb^{3+} ions at room temperature. In order to confirm these results with a second rare-earth species, erbium ions were implanted into thin film LNOI. Erbium provides access to telecom band optical transitions and is therefore particularly interesting for future applications. The erbium ion implantation was conducted with 150keV energy and a fluence of $F_{\text{erbium}} = 10^{12}$ions/cm^2. This results in an erbium peak concentration of 0.001%, according to SRIM simulations [122]. After annealing at 550°C for 8 hours, the two-photon upconversion emission spectrum of Er^{3+} :LN is compared to a bulk grown 0.01% Er^{3+} :LN sample obtained from Roditi International Corporation Ltd. Optical properties of trivalent erbium related to two-photon upconversion are discussed in section 4.3.5. The spectra shown in figure 4.22 b) share their features to a high degree. As a result, based on annealing treatment at comparably low temperatures of 550°C , erbium is incorporated into the LN matrix in the trivalent charge state, and no significant differences in the upconverted emission spectrum are seen. This indicates, that low rare-earth concentrations generated by implantation doping in LN do not deteriorate optical properties at room temperature.

4.5 Rare-Earth Ions Coupled to Microcavities - Conclusion and Outlook

In this chapter, two different experimental photonic platforms for integrating rare-earth ions into microcavities were presented, both with unique prospects for realizing rare-earth ion based quantum architectures.

For the Si:TiO$_2$ thin film platform, fabrication of waveguides and waveguide-coupled WGMRs was shown for several substrate materials, such as quartz, YAG, and sapphire. Based on the optical properties of the Si:TiO$_2$ thin film with amorphous phase, unprecedented propagation loss in waveguides at 800nm wavelength was demonstrated. Evanescent coupling between the waveguide mode and rare-earth emitters located in a subjacent host crystal was demonstrated. Also, rare-earth implantation doping of Si:TiO$_2$ thin film was achieved. The Si:TiO$_2$ thin film platform was shown to provide a potentially impactful route towards CQED experiments with integrated rare-earth ions. Next step with this platform could be single rare-earth ion detection based on Purcell-enhanced optical transitions with a view to studying the coherent properties of the spin system. With only 5% of ^{29}Si nulcear spins and 25% silicon content in Si:TiO$_2$ thin films and 13% of titanium isotopes with odd mass number, the nulcear spin density is low compared to other waveguiding platforms, such as AlN or LN. This can translate into long coherence times of doped rare-earth electron spins and can simultaneously provide access to proximal nuclear spins, as demonstrated in chapter 2.

For the LNOI platform, we showed high-Q microresonators doped with Yb^{3+} . In principle, fabricated structures allow for Purcell enhancement for Yb^{3+} emitters. Limited by the low energy and high dose implantation of Yb in these structures, the expected magnitude of lifetime shortening could not be observed. As a consequence, lower dopant concentrations were investigated and it was demonstrated, that implantation doping of rare-earth emitters into thin film LNOI can result in an appreciably high agreement of fluorescence spectra between bulk grown samples with implanted ones. Electro-optic control of resonator modes was demonstrated furthermore. For the future, high enough Purcell enhancement of low dose and high energy implantation doped Yb^{3+} , and also the associated detection of a single Yb^{3+} ion remains yet to be demonstrated. High outcoupling efficiency of signal from the integrated waveguide mode to the photodetector will be detrimental to single ion detection and its systematic investigation can unlock a boost

in signal collection efficiency. Various directions for efficient light extraction from integrated waveguides are used and proposed, such using a lensed fiber for coupling to waveguides, integrated grating couplers, or inverse-designed couplers [18, 250, 251]. Undoubtedly, even higher quality factors of fabricated microresonators will also benefit both, single ion detection experiments and further studies of their spin properties in the LN host crystal. This work will greatly benefit from fabrication techniques, that allowed quality factors of up 10^7 [252], which are based on pure mechanical RIE in argon plasma and avoid lift-off techniques. The same purely mechanical argon RIE recipe, which allows to increase quality factors of up to two orders of magnitude over results shown here, could also be applied to other smart-cut thin film oxide crystals, as they tend to elude chemical dry etching. Scalable structuring of thin films made from such an attractive class of materials can open up their use in integrated optics furthermore. Ultimately, provided single ion detection is accomplished, the LNOI platform is particularly well-suited for measuring photon indistinguishability between two remote rare-earth ions using an Hong-Ou-Mandel interferometer [253]. The large electro-optic resonance tuning range provided by LN allows for fabricated resonators to be brought in resonance with each other flexibly. This measurement would set the foundation for entanglement between two distant rare-earth emitters, a milestone which should have major implications when realized in a scalable platform, such as LNOI.

Appendix A

Appendices

A.1 Physical constants

Constant	Description
c	$= 2.99792458 \cdot 10^8 \text{m} \cdot \text{s}^{-1}$, speed of light in vacuum
e	$= 1.602177 \cdot 10^{-19}$C, elementary charge
μ_0	$= 4\pi \cdot 10^{-7}\text{NA}^{-2}$, magnetic constant
ϵ_0	$= \frac{1}{c^2 \mu_0} = 8.854187 \cdot 10^{-12}\text{F} \cdot \text{m}^{-1}$, dielectric constant
μ_B	$= \frac{e\hbar}{2m_e} = 9.274010 \cdot 10^{-24}\text{J} \cdot \text{T}^{-1}$, Bohr magneton
μ_N	$= 5.050783 \cdot 10^{-27}\text{J} \cdot \text{T}^{-1}$, nuclear magneton
h	$= 6.626070 \cdot 10^{-34}$Js, Planck constant
$\hbar$	$= h/(2\pi) = 1.054571 \cdot 10^{-34}$Js, reduced Planck constant

TABLE A.1: Physical constants.

A.2 Annealing of Pr^{3+}:YAG Samples

After single praseodymium ion implantation, the YAG crystal was annealed in air with the following procedure:

Starting at room temperature, the oven was ramped to 800°C at a rate of 5°C /minute, then ramped to 1200°C at a rate of 3°C /minute and held at 1200°C for one minute. Then, the oven was ramped down to 800°C at a rate of 3°C /minute and then cooled down to room temperature at an uncontrolled rate.

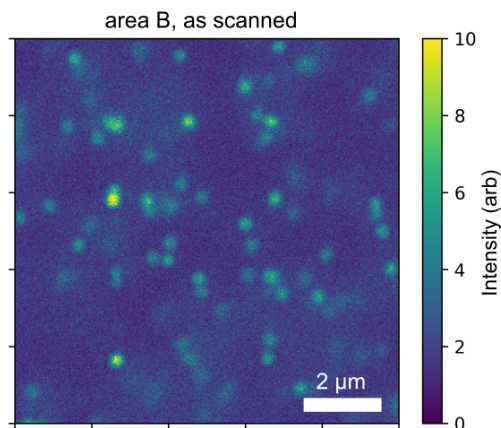## A.3   Background Correction - Single Ion Implanted Praseodymium Grid

FIGURE A.1: Upconverting laser scan taken at implanted area B of the crystal.

Figure A.1 shows the upconverting laser scan of area B after implantation and annealing. Implanted spots cannot be easily distinguished from background signal. Background corrected data is shown in the main part in figure 3.12 on the righthand side.

The background correction procedure applied to laser scanning upconverting microscope images taken of the unimplanted and the implanted and

annealed sample were realized by minimization of the mean squared error of the residual background intensity as estimator. The residual background intensity (amounting to around -2.5 as shown in A.2) emerges from unequal laser power between scans and the corresponding change in signal-to-background ratios between the scans. Minimization of the mean squared error of the estimator was realized by iterative translation, rotation and intensity scaling. In order to avoid inhomogeneities of the background intensity due to implanted spots, the estimator was confined to the unimplanted area by cropping out implantation spots.
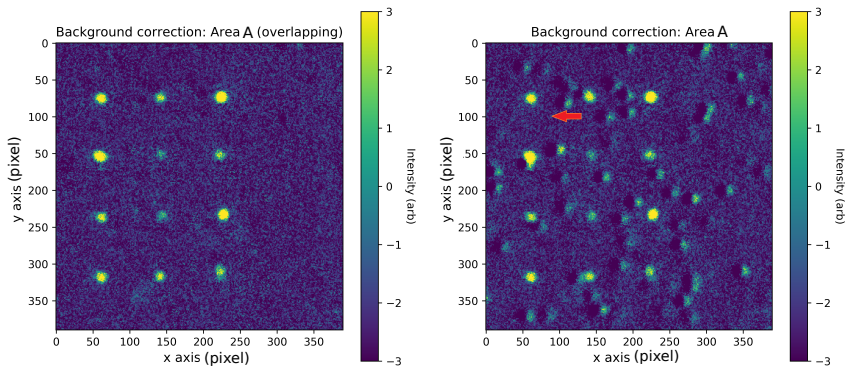

FIGURE A.2: Background correction: Left image shows overlap between scans before implantation and after implantation and annealing. Right image shows lateral offset between the two scans.

Spot no.	Spot count [kcounts]	Ions per spot [in units of C_A]	Rounded [ions/spot]
1	1231	3.12	3
2	778	1.97	2
3	1998	5.06	5
4	1883	4.77	5
5	396	1	1
6	732	1.85	2
7	871	2.21	2
8	434	1.1	1
9	1516	3.84	4
10	1105	2.8	3
11	717	1.82	2
12	876	2.22	2
Sum	-	-	32

TABLE A.2: Accumulated fluorescence signal on spots in area A. Sums take into account a circular cropped out region of pixels of the raw collected data on the respective regions minus the average background in proximity of this crop out defined by a donut shaped outer lying second crop out of raw pixels. Pixel size is 25 nm and pixel integration time is 6 ms on all taken scans. Average summed up single ion fluorescence counts are $C_A = 395$kcounts and corresponds to the area under the fitted 2D-Gaussian.

Spot no.	Spot count [kcounts]	Ions per spot [in units of C_B]	Rounded [ions/spot]
1	900	2.69	3
2	677	2.03	2
3	723	2.16	2
4	956	2.86	3
5	299	0.9	1
6	702	2.1	2
7	563	1.69	2
8	424	1.27	1
9	644	1.93	2
10	964	2.89	3
11	371	1.11	1
12	413	1.24	1
Sum	-	-	23

TABLE A.3: Accumulated fluorescence signal on spots in area B. Sums take into account a circular crop out of pixels of the raw collected data on the respective regions minus the average background in proximity of this crop out defined by a donut shaped outer lying second crop out of raw pixels. Pixel size is 25 nm and pixel integration time is 6 ms on all taken scans. Average summed up single ion fluorescence counts are $C_B = 334$kcounts and corresponds to the area under the fitted 2D-Gaussian.

A.4   Chemical Beam Vapor Deposition of Si:TiO$_2$ Combinatorial Film

The detailed information about the deposition process of combinatorial Si:TiO$_2$ thin films can be found in [200]. The chemical beam vapor deposition is based on the thermal decomposition of organometallic precursors on the heated sample substrate under high vacuum conditions with pressures $\leq$ 10^{-3}Pa. When the precursors impinge upon the sample substrate as molecular beams, no gas phase reaction occurs. Sample substrate crystals were epipolished YAG, sapphire and quartz for characterization of waveguide functionality. For characterization of material properties, sample substrates were silicon and glass. The following organometallic precursors (in liquid phase) were used: titanium tetraisoporpoxide (Ti(OiPr)$_4$, CAS 546-68-9, evaporated from a reservoir at 32°C) and tetrabutoxysilane (Si(OnBu)$_4$, CAS 4766-57-8, evaporated from a reservoir at 65°C). A homogeneous distribution of the Ti and Si precursor flow onto the sample with a flow ratio of Si/Ti$=$ 1.1 was realized. Substrate temperature during deposition was 500°C . These conditions resulted in a growth rate of 10nm/min and a Si doping of the film of about 25% (defined as Si/(Si+Ti) ratio), measured with SEM-EDX. Before film deposition, the chamber was pumped to a base pressure of 5×10^{-4}Pa and a liquid nitrogen-cooled cryo-panel was used to keep the pressure below 2×10^{-3}Pa during the deposition.

A.5   Nanofabrication Steps for Thin Film Samples

In the following, the generic lift-off fabrication procedure is given and illustrated in figure A.3. The procedure was applied to various thin film material and substrate material combinations and it typically requires specific adaptations to take differences in material chemistry and thickness into account. Details are discussed in the respective sections of the main text.

Thin film samples were covered with a double-layered positive tone PMMA electron beam resist by spin coating. The bottom layer (200K) has a shorter polymer chain length than the top layer (950K), which causes an undercut of the resist mask when exposed by the electron beam. This behavior is caused by differing exposure sensitivities between the two resist layers and is depicted in figure A.3. It aims for a metal mask lift-off step with a minimum of roughness at edges based on the undercut, which prevents the metal mask deposited on the thin film to be connected to the metal mask deposited on the electron beam resist layer. In this way, during the lift-off step, in which the PMMA resist is dissolved in NMP (2-Pyrrolidinone, 1-methyl-) or NEP (2-Pyrrolidinone, 1-ethyl-) at elevated temperatures between $60°C$ and $90°C$, no unwanted breaking of the thin metal mask is caused. While metal mask breaking can induce unwanted metal mask roughness, the goal is to leave only the unperturbed, as-evaporated metal mask on the thin film. Here, the thickness of the bottom PMMA resist layer limits the maximum thickness of the deposited metal mask, due to the danger of metal mask merging while deposition. However, an important consideration is, that large thicknesses of PMMA resist translate into reduced patterning resolution. This is based on the fact, that high ratios between thickness and width of PMMA structures (aspect ratio) render the PMMA structures unstable and leads to tipping over. After the reactive ion etching step, the residual metal mask is removed by wet etching in acidic solution and only the imprinted thin film structures are left. In order to activate photonic structures with fluorescent centers, a post-fabrication implantation step and an annealing step is appended.
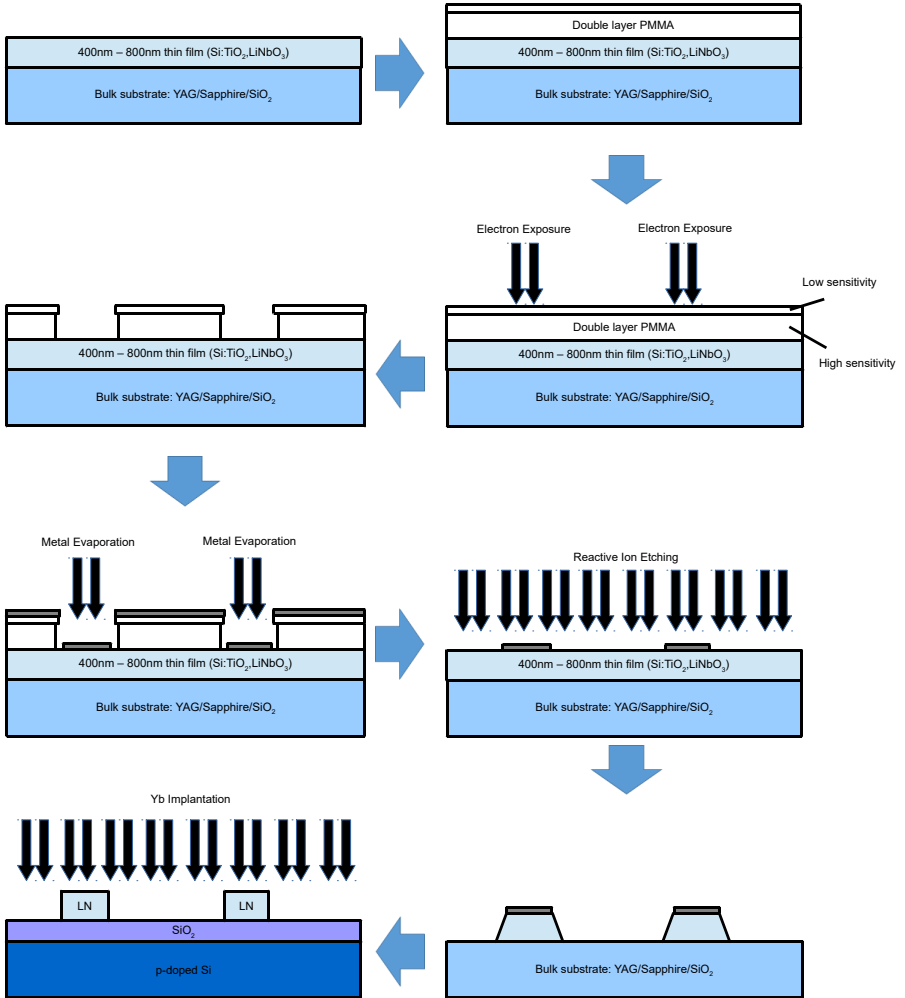
FIGURE A.3: Generic lift-off fabrication procedure depicted as a sequence diagram. It was used for various thin film material and substrate material combinations with small adaptations, mainly regarding metal mask and reactive ion etching. The exact details are discussed in the respective sections of the main text.

Bibliography

[1] Richard P. Feynman. "Simulating physics with computers". In: *International journal of theoretical physics* 21.6 (1982), pp. 467–488 (cit. on p. 4).

[2] P. W. Shor, ed. *Algorithms for quantum computation: discrete logarithms and factoring: Proceedings 35th Annual Symposium on Foundations of Computer Science*. 1994. DOI: `10.1109/SFCS.1994.365700` (cit. on p. 4).

[3] Michael A. Nielsen and Isaac L. Chuang. *Quantum Computation and Quantum Information: 10th Anniversary Edition*. Cambridge: Cambridge University Press, 2010. ISBN: 9781107002173 (cit. on p. 4).

[4] A. G. J. MacFarlane, Jonathan P. Dowling, and Gerard J. Milburn. "Quantum technology: the second quantum revolution". In: *Philosophical Transactions of the Royal Society of London. Series A: Mathematical, Physical and Engineering Sciences* 361.1809 (2003), pp. 1655–1674. DOI: `10.1098/rsta.2003.1227` (cit. on p. 4).

[5] Mark Fox. *Quantum optics: an introduction*. OUP Oxford, 2006. ISBN: 0191524255 (cit. on pp. 5, 94).

[6] David P. DiVincenzo. "Two-bit gates are universal for quantum computation". In: *Physical Review A* 51.2 (1995), pp. 1015–1022. DOI: `10.1103/PhysRevA.51.1015` (cit. on p. 6).

[7] David P. DiVincenzo. "The Physical Implementation of Quantum Computation". In: *Fortschritte der Physik* 48.9–11 (2000), pp. 771–783. DOI: `10.1002/1521-3978(200009)48:9/11<771::AID-PROP771>3.0.CO;2-E` (cit. on p. 6).

[8]   Robert Raussendorf and Jim Harrington. "Fault-Tolerant Quantum Computation with High Threshold in Two Dimensions". In: *Physical Review Letters* 98.19 (2007), p. 190504. DOI: `10.1103/PhysRevLett.98.190504` (cit. on pp. 7, 8).

[9]   Michael Edward Beverland. "Toward realizable quantum computers". PhD thesis. California Institute of Technology, 2016 (cit. on p. 7).

[10] Antonio Acín et al. "The quantum technologies roadmap: a European community view". In: *New Journal of Physics* 20.8 (2018), p. 080201. DOI: `10.1088/1367-2630/aad1ea` (cit. on pp. 7, 8).

[11] Austin G. Fowler et al. "Surface codes: Towards practical large-scale quantum computation". In: *Physical Review A* 86.3 (2012), p. 032324. DOI: `10.1103/PhysRevA.86.032324` (cit. on p. 8).

[12] C. Pomerance. "Tale of two sieves". In: *Notices American Mathematical Society* 43.12 (1996), pp. 1473–1485 (cit. on p. 8).

[13] John Preskill. "Reliable quantum computers". In: *Proceedings of the Royal Society of London. Series A: Mathematical, Physical and Engineering Sciences* 454.1969 (1998), pp. 385–410. DOI: `10.1098/rspa.1998.0167` (cit. on p. 8).

[14] Frank Arute et al. "Quantum supremacy using a programmable superconducting processor". In: *Nature* 574.7779 (2019), pp. 505–510. DOI: `10.1038/s41586-019-1666-5` (cit. on p. 8).

[15] H. J. Kimble. "The quantum internet". In: *Nature* 453.7198 (2008), pp. 1023–1030. DOI: `10.1038/nature07127` (cit. on pp. 8, 93).

[16] David D. Awschalom et al. "Quantum technologies with optically interfaced solid-state spins". In: *Nature Photonics* 12.9 (2018), pp. 516–527. DOI: `10.1038/s41566-018-0232-2` (cit. on pp. 9, 17).

[17] Tian Zhong et al. "Nanophotonic coherent light–matter interfaces based on rare-earth-doped crystals". In: *Nature Communications* 6.1 (2015), p. 8206. DOI: `10.1038/ncomms9206` (cit. on pp. 9, 104).

[18] A. M. Dibos et al. "Atomic Source of Single Photons in the Telecom Band". In: *Physical Review Letters* 120.24 (2018), p. 243601. DOI: `10.`

1103 / PhysRevLett . 120 . 243601 (cit. on pp. 9, 13, 15, 66, 104, 105, 145).

[19]   Tian Zhong et al. "Optically Addressing Single Rare-Earth Ions in a Nanophotonic Cavity". In: *Physical Review Letters* 121.18 (2018), p. 183603. DOI: 10.1103/PhysRevLett.121.183603 (cit. on pp. 9, 13, 15, 66, 104).

[20]   Jonathan M. Kindem et al. "Coherent control and single-shot read-out of a rare-earth ion embedded in a nanophotonic cavity". In: *arXiv preprint arXiv:1907.12161* (2019) (cit. on pp. 9, 15, 18, 104).

[21]   Thomas Kornher et al. "Production yield of rare-earth ions implanted into an optical crystal". In: *Applied Physics Letters* 108.5 (2016), p. 053108. DOI: 10.1063/1.4941403 (cit. on pp. 9, 83, 122, 125, 128).

[22]   Karin Groot-Berning et al. "Trapping and sympathetic cooling of single thorium ions for spectroscopy". In: *Physical Review A* 99.2 (2019), p. 023420. DOI: 10.1103/PhysRevA.99.023420 (cit. on p. 9).

[23]   Christopher M. Phenicie et al. "Narrow Optical Line Widths in Erbium Implanted in TiO2". In: *Nano Letters* 19.12 (2019), pp. 8928–8933. DOI: 10.1021/acs.nanolett.9b03831 (cit. on pp. 9, 91).

[24]   Brian G. Wybourne. "Spectroscopic properties of rare earths". In: (1965) (cit. on p. 9).

[25]   Gerhard Heinrich Dieke, Henry Milton Crosswhite, and Hannah Crosswhite. "Spectra and energy levels of rare earth ions in crystals". In: (1968) (cit. on p. 9).

[26]   Guokui Liu and Bernard Jacquier. *Spectroscopic properties of rare earths in optical materials*. Springer Science & Business Media, 2006. ISBN: 3540282092 (cit. on pp. 9–11, 140).

[27]   C. W. Thiel, Thomas Böttger, and R. L. Cone. "Rare-earth-doped materials for applications in quantum information storage and signal processing". In: *Journal of Luminescence* 131.3 (2011), pp. 353–361. DOI: 10.1016/j.jlumin.2010.12.015 (cit. on p. 9).

[28]   Hugues de Riedmatten et al. "A solid-state light–matter interface at the single-photon level". In: *Nature* 456.7223 (2008), pp. 773–777. DOI: 10.1038/nature07607 (cit. on p. 9).

[29] S. Bertaina et al. "Rare-earth solid-state qubits". In: *Nature Nanotechnology* 2.1 (2007), pp. 39–42. DOI: `10.1038/nnano.2006.174` (cit. on p. 9).

[30] Theodore Gray. *Elements: A Visual Exploration of Every Known Atom in the Universe*. Black Dog & Leventhal, 2012. ISBN: 1603764054 (cit. on p. 10).

[31] R. W. Equall et al. "Ultraslow optical dephasing in Eu3+:Y2SiO5". In: *Physical Review Letters* 72.14 (1994), pp. 2179–2182. DOI: `10.1103/PhysRevLett.72.2179` (cit. on p. 10).

[32] Y. Sun et al. "Recent progress in developing new rare earth materials for hole burning and coherent transient applications". In: *Journal of Luminescence* 98.1 (2002), pp. 281–287. DOI: `10.1016/S0022-2313(02)00281-8` (cit. on p. 10).

[33] A. J. Freeman and R. E. Watson. "Theoretical Investigation of Some Magnetic and Spectroscopic Properties of Rare-Earth Ions". In: *Physical Review* 127.6 (1962), pp. 2058–2075. DOI: `10.1103/PhysRev.127.2058` (cit. on p. 11).

[34] Christiane Görller-Walrand and Koen Binnemans. "Rationalization of crystal-field parametrization". In: *Handbook on the physics and chemistry of rare earths* 23 (1996), pp. 121–283 (cit. on p. 12).

[35] Frank Träger. *Springer handbook of lasers and optics*. Springer Science & Business Media, 2012. ISBN: 3642194095 (cit. on p. 13).

[36] R. Kolesov et al. "Optical detection of a single rare-earth ion in a crystal". In: *Nature Communications* 3.1 (2012), p. 1029. DOI: `10.1038/ncomms2034` (cit. on pp. 13, 14, 66, 73–76, 120).

[37] Roman Kolesov et al. "Mapping Spin Coherence of a Single Rare-Earth Ion in a Crystal onto a Single Photon Polarization State". In: *Physical Review Letters* 111.12 (2013), p. 120502. DOI: `10.1103/PhysRevLett.111.120502` (cit. on pp. 13, 14, 35, 120, 125).

[38] Chunming Yin et al. "Optical addressing of an individual erbium ion in silicon". In: *Nature* 497 (2013), 91 EP –. DOI: `10.1038/nature12081` (cit. on pp. 13, 14).

[39] T. Utikal et al. "Spectroscopic detection and state preparation of a single praseodymium ion in a crystal". In: *Nature Communications* 5.1 (2014), p. 3627. DOI: 10.1038/ncomms4627 (cit. on pp. 13–15, 18).

[40] Roger M. Macfarlane. "High-resolution laser spectroscopy of rare-earth doped insulators: a personal perspective". In: *Journal of Luminescence* 100.1 (2002), pp. 1–20. DOI: 10.1016/S0022-2313(02)00450-7 (cit. on p. 13).

[41] J. J. Macklin et al. "Imaging and Time-Resolved Spectroscopy of Single Molecules at an Interface". In: *Science* 272.5259 (1996), pp. 255–258. DOI: 10.1126/science.272.5259.255 (cit. on p. 14).

[42] J. P. Hadden et al. "Strongly enhanced photon collection from diamond defect centers under microfabricated integrated solid immersion lenses". In: *Applied Physics Letters* 97.24 (2010), p. 241901. DOI: 10.1063/1.3519847 (cit. on p. 14).

[43] P. Siyushev et al. "Coherent properties of single rare-earth spin qubits". In: *Nature Communications* 5.1 (2014), p. 3895. DOI: 10.1038/ncomms4895 (cit. on pp. 14, 18, 51, 120).

[44] Kangwei Xia et al. "All-Optical Preparation of Coherent Dark States of a Single Rare Earth Ion Spin in a Crystal". In: *Physical Review Letters* 115.9 (2015), p. 093602. DOI: 10.1103/PhysRevLett.115.093602 (cit. on pp. 14, 23, 29, 125–127).

[45] Mouktik Raha et al. "Optical quantum nondemolition measurement of a solid-state spin without a cycling transition". In: *arXiv preprint arXiv:1907.09992* (2019) (cit. on p. 15).

[46] John J. L. Morton et al. "Solid-state quantum memory using the 31P nuclear spin". In: *Nature* 455.7216 (2008), pp. 1085–1088. DOI: 10.1038/nature07295 (cit. on p. 17).

[47] P. C. Maurer et al. "Room-Temperature Quantum Bit Memory Exceeding One Second". In: *Science* 336.6086 (2012), p. 1283. DOI: 10.1126/science.1220513 (cit. on p. 17).

[48] G. Waldherr et al. "Quantum error correction in a solid-state hybrid spin register". In: *Nature* 506 (2014), 204 EP –. DOI: `10.1038/nature12919` (cit. on pp. 18, 64).

[49] L. Childress et al. "Coherent Dynamics of Coupled Electron and Nuclear Spin Qubits in Diamond". In: *Science* 314.5797 (2006), p. 281. DOI: `10.1126/science.1131871` (cit. on pp. 18, 50, 54).

[50] Nan Zhao et al. "Sensing single remote nuclear spins". In: *Nature Nanotechnology* 7.10 (2012), pp. 657–662. DOI: `10.1038/nnano.2012.152` (cit. on pp. 18, 50, 52, 64).

[51] Shimon Kolkowitz et al. "Sensing Distant Nuclear Spins with a Single Electron Spin". In: *Physical Review Letters* 109.13 (2012), p. 137601. DOI: `10.1103/PhysRevLett.109.137601` (cit. on p. 18).

[52] T. H. Taminiau et al. "Detection and Control of Individual Nuclear Spins Using a Weakly Coupled Electron Spin". In: *Physical Review Letters* 109.13 (2012), p. 137602. DOI: `10.1103/PhysRevLett.109.137602` (cit. on p. 18).

[53] M. H. Abobeih et al. "One-second coherence for a single electron spin coupled to a multi-qubit nuclear-spin environment". In: *Nature Communications* 9.1 (2018), p. 2552. DOI: `10.1038/s41467-018-04916-z` (cit. on p. 18).

[54] Roland Nagy et al. "High-fidelity spin and optical control of single silicon-vacancy centres in silicon carbide". In: *Nature Communications* 10.1 (2019), p. 1954. DOI: `10.1038/s41467-019-09873-9` (cit. on p. 18).

[55] Jarryd J. Pla et al. "High-fidelity readout and control of a nuclear spin qubit in silicon". In: *Nature* 496.7445 (2013), pp. 334–338. DOI: `10.1038/nature12011` (cit. on p. 18).

[56] Kangwei Xia et al. "Optical and spin properties of a single praseodymium ion in a crystal". In: *arXiv preprint arXiv:1706.08736* (2017) (cit. on p. 18).

[57] B. Car et al. "Selective Optical Addressing of Nuclear Spins through Superhyperfine Interaction in Rare-Earth Doped Solids". In: *Physical*

Review Letters 120.19 (2018), p. 197401. DOI: `10.1103/PhysRevLett.120.197401` (cit. on p. 18).

[58] Manjin Zhong, Rose L. Ahlefeldt, and Matthew J. Sellars. "Quantum information processing using frozen core Y3+ spins in Eu3+:Y2SiO5". In: *New Journal of Physics* 21.3 (2019), p. 033019. DOI: `10.1088/1367-2630/ab0cb7` (cit. on p. 18).

[59] C. Michel, G. Buisson, and E. F. Bertaut. "Structure de Y2SiO5". In: *C.r.hebd.Seanc.Acad.Sci.,Paris* 264.5 (1967), p. 397 (cit. on p. 19).

[60] B. A. Maksimov et al. "Crystal structure of yttrium oxyorthosilicate Y2O3, SiO2 and Y2SiO5". In: *Kristallografiya* 15 (1970), pp. 926–933 (cit. on p. 19).

[61] N. I. Leonyuk et al. "High-temperature crystallization and X-ray characterization of Y2SiO5, Y2Si2O7 and LaBSiO5". In: *Journal of Crystal Growth* 205.3 (1999), pp. 361–367. DOI: `10.1016/S0022-0248(99)00233-X` (cit. on p. 19).

[62] W. Y. Ching, Lizhi Ouyang, and Yong-Nian Xu. "Electronic and optical properties of Y2SiO5 and Y2Si2O7 with comparisons to a-SiO2 and Y2O3". In: *Physical Review B* 67.24 (2003), p. 245108. DOI: `10.1103/PhysRevB.67.245108` (cit. on pp. 19, 20).

[63] Thomas Böttger et al. "Effects of magnetic field orientation on optical decoherence in $Er^3+:Y_2SiO_5$". In: *Physical Review B* 79.11 (2009), p. 115104. DOI: `10.1103/PhysRevB.79.115104` (cit. on p. 19).

[64] R. M. Macfarlane, R. S. Meltzer, and B. Z. Malkin. "Optical measurement of the isotope shifts and hyperfine and superhyperfine interactions of Nd in the solid state". In: *Physical Review B* 58.9 (1998), pp. 5692–5700. DOI: `10.1103/PhysRevB.58.5692` (cit. on p. 19).

[65] Chemistry Table (cit. on p. 20).

[66] L. Pidol et al. "EPR study of Ce3+ ions in lutetium silicate scintillators Lu2Si2O7 and Lu2SiO5". In: *Journal of Physics and Chemistry of Solids* 67.4 (2006), pp. 643–650. DOI: `10.1016/j.jpcs.2005.10.175` (cit. on pp. 21, 22, 39, 50).

[67] T. Gustafsson et al. "Lu2SiO5 by single-crystal X-ray and neutron diffraction". In: *Acta Crystallographica Section C* 57.6 (2001), pp. 668–669. DOI: 10.1107/S0108270101005352 (cit. on p. 21).

[68] Winicjusz Drozdowski et al. "VUV spectroscopy and low temperature thermoluminescence of LSO:Ce and YSO:Ce". In: *Journal of Alloys and Compounds* 380.1 (2004), pp. 146–150. DOI: 10.1016/j.jallcom.2004.03.016 (cit. on pp. 21, 22).

[69] Hai Yan et al. "Integrated optical add-drop multiplexer based on a compact parent-sub microring-resonator structure". In: *Optics Communications* 289 (2013), pp. 53–59. DOI: 10.1016/j.optcom.2012.09.059 (cit. on pp. 22, 23, 104).

[70] D. W. Cooke et al. "Luminescent properties and reduced dimensional behavior of hydrothermally prepared Y2SiO5:Ce nanophosphors". In: *Applied Physics Letters* 88.10 (2006), p. 103108. DOI: 10.1063/1.2183737 (cit. on p. 24).

[71] Valéry Zwiller and Gunnar Björk. "Improved light extraction from emitters in high refractive index materials using solid immersion lenses". In: *Journal of Applied Physics* 92.2 (2002), pp. 660–665. DOI: 10.1063/1.1487913 (cit. on p. 29).

[72] P. Siyushev et al. "Monolithic diamond optics for single photon detection". In: *Applied Physics Letters* 97.24 (2010), p. 241902. DOI: 10.1063/1.3519849 (cit. on p. 29).

[73] Mohammad Jamali et al. "Microscopic diamond solid-immersion-lenses fabricated around single defect centers by focused ion beam milling". In: *Review of Scientific Instruments* 85.12 (2014), p. 123703. DOI: 10.1063/1.4902818 (cit. on p. 29).

[74] Matthias Widmann et al. "Coherent control of single spins in silicon carbide at room temperature". In: *Nature Materials* 14.2 (2015), pp. 164–168. DOI: 10.1038/nmat4145 (cit. on p. 29).

[75] Stefan W. Hell. "Far-Field Optical Nanoscopy". In: *Science* 316.5828 (2007), pp. 1153–1158. DOI: 10.1126/science.1137395 (cit. on p. 30).

[76] Bo Huang et al. "Three-Dimensional Super-Resolution Imaging by Stochastic Optical Reconstruction Microscopy". In: *Science* 319.5864 (2008), pp. 810–813. DOI: 10.1126/science.1153529 (cit. on p. 30).

[77] Katrin I. Willig et al. "STED microscopy reveals that synaptotagmin remains clustered after synaptic vesicle exocytosis". In: *Nature* 440.7086 (2006), pp. 935–939. DOI: 10.1038/nature04592 (cit. on p. 30).

[78] Kyu Young Han et al. "Three-Dimensional Stimulated Emission Depletion Microscopy of Nitrogen-Vacancy Centers in Diamond Using Continuous-Wave Light". In: *Nano Letters* 9.9 (2009), pp. 3323–3329. DOI: 10.1021/nl901597v (cit. on p. 30).

[79] Dominik Wildanger, Jeronimo R. Maze, and Stefan W. Hell. "Diffraction Unlimited All-Optical Recording of Electron Spin Resonances". In: *Physical Review Letters* 107.1 (2011), p. 017601. DOI: 10.1103/PhysRevLett.107.017601 (cit. on p. 30).

[80] Eva Rittweger et al. "STED microscopy reveals crystal colour centres with nanometric resolution". In: *Nature Photonics* 3.3 (2009), pp. 144–147. DOI: 10.1038/nphoton.2009.2 (cit. on p. 30).

[81] Jean-Christophe Jaskula et al. "Superresolution optical magnetic imaging and spectroscopy using individual electronic spins in diamond". In: *Optics Express* 25.10 (2017), pp. 11048–11064. DOI: 10.1364/OE.25.011048 (cit. on p. 30).

[82] Stefan W. Hell. "Toward fluorescence nanoscopy". In: *Nature Biotechnology* 21.11 (2003), pp. 1347–1355. DOI: 10.1038/nbt895 (cit. on p. 31).

[83] Volker Westphal and Stefan W. Hell. "Nanoscale Resolution in the Focal Plane of an Optical Microscope". In: *Physical Review Letters* 94.14 (2005), p. 143903. DOI: 10.1103/PhysRevLett.94.143903 (cit. on p. 31).

[84] R. Kolesov et al. "Superresolution Microscopy of Single Rare-Earth Emitters in YAG and *H*3 Centers in Diamond". In: *Physical Review Letters* 120.3 (2018), p. 033903. DOI: 10.1103/PhysRevLett.120.033903 (cit. on pp. 31, 34, 91).

[85] Lixin Ning et al. "Electronic properties and 4f→ 5d transitions in Ce-doped Lu2SiO5: a theoretical investigation". In: *Journal of Materials Chemistry* 22.27 (2012), pp. 13723–13731 (cit. on p. 36).

[86] Peter A. Tanner et al. "Soft synthesis and vacuum ultraviolet spectra of YAG:Ce3+nanocrystals: reassignment of Ce3+energy levels". In: *Journal of Physics: Condensed Matter* 19.21 (2007), p. 216213. DOI: 10.1088/0953-8984/19/21/216213 (cit. on p. 35).

[87] Arthur Schweiger and Gunnar Jeschke. *Principles of pulse electron paramagnetic resonance*. Reprinted. Oxford: Oxford Univ. Press, 2005. ISBN: 0198506341 (cit. on pp. 39, 40, 54).

[88] R. Hanson, O. Gywat, and D. D. Awschalom. "Room-temperature manipulation and decoherence of a single spin in diamond". In: *Physical Review B* 74.16 (2006), p. 161203. DOI: 10.1103/PhysRevB.74.161203 (cit. on p. 44).

[89] V. V. Dobrovitski et al. "Decay of Rabi Oscillations by Dipolar-Coupled Dynamical Spin Environments". In: *Physical Review Letters* 102.23 (2009), p. 237601. DOI: 10.1103/PhysRevLett.102.237601 (cit. on p. 44).

[90] A. Dréau et al. "Avoiding power broadening in optically detected magnetic resonance of single NV defects for enhanced dc magnetic field sensitivity". In: *Physical Review B* 84.19 (2011), p. 195204. DOI: 10.1103/PhysRevB.84.195204 (cit. on p. 46).

[91] Jonas Bylander et al. "Noise spectroscopy through dynamical decoupling with a superconducting flux qubit". In: *Nature Physics* 7.7 (2011), pp. 565–570. DOI: 10.1038/nphys1994 (cit. on p. 46).

[92] I. N. Kurkin and K. P. Chernov. "EPR and spin-lattice relaxation of rare-earth activated centres in Y2SiO5 single crystals". In: *Physica B+C* 101.2 (1980), pp. 233–238. DOI: 10.1016/0378-4363(80)90107-2 (cit. on p. 48).

[93] Jun Wen et al. "Spectroscopic Distinctions between Two Types of Ce3+ Ions in X2-Y2SiO5: A Theoretical Investigation". In: *The Journal of Physical Chemistry A* 118.27 (2014), pp. 4988–4994. DOI: 10.1021/jp5050207 (cit. on p. 50).

[94]   Wen Yang and Ren-Bao Liu. "Quantum many-body theory of qubit decoherence in a finite-size spin bath. II. Ensemble dynamics". In: *Physical Review B* 79.11 (2009), p. 115320. DOI: 10.1103/PhysRevB.79.115320 (cit. on p. 52).

[95]   A. Szabo. "Spin dependence of optical dephasing in ruby: the frozen core". In: *Optics Letters* 8.9 (1983), pp. 486–487. DOI: 10.1364/OL.8.000486 (cit. on pp. 54, 64).

[96]   Nan Zhao et al. "Atomic-scale magnetometry of distant nuclear spin clusters via nitrogen-vacancy spin in diamond". In: *Nature Nanotechnology* 6.4 (2011), pp. 242–246. DOI: 10.1038/nnano.2011.22 (cit. on p. 59).

[97]   Łukasz Cywiński et al. "How to enhance dephasing time in superconducting qubits". In: *Physical Review B* 77.17 (2008), p. 174509. DOI: 10.1103/PhysRevB.77.174509 (cit. on p. 59).

[98]   Ping Wang and Wen Yang. "Theory of nuclear spin dephasing and relaxation by optically illuminated nitrogen-vacancy center". In: *New Journal of Physics* 17.11 (2015), p. 113041. DOI: 10.1088/1367-2630/17/11/113041 (cit. on pp. 61, 62).

[99]   G. Lindblad. "On the generators of quantum dynamical semigroups". In: *Communications in Mathematical Physics* 48.2 (1976), pp. 119–130. DOI: 10.1007/BF01608499 (cit. on p. 62).

[100] Heinz-Peter Breuer and Francesco Petruccione. *The theory of open quantum systems*. Oxford University Press on Demand, 2002. ISBN: 0198520638 (cit. on p. 62).

[101] Wenchao Ma et al. "Resolving remote nuclear spins in a noisy bath by dynamical decoupling design". In: *Physical Review A* 92.3 (2015), p. 033418. DOI: 10.1103/PhysRevA.92.033418 (cit. on p. 64).

[102] P. London et al. "Detecting and Polarizing Nuclear Spins with Double Resonance on a Single Electron Spin". In: *Physical Review Letters* 111.6 (2013), p. 067601. DOI: 10.1103/PhysRevLett.111.067601 (cit. on p. 64).

[103]   Jarryd J. Pla et al. "A single-atom electron spin qubit in silicon". In: *Nature* 489.7417 (2012), pp. 541–545. DOI: `10.1038/nature11449` (cit. on p. 66).

[104]   Matthias Koch et al. "Spin read-out in atomic qubits in an all-epitaxial three-dimensional transistor". In: *Nature Nanotechnology* 14.2 (2019), pp. 137–140. DOI: `10.1038/s41565-018-0338-1` (cit. on p. 66).

[105]   M. Veldhorst et al. "A two-qubit logic gate in silicon". In: *Nature* 526.7573 (2015), pp. 410–414. DOI: `10.1038/nature15263` (cit. on p. 66).

[106]   M. A. Broome et al. "Two-electron spin correlations in precision placed donors in silicon". In: *Nature Communications* 9.1 (2018), p. 980. DOI: `10.1038/s41467-018-02982-x` (cit. on p. 66).

[107]   A. Gruber et al. "Scanning Confocal Optical Microscopy and Magnetic Resonance on Single Defect Centers". In: *Science* 276.5321 (1997), pp. 2012–2014. DOI: `10.1126/science.276.5321.2012` (cit. on pp. 66, 73).

[108]   Lachlan J. Rogers et al. "All-Optical Initialization, Readout, and Coherent Preparation of Single Silicon-Vacancy Spins in Diamond". In: *Physical Review Letters* 113.26 (2014), p. 263602. DOI: `10.1103/PhysRevLett.113.263602` (cit. on pp. 66, 73).

[109]   Dirk Englund et al. "Deterministic Coupling of a Single Nitrogen Vacancy Center to a Photonic Crystal Cavity". In: *Nano Letters* 10.10 (2010), pp. 3922–3926. DOI: `10.1021/nl101662v` (cit. on p. 66).

[110]   Sara Marzban et al. "Observation of Photon Echoes From Evanescently Coupled Rare-Earth Ions in a Planar Waveguide". In: *Physical Review Letters* 115.1 (2015), p. 013601. DOI: `10.1103/PhysRevLett.115.013601` (cit. on pp. 66, 108).

[111]   Thomas Kornher et al. "Amorphous Silicon-Doped Titania Films for on-Chip Photonics". In: *ACS Photonics* 4.5 (2017), pp. 1101–1107. DOI: `10.1021/acsphotonics.6b00919` (cit. on pp. 66, 91).

[112]   M.-A. Lemonde et al. "Phonon Networks with Silicon-Vacancy Centers in Diamond Waveguides". In: *Physical Review Letters* 120.21 (2018), p. 213603. DOI: `10.1103/PhysRevLett.120.213603` (cit. on p. 66).

[113] Frank J. Rueß et al. "Realization of Atomically Controlled Dopant Devices in Silicon". In: *Small* 3.4 (2007), pp. 563–567. DOI: `10.1002/smll.200600680` (cit. on p. 66).

[114] Jessica van Donkelaar et al. "Single atom devices by ion implantation". In: *Journal of Physics: Condensed Matter* 27.15 (2015), p. 154204. DOI: `10.1088/0953-8984/27/15/154204` (cit. on p. 66).

[115] Georg Jacob et al. "Transmission Microscopy with Nanometer Resolution Using a Deterministic Single Ion Source". In: *Physical Review Letters* 117.4 (2016), p. 043001. DOI: `10.1103/PhysRevLett.117.043001` (cit. on pp. 67, 69–71).

[116] Karin Groot-Berning et al. "Deterministic Single-Ion Implantation of Rare-Earth Ions for Nanometer-Resolution Color-Center Generation". In: *Physical Review Letters* 123.10 (2019), p. 106802. DOI: `10.1103/PhysRevLett.123.106802` (cit. on p. 67).

[117] Georg Jacob. "Ion implantation and transmission microscopy with nanometer resolution using a deterministic ion source". PhD thesis. 2017 (cit. on p. 67).

[118] Wolfgang Paul and Helmut Steinwedel. "Notizen: Ein neues Massenspektrometer ohne Magnetfeld". In: *Zeitschrift für Naturforschung A* 8.7 (1953), pp. 448–450. DOI: `10.1515/zna-1953-0710` (cit. on p. 68).

[119] J. Meijer et al. "Concept of deterministic single ion doping with sub-nm spatial resolution". In: *Applied Physics A* 83.2 (2006), pp. 321–327. DOI: `10.1007/s00339-006-3497-0` (cit. on p. 68).

[120] W. Schnitzler et al. "Deterministic Ultracold Ion Source Targeting the Heisenberg Limit". In: *Physical Review Letters* 102.7 (2009), p. 070501. DOI: `10.1103/PhysRevLett.102.070501` (cit. on p. 68).

[121] Jannes B. Wübbena et al. "Sympathetic cooling of mixed-species two-ion crystals for precision spectroscopy". In: *Physical Review A* 85.4 (2012), p. 043412. DOI: `10.1103/PhysRevA.85.043412` (cit. on p. 71).

[122] James F. Ziegler, M. D. Ziegler, and J. P. Biersack. "SRIM – The stopping and range of ions in matter (2010)". In: *Nuclear Instruments and Methods in Physics Research Section B: Beam Interactions with Materials*

and Atoms 268.11 (2010), pp. 1818–1823. DOI: `10.1016/j.nimb.2010.02.091` (cit. on pp. 72, 85, 91, 122, 125, 128, 132, 139, 142, 143).

[123] S. K. Gayen, Bin Qing Xie, and Y. M. Cheung. "Two-photon excitation of the lowest 4f2-4f5d near-ultraviolet transitions in Pr3+:Y3Al5O12". In: *Physical Review B* 45.1 (1992), pp. 20–28. DOI: `10.1103/PhysRevB.45.20` (cit. on p. 73).

[124] F. Auzel. "Upconversion processes in coupled ion systems". In: *Journal of Luminescence* 45.1 (1990), pp. 341–345. DOI: `10.1016/0022-2313(90)90189-I` (cit. on p. 73).

[125] M. Nakielska et al. "Up-conversion and fluorescence quenching processes studies in highly Pr3+-doped YAG waveguides". In: *Journal of Alloys and Compounds* 451.1 (2008), pp. 190–193. DOI: `10.1016/j.jallcom.2007.04.174` (cit. on p. 73).

[126] John B. Gruber et al. "Symmetry, selection rules, and energy levels of Pr3+:Y3Al5O12". In: *Chemical Physics* 134.2 (1989), pp. 241–257. DOI: `10.1016/0301-0104(89)87159-9` (cit. on pp. 74, 77, 78).

[127] Joseph Ganem, W. M. Dennis, and W. M. Yen. "One-color sequential pumping of the 4f5d bands in Pr-doped yttrium aluminum garnet". In: *Journal of Luminescence* 54.2 (1992), pp. 79–87. DOI: `10.1016/0022-2313(92)90250-D` (cit. on p. 74).

[128] M. J. Weber. "Nonradiative decay from 5d states of rare earths in crystals". In: *Solid State Communications* 12.7 (1973), pp. 741–744. DOI: `10.1016/0038-1098(73)90326-8` (cit. on p. 74).

[129] van der Ziel, J. P., M. D. Sturge, and L. G. van Uitert. "Optical Detection of Site Selectivity for Rare-Earth Ions in Flux-Grown Yttrium Aluminum Garnet". In: *Physical Review Letters* 27.8 (1971), pp. 508–511. DOI: `10.1103/PhysRevLett.27.508` (cit. on pp. 76, 77).

[130] J. F. Dillon and L. R. Walker. "Ferrimagnetic Resonance in Rare-Earth Doped Yttrium Iron Garnet. II. Terbium Substitution". In: *Physical Review* 124.5 (1961), pp. 1401–1413. DOI: `10.1103/PhysRev.124.1401` (cit. on p. 77).

[131] F. N. Hooge. "Spectra of Praseodymium in Yttrium Gallium Garnet and in Yttrium Aluminum Garnet". In: *The Journal of Chemical Physics* 45.12 (1966), pp. 4504–4509. DOI: 10.1063/1.1727530 (cit. on p. 78).

[132] J. R. Rabeau et al. "Implantation of labelled single nitrogen vacancy centers in diamond using N15". In: *Applied Physics Letters* 88.2 (2006), p. 023113. DOI: 10.1063/1.2158700 (cit. on p. 83).

[133] Boris Naydenov et al. "Enhanced generation of single optically active spins in diamond by ion implantation". In: *Applied Physics Letters* 96.16 (2010), p. 163108. DOI: 10.1063/1.3409221 (cit. on p. 83).

[134] Tim Schröder et al. "Scalable focused ion beam creation of nearly lifetime-limited single quantum emitters in diamond nanostructures". In: *Nature Communications* 8.1 (2017), p. 15376. DOI: 10.1038/ncomms15376 (cit. on p. 84).

[135] D. J. Cherniak. "Rare earth element and gallium diffusion in yttrium aluminum garnet". In: *Physics and Chemistry of Minerals* 26.2 (1998), pp. 156–163 (cit. on p. 85).

[136] Athanasios Papoulis and S. Unnikrishna Pillai. *Probability, random variables, and stochastic processes*. Tata McGraw-Hill Education, 2002. ISBN: 0070486581 (cit. on p. 87).

[137] Guilherme Tosi et al. "Silicon quantum processor with robust long-distance qubit couplings". In: *Nature Communications* 8.1 (2017), p. 450. DOI: 10.1038/s41467-017-00378-x (cit. on p. 90).

[138] J. Perczel et al. "Topological Quantum Optics in Two-Dimensional Atomic Arrays". In: *Physical Review Letters* 119.2 (2017), p. 023603. DOI: 10.1103/PhysRevLett.119.023603 (cit. on p. 91).

[139] P. Haikka et al. "Proposal for detecting a single electron spin in a microwave resonator". In: *Physical Review A* 95.2 (2017), p. 022306. DOI: 10.1103/PhysRevA.95.022306 (cit. on p. 91).

[140] B. E. Kane. "A silicon-based nuclear spin quantum computer". In: *Nature* 393.6681 (1998), pp. 133–137. DOI: 10.1038/30156 (cit. on p. 91).

[141] Daniel A. Steck. *Quantum and atom optics*. 2007 (cit. on p. 94).

[142]   Edward Mills Purcell. "Spontaneous transition probabilities in radio-frequency spectroscopy". In: *Phys. Rev* 69 (1946), p. 681 (cit. on p. 97).

[143]   Ja Hyon Ku. "JW Strutt, third Baron Rayleigh, The theory of sound, (1877–1878)". In: *Landmark Writings in Western Mathematics 1640-1940*. Elsevier, 2005, pp. 588–599 (cit. on p. 98).

[144]   Anatolii N. Oraevsky. "Whispering-gallery waves". In: *Quantum Electronics* 32.5 (2002), pp. 377–400. DOI: `10.1070/qe2002v032n05abeh002205` (cit. on p. 98).

[145]   Tobias Jan August Kippenberg. "Nonlinear optics in ultra-high Q whispering-gallery optical microcavities". PhD thesis. California Institute of Technology, 2004 (cit. on p. 98).

[146]   John Heebner et al. *Optical microresonators: theory, fabrication, and applications*. Springer Science & Business Media, 2008. ISBN: 0387730672 (cit. on p. 98).

[147]   J. Sarma and K.A. Shore. "Electromagnetic theory for optical disc resonators". In: *IEE Proceedings J (Optoelectronics)* 132.6 (December 1985), pp. 325–330 (cit. on p. 99).

[148]   Jerome Degallaix et al. "Bulk optical absorption of high resistivity silicon at 1550 nm". In: *Optics Letters* 38.12 (2013), pp. 2047–2049. DOI: `10.1364/OL.38.002047` (cit. on p. 101).

[149]   H. Tang et al. "Electrical and optical properties of TiO2 anatase thin films". In: *Journal of Applied Physics* 75.4 (1994), pp. 2042–2047. DOI: `10.1063/1.356306` (cit. on pp. 101, 108, 109).

[150]   Jonathan D. B. Bradley et al. "Submicrometer-wide amorphous and polycrystalline anatase TiO2 waveguides for microphotonic devices". In: *Optics Express* 20.21 (2012), pp. 23821–23831. DOI: `10.1364/OE.20.023821` (cit. on pp. 101, 108, 109, 117).

[151]   Tapani Alasaarela et al. "High-quality crystallinity controlled ALD TiO2 for waveguiding applications". In: *Optics Letters* 38.20 (2013), pp. 3980–3983. DOI: `10.1364/OL.38.003980` (cit. on pp. 101, 108, 109).

[152] P. K. Tien. "Light Waves in Thin Films and Integrated Optics". In: *Applied Optics* 10.11 (1971), pp. 2395–2413. DOI: 10.1364/AO.10.002395 (cit. on p. 101).

[153] V. B. Braginsky, M. L. Gorodetsky, and V. S. Ilchenko. "Quality-factor and nonlinear properties of optical whispering-gallery modes". In: *Physics Letters A* 137.7 (1989), pp. 393–397. DOI: 10.1016/0375-9601(89)90912-2 (cit. on p. 101).

[154] K. Winkler et al. "High quality factor GaAs microcavity with buried bullseye defects". In: *Physical Review Materials* 2.5 (2018), p. 052201. DOI: 10.1103/PhysRevMaterials.2.052201 (cit. on p. 103).

[155] Kerry J. Vahala. "Optical microcavities". In: *Nature* 424.6950 (2003), pp. 839–846. DOI: 10.1038/nature01939 (cit. on p. 103).

[156] Charles Santori et al. "Indistinguishable photons from a single-photon device". In: *Nature* 419.6907 (2002), pp. 594–597. DOI: 10.1038/nature01086 (cit. on p. 103).

[157] J. P. Reithmaier et al. "Strong coupling in a single quantum dot–semiconductor microcavity system". In: *Nature* 432.7014 (2004), pp. 197–200. DOI: 10.1038/nature02969 (cit. on p. 103).

[158] Shunfa Liu et al. "A deterministic quantum dot micropillar single photon source with >65% extraction efficiency based on fluorescence imaging method". In: *Scientific Reports* 7.1 (2017), p. 13986. DOI: 10.1038/s41598-017-13433-w (cit. on p. 103).

[159] O. Painter, J. Vučković, and A. Scherer. "Defect modes of a two-dimensional photonic crystal in an optically thin dielectric slab". In: *Journal of the Optical Society of America B* 16.2 (1999), pp. 275–285. DOI: 10.1364/JOSAB.16.000275 (cit. on p. 103).

[160] Jelena Vučković et al. "Design of photonic crystal microcavities for cavity QED". In: *Physical Review E* 65.1 (2001), p. 016608. DOI: 10.1103/PhysRevE.65.016608 (cit. on p. 103).

[161]   Andrei Faraon et al. "Coupling of Nitrogen-Vacancy Centers to Photonic Crystal Cavities in Monocrystalline Diamond". In: *Physical Review Letters* 109.3 (2012), p. 033604. DOI: 10.1103/PhysRevLett.109.033604 (cit. on p. 104).

[162]   B. J. M. Hausmann et al. "Coupling of NV Centers to Photonic Crystal Nanobeams in Diamond". In: *Nano Letters* 13.12 (2013), pp. 5791–5796. DOI: 10.1021/nl402174g (cit. on p. 104).

[163]   David O. Bracher, Xingyu Zhang, and Evelyn L. Hu. "Selective Purcell enhancement of two closely linked zero-phonon transitions of a silicon carbide color center". In: *Proceedings of the National Academy of Sciences* 114.16 (2017), pp. 4060–4065. DOI: 10.1073/pnas.1704219114 (cit. on p. 104).

[164]   Bong-Shik Song et al. "High-Q-factor nanobeam photonic crystal cavities in bulk silicon carbide". In: *Applied Physics Letters* 113.23 (2018), p. 231106. DOI: 10.1063/1.5058194 (cit. on p. 104).

[165]   Daniil M. Lukin et al. "4H-silicon-carbide-on-insulator for integrated quantum and nonlinear photonics". In: *Nature Photonics* (2019). DOI: 10.1038/s41566-019-0556-6 (cit. on p. 104).

[166]   A. Vorckel et al. "Asymmetrically coupled silicon-on-insulator microring resonators for compact add-drop multiplexers". In: *IEEE Photonics Technology Letters* 15.7 (2003), pp. 921–923. DOI: 10.1109/LPT.2003.813419 (cit. on p. 104).

[167]   Miloš A. Popovíc et al. "Multistage high-order microring-resonator add-drop filters". In: *Optics Letters* 31.17 (2006), pp. 2571–2573. DOI: 10.1364/OL.31.002571 (cit. on p. 104).

[168]   S. Xiao et al. "Silicon-on-Insulator Microring Add-Drop Filters With Free Spectral Ranges Over 30 nm". In: *Journal of Lightwave Technology* 26.2 (2008), pp. 228–236. DOI: 10.1109/JLT.2007.911098 (cit. on p. 104).

[169]   Shuichi Suzuki et al. "Precise Control of Wavelength Channel Spacing of Microring Resonator Add-Drop Filter Array". In: *Journal of Lightwave Technology* 20.4 (2002), p. 745 (cit. on p. 104).

[170] Danning Wu et al. "Four-channel optical add-drop multiplexer based on dual racetrack micro-ring resonators". In: *Optics Communications* 354 (2015), pp. 386–391. DOI: `10.1016/j.optcom.2015.06.028` (cit. on p. 104).

[171] Linjie Zhou and Andrew W. Poon. "Fano resonance-based electrically reconfigurable add-drop filters in silicon microring resonator-coupled Mach-Zehnder interferometers". In: *Optics Letters* 32.7 (2007), pp. 781–783. DOI: `10.1364/OL.32.000781` (cit. on p. 104).

[172] Amy C. Turner et al. "Ultra-low power parametric frequency conversion in a silicon microring resonator". In: *Optics Express* 16.7 (2008), pp. 4881–4887. DOI: `10.1364/OE.16.004881` (cit. on p. 104).

[173] David J. Moss et al. "New CMOS-compatible platforms based on silicon nitride and Hydex for nonlinear optics". In: *Nature Photonics* 7.8 (2013), pp. 597–607. DOI: `10.1038/nphoton.2013.183` (cit. on p. 104).

[174] B. J. M. Hausmann et al. "Diamond nonlinear photonics". In: *Nature Photonics* 8.5 (2014), pp. 369–374. DOI: `10.1038/nphoton.2014.72` (cit. on p. 104).

[175] Cheng Wang et al. "Monolithic lithium niobate photonic circuits for Kerr frequency comb generation and modulation". In: *Nature Communications* 10.1 (2019), p. 978. DOI: `10.1038/s41467-019-08969-6` (cit. on p. 104).

[176] S. M. Spillane et al. "Ultrahigh-Q toroidal microresonators for cavity quantum electrodynamics". In: *Physical Review A* 71.1 (2005), p. 013817. DOI: `10.1103/PhysRevA.71.013817` (cit. on p. 104).

[177] Pawel Latawiec et al. "Integrated diamond Raman laser pumped in the near-visible". In: *Optics Letters* 43.2 (2018), pp. 318–321. DOI: `10.1364/OL.43.000318` (cit. on pp. 104, 108).

[178] Carlos Angulo Barrios. "Integrated microring resonator sensor arrays for labs-on-chips". In: *Analytical and Bioanalytical Chemistry* 403.6 (2012), pp. 1467–1475. DOI: `10.1007/s00216-012-5937-3` (cit. on p. 104).

[179]   Qing Li, Marcelo Davanço, and Kartik Srinivasan. "Efficient and low-noise single-photon-level frequency conversion interfaces using silicon nanophotonics". In: *Nature Photonics* 10.6 (2016), pp. 406–414. DOI: 10.1038/nphoton.2016.64 (cit. on p. 104).

[180]   Andrei Faraon et al. "Resonant enhancement of the zero-phonon emission from a colour centre in a diamond cavity". In: *Nature Photonics* 5.5 (2011), pp. 301–305. DOI: 10.1038/nphoton.2011.52 (cit. on p. 104).

[181]   Dapeng Ding et al. "Multidimensional Purcell effect in an ytterbium-doped ring resonator". In: *Nature Photonics* 10.6 (2016), pp. 385–388. DOI: 10.1038/nphoton.2016.72 (cit. on pp. 104, 105, 142).

[182]   T. Yoshie et al. "Vacuum Rabi splitting with a single quantum dot in a photonic crystal nanocavity". In: *Nature* 432.7014 (2004), pp. 200–203. DOI: 10.1038/nature03119 (cit. on p. 104).

[183]   Tian Zhong et al. "Nanophotonic rare-earth quantum memory with optically controlled retrieval". In: *Science* 357.6358 (2017), p. 1392. DOI: 10.1126/science.aan5959 (cit. on p. 104).

[184]   A. E. Shitikov et al. "Billion Q-factor in silicon WGM resonators". In: *Optica* 5.12 (2018), pp. 1525–1528. DOI: 10.1364/OPTICA.5.001525 (cit. on p. 105).

[185]   Chi Xiong et al. "Aluminum nitride as a new material for chip-scale optomechanics and nonlinear optics". In: *New Journal of Physics* 14.9 (2012), p. 095014. DOI: 10.1088/1367-2630/14/9/095014 (cit. on p. 108).

[186]   Patrik Rath et al. "Diamond as a material for monolithically integrated optical and optomechanical devices". In: *physica status solidi (a)* 212.11 (2015), pp. 2385–2399. DOI: 10.1002/pssa.201532494 (cit. on p. 108).

[187]   Luozhou Li et al. "One-dimensional photonic crystal cavities in single-crystal diamond". In: *Photonics and Nanostructures - Fundamentals and Applications* 15 (2015), pp. 130–136. DOI: 10.1016/j.photonics.2015.03.002 (cit. on p. 108).

[188] Michael J. Burek et al. "High quality-factor optical nanocavities in bulk single-crystal diamond". In: *Nature Communications* 5.1 (2014), p. 5718. DOI: 10.1038/ncomms6718 (cit. on p. 108).

[189] Mughees Khan et al. "Fabrication and characterization of high-quality-factor silicon nitride nanobeam cavities". In: *Optics Letters* 36.3 (2011), pp. 421–423. DOI: 10.1364/OL.36.000421 (cit. on p. 108).

[190] Ehsan Shah Hosseini et al. "High Quality Planar Silicon Nitride Microdisk Resonators for Integrated Photonics in the VisibleWavelength Range". In: *Optics Express* 17.17 (2009), pp. 14543–14551. DOI: 10.1364/OE.17.014543 (cit. on p. 108).

[191] Christopher C. Evans, Chengyu Liu, and Jin Suntivich. "Low-loss titanium dioxide waveguides and resonators using a dielectric lift-off fabrication process". In: *Optics Express* 23.9 (2015), pp. 11160–11169. DOI: 10.1364/OE.23.011160 (cit. on pp. 108, 109, 117).

[192] Junsoo Park et al. "Titanium Dioxide Whispering Gallery Microcavities". In: *Advanced Optical Materials* 2.8 (2014), pp. 711–717. DOI: 10.1002/adom.201400107 (cit. on pp. 108, 109).

[193] M. Häyrinen et al. "Low-Loss Titanium Dioxide Strip Waveguides Fabricated by Atomic Layer Deposition". In: *Journal of Lightwave Technology* 32.2 (2014), pp. 208–212. DOI: 10.1109/JLT.2013.2291960 (cit. on pp. 108, 109, 117).

[194] Jennifer T. Choy et al. "Integrated TiO2 resonators for visible photonics". In: *Optics Letters* 37.4 (2012), pp. 539–541. DOI: 10.1364/OL.37.000539 (cit. on pp. 108, 109).

[195] Yiyang Gong and Jelena Vučković. "Photonic crystal cavities in silicon dioxide". In: *Applied Physics Letters* 96.3 (2010), p. 031107. DOI: 10.1063/1.3297877 (cit. on p. 108).

[196] Seung Hoon Lee et al. "Towards visible soliton microcomb generation". In: *Nature Communications* 8.1 (2017), p. 1295. DOI: 10.1038/s41467-017-01473-9 (cit. on p. 108).

[197]   Koichi Abe et al., eds. *Nonlinear optical waveguides with rutile TiO2*.
        Vol. 7940. 4560. URL: https://doi.org/10.1117/12.874560 (cit. on
        pp. 109, 117).

[198]   Xiaowei Guan et al. "Compact titanium dioxide waveguides with
        high nonlinearity at telecommunication wavelengths". In: *Optics Ex-
        press* 26.2 (2018), pp. 1055–1063. DOI: 10.1364/OE.26.001055 (cit. on
        pp. 109, 117).

[199]   P. Karasiński et al. "Optical rib waveguides based on sol-gel derived
        silica–titania films". In: *Thin Solid Films* 519.16 (2011), pp. 5544–5551.
        DOI: 10.1016/j.tsf.2011.02.064 (cit. on p. 109).

[200]   Estelle Wagner et al. "Geometry of Chemical Beam Vapor Deposi-
        tion System for Efficient Combinatorial Investigations of Thin Ox-
        ide Films: Deposited Film Properties versus Precursor Flow Simu-
        lations". In: *ACS Combinatorial Science* 18.3 (2016), pp. 154–161. DOI:
        10.1021/acscombsci.5b00146 (cit. on pp. 109, 152).

[201]   Si-Moo Lee et al. "The deposition behavior of SiO2–TiO2 thin film by
        metalorganic chemical vapor deposition method". In: *Journal of Vac-
        uum Science & Technology A* 18.5 (2000), pp. 2384–2388. DOI: 10.1116/
        1.1287154 (cit. on p. 109).

[202]   J. R. DeVore. "Refractive Indices of Rutile and Sphalerite". In: *Journal
        of the Optical Society of America* 41.6 (1951), pp. 416–419. DOI: 10.1364/
        JOSA.41.000416 (cit. on p. 110).

[203]   Kyung-Rok Choi et al. "Dry etching properties of TiO2 thin films in
        O2/CF4/Ar plasma". In: *Vacuum* 92 (2013), pp. 85–89. DOI: 10.1016/
        j.vacuum.2012.11.009 (cit. on p. 111).

[204]   Nicolas Martin et al. "Microstructure modification of amorphous ti-
        tanium oxide thin films during annealing treatment". In: *Thin Solid
        Films* 300.1 (1997), pp. 113–121. DOI: 10.1016/S0040-6090(96)09510-
        7 (cit. on p. 112).

[205]   Roman Kolesov et al. "Wave–particle duality of single surface plas-
        mon polaritons". In: *Nature Physics* 5.7 (2009), pp. 470–474. DOI: 10.
        1038/nphys1278 (cit. on p. 114).

[206] Shanhui Fan. "Sharp asymmetric line shapes in side-coupled waveguide-cavity systems". In: *Applied Physics Letters* 80.6 (2002), pp. 908–910. DOI: 10.1063/1.1448174 (cit. on p. 115).

[207] D. J. Robbins. "The effects of crystal field and temperature on the photoluminescence excitation efficiency of Ce3+ in YAG". In: *Journal of the electrochemical society* 126.9 (1979), pp. 1550–1555 (cit. on p. 126).

[208] A. Bahtat et al. "Up-conversion fluorescence spectroscopy in Er3+: TiO2 planar waveguides prepared by a sol-gel process". In: *Journal of Non-Crystalline Solids* 202.1 (1996), pp. 16–22. DOI: 10.1016/0022-3093(96)00172-X (cit. on p. 128).

[209] Hoi van Pham et al. "Coherent emission at 537 nm from IR-pumped erbium-doped silica microspheres". In: *Optics Letters* 39.4 (2014), pp. 907–909. DOI: 10.1364/ol.39.000907 (cit. on p. 128).

[210] S. Obregón et al. "High-performance Er3+–TiO2 system: Dual upconversion and electronic role of the lanthanide". In: *Journal of Catalysis* 299 (2013), pp. 298–306. DOI: 10.1016/j.jcat.2012.12.021 (cit. on p. 128).

[211] Sabrina R. Johannsen et al. "Up-conversion enhancement in Er3+ doped TiO2 through plasmonic coupling: Experiments and finite-element modeling". In: *Applied Physics Letters* 106.5 (2015), p. 053101. DOI: 10.1063/1.4907415 (cit. on p. 128).

[212] Fiorenzo Vetrone et al. "980 nm excited upconversion in an Er-doped ZnO–TeO2 glass". In: *Applied Physics Letters* 80.10 (2002), pp. 1752–1754. DOI: 10.1063/1.1458073 (cit. on p. 129).

[213] Feng Song et al. "Three-photon phenomena in the upconversion luminescence of erbium–ytterbium-codoped phosphate glass". In: *Applied Physics Letters* 79.12 (2001), pp. 1748–1750. DOI: 10.1063/1.1404996 (cit. on p. 129).

[214] Mian Zhang et al. "Broadband electro-optic frequency comb generation in a lithium niobate microring resonator". In: *Nature* 568.7752 (2019), pp. 373–377. DOI: 10.1038/s41586-019-1008-7 (cit. on p. 130).

[215]   Mian Zhang et al. "Electronically programmable photonic molecule". In: *Nature Photonics* 13.1 (2019), pp. 36–40. DOI: `10.1038/s41566-018-0317-y` (cit. on p. 130).

[216]   Cheng Wang et al. "Integrated lithium niobate electro-optic modulators operating at CMOS-compatible voltages". In: *Nature* 562.7725 (2018), pp. 101–104. DOI: `10.1038/s41586-018-0551-y` (cit. on p. 130).

[217]   Andrea Guarino et al. "Electro–optically tunable microring resonators in lithium niobate". In: *Nature Photonics* 1.7 (2007), pp. 407–410. DOI: `10.1038/nphoton.2007.93` (cit. on p. 130).

[218]   M. de Micheli et al. "Fabrication and characterization of Titanium Indiffused Proton Exchanged (TIPE) waveguides in lithium niobate". In: *Optics Communications* 42.2 (1982), pp. 101–103. DOI: `10.1016/0030-4018(82)90374-1` (cit. on p. 131).

[219]   Yu. N. Korkishko et al. "Reverse proton exchange for buried waveguides in LiNbO3". In: *Journal of the Optical Society of America A* 15.7 (1998), pp. 1838–1842. DOI: `10.1364/JOSAA.15.001838` (cit. on p. 131).

[220]   Rostislav V. Roussev et al. "Periodically poled lithium niobate waveguide sum-frequency generator for efficient single-photon detection at communication wavelengths". In: *Optics Letters* 29.13 (2004), pp. 1518–1520. DOI: `10.1364/OL.29.001518` (cit. on p. 131).

[221]   D. Janner et al. "Micro-structured integrated electro-optic LiNbO3 modulators". In: *Laser & Photonics Reviews* 3.3 (2009), pp. 301–313. DOI: `10.1002/lpor.200810073` (cit. on p. 131).

[222]   M. Levy et al. "Fabrication of single-crystal lithium niobate films by crystal ion slicing". In: *Applied Physics Letters* 73.16 (1998), pp. 2293–2295. DOI: `10.1063/1.121801` (cit. on p. 132).

[223]   A. M. Radojevic et al. "Large etch-selectivity enhancement in the epitaxial liftoff of single-crystal LiNbO3 films". In: *Applied Physics Letters* 74.21 (1999), pp. 3197–3199. DOI: `10.1063/1.124115` (cit. on p. 132).

[224]   Payam Rabiei and Peter Gunter. "Optical and electro-optical properties of submicrometer lithium niobate slab waveguides prepared by

crystal ion slicing and wafer bonding". In: *Applied Physics Letters* 85.20 (2004), pp. 4603–4605. DOI: 10.1063/1.1819527 (cit. on p. 132).

[225] L. Maleki and A. Matsko. "Ferroelectric crystals for photonic applications". In: *Lithium Niobate Whispering Gallery Resonators: Applications and Fundamental Studies, Book Chapter* 91 (2009), pp. 337–383 (cit. on pp. 132, 135, 137).

[226] R. S. Weis and T. K. Gaylord. "Lithium niobate: Summary of physical properties and crystal structure". In: *Applied Physics A* 37.4 (1985), pp. 191–203. DOI: 10.1007/BF00614817 (cit. on pp. 132, 137).

[227] E. Montoya, A. Lorenzo, and L. E. Bausá. "Optical characterization of crystals". In: *Journal of Physics: Condensed Matter* 11.1 (1999), pp. 311–320. DOI: 10.1088/0953-8984/11/1/026 (cit. on pp. 133, 135).

[228] Sarah Benchabane et al. "Highly selective electroplated nickel mask for lithium niobate dry etching". In: *Journal of Applied Physics* 105.9 (2009), p. 094109. DOI: 10.1063/1.3125315 (cit. on p. 134).

[229] Aurélie Lecestre et al. "Electroplated Ni mask for plasma etching of submicron-sized features in LiNbO3". In: *Microelectronic Engineering* 105 (2013), pp. 95–98. DOI: 10.1016/j.mee.2012.08.004 (cit. on p. 134).

[230] Zsolt Kis et al. "Homogeneous linewidth measurements of Yb3+ ions in congruent and stoichiometric lithium niobate crystals". In: *Optical Materials* 37 (2014), pp. 845–853. DOI: 10.1016/j.optmat.2014.09.022 (cit. on pp. 134, 140, 141).

[231] J. Garcıa Solé et al. "Rare earth and transition metal ion centers in LiNbO3". In: *Spectrochimica Acta Part A: Molecular and Biomolecular Spectroscopy* 54.11 (1998), pp. 1571–1581. DOI: 10.1016/S1386-1425(98)00084-5 (cit. on p. 134).

[232] Xiaodong Jiang et al. "Rare earth-implanted lithium niobate: Properties and on-chip integration". In: *Applied Physics Letters* 115.7 (2019), p. 071104. DOI: 10.1063/1.5098316 (cit. on pp. 134, 142).

[233] G. Ulliac et al. "Argon plasma inductively coupled plasma reactive ion etching study for smooth sidewall thin film lithium niobate waveguide application". In: *Optical Materials* 53 (2016), pp. 1–5. DOI: 10.1016/j.optmat.2015.12.040 (cit. on p. 135).

[234] Andrew J. Mercante et al. "Thin film lithium niobate electro-optic modulator with terahertz operating bandwidth". In: *Optics Express* 26.11 (2018), pp. 14810–14816. DOI: 10.1364/OE.26.014810 (cit. on p. 135).

[235] Venkatraman Gopalan and Mool C. Gupta. "Origin and characteristics of internal fields in LiNbO3 crystals". In: *Ferroelectrics* 198.1 (1997), pp. 49–59. DOI: 10.1080/00150199708228337 (cit. on p. 136).

[236] Venkatraman Gopalan et al. "The role of nonstoichiometry in 180° domain switching of LiNbO3 crystals". In: *Applied Physics Letters* 72.16 (1998), pp. 1981–1983. DOI: 10.1063/1.121491 (cit. on p. 136).

[237] Venkatraman Gopalan, Terence E. Mitchell, and Kurt E. Sicakfus. "Switching kinetics of 180° domains in congruent LiNbO3 and LiTaO3 crystals". In: *Solid State Communications* 109.2 (1998), pp. 111–117. DOI: 10.1016/S0038-1098(98)00509-2 (cit. on p. 136).

[238] I. V. Kityk et al. "Band structure treatment of the influence of nonstoichiometric defects on optical properties in LiNbO3". In: *Journal of Applied Physics* 90.11 (2001), pp. 5542–5549. DOI: 10.1063/1.1413942 (cit. on p. 136).

[239] U. Schlarb and K. Betzler. "Influence of the defect structure on the refractive indices of undoped and Mg-doped lithium niobate". In: *Physical Review B* 50.2 (1994), pp. 751–757. DOI: 10.1103/PhysRevB.50.751 (cit. on p. 136).

[240] D. Bryan et al. "Magnesium-Doped Lithium Niobate For Higher Optical Power Applications". In: *Optical Engineering* 24.1 (1985), p. 241138 (cit. on p. 136).

[241] N. Iyi et al. "Defect Structure Model of MgO-Doped LiNbO3". In: *Journal of Solid State Chemistry* 118.1 (1995), pp. 148–152. DOI: 10.1006/jssc.1995.1323 (cit. on p. 136).

[242] Kiminori Mizuuchi et al. "Continuous-Wave Deep Blue Generation in a Periodically Poled MgO:LiNbO3Crystal by Single-Pass Frequency Doubling of a 912-nm Nd:GdVO4Laser". In: *Japanese Journal of Applied Physics* 43.No. 10A (2004), pp. L1293–L1295. DOI: 10.1143/jjap.43.11293 (cit. on p. 136).

[243] Joost Melai et al. "The electrical conduction and dielectric strength of SU-8". In: *Journal of Micromechanics and Microengineering* 19.6 (2009), p. 065012. DOI: 10.1088/0960-1317/19/6/065012 (cit. on p. 136).

[244] Hagen Bartzsch et al. "Electrical insulation properties of sputter-deposited SiO2, Si3N4 and Al2O3 films at room temperature and 400 °C". In: *physica status solidi (a)* 206.3 (2009), pp. 514–519. DOI: 10.1002/pssa.200880481 (cit. on p. 136).

[245] N. Ghalichechian and K. Sertel. "Permittivity and Loss Characterization of SU-8 Films for mmW and Terahertz Applications". In: *IEEE Antennas and Wireless Propagation Letters* 14 (2015), pp. 723–726. DOI: 10.1109/LAWP.2014.2380813 (cit. on p. 137).

[246] Paul R. Gray et al. *Analysis and design of analog integrated circuits*. John Wiley & Sons, 2009. ISBN: 0470245999 (cit. on p. 137).

[247] D. Taylor. "The Properties of Lithium Niobate". In: *EMIS Datareviews Series* 5 (2002) (cit. on p. 142).

[248] Badih El-Kareh and Lou N. Hutter. *Fundamentals of semiconductor processing technology*. Springer Science & Business Media, 2012. ISBN: 1461522099 (cit. on p. 142).

[249] J. K. Jones et al. "Channel waveguide laser at 1 micron in Yb-indiffused LiNbO3". In: *Optics Letters* 20.13 (1995), pp. 1477–1479. DOI: 10.1364/OL.20.001477 (cit. on p. 142).

[250] A. Mekis et al. "A Grating-Coupler-Enabled CMOS Photonics Platform". In: *IEEE Journal of Selected Topics in Quantum Electronics* 17.3 (2011), pp. 597–608. DOI: 10.1109/JSTQE.2010.2086049 (cit. on p. 145).

[251]   Constantin Dory et al. "Inverse-designed diamond photonics". In: *Nature Communications* 10.1 (2019), p. 3309. DOI: 10.1038/s41467-019-11343-1 (cit. on p. 145).

[252]   Mian Zhang et al. "Monolithic ultra-high-Q lithium niobate microring resonator". In: *Optica* 4.12 (2017), pp. 1536–1537. DOI: 10.1364/OPTICA.4.001536 (cit. on p. 145).

[253]   C. K. Hong, Z. Y. Ou, and L. Mandel. "Measurement of subpicosecond time intervals between two photons by interference". In: *Physical Review Letters* 59.18 (1987), pp. 2044–2046. DOI: 10.1103/PhysRevLett.59.2044 (cit. on p. 145).

Appendix B

Acknowledgements

First, I would like to thank Prof. Dr. Jörg Wrachtrup for giving me the opportunity to carry out my dissertation in the 3rd Institute of Physics in Stuttgart. He provided both guidance and infrastructure throughout this time, which gave me the chance to explore ideas in a truly inspiring manner and atmosphere. I also would like to thank Prof. Dr. Michler for taking the time to examine this dissertation and for sparking my interest for integrated photonics during his advanced seminar course.

I want to express special gratitude to my supervisor, Dr. Roman Kolesov, for being a steady source of scientific insights and guidance, and also of contagious enthusiasm for physics and creative ideas. Thank you for the fun times in the lab and for teaching me so much over the years.

Thank you to the rare-earth ion subgroup: Fiammetta for your positivity and bringing fresh perspectives into the group. Kangwei for introducing me to the lab in the very beginning of my PhD, staying in touch, and your all around genuine nature. I'm excited to see where your experiments will go in the future. Thank you to fellow colleagues, especially Matthias Niethammer, and the rest of the Gang, Matthias Widmann, Torsten Rendler, and Stefan Lasse, for staying late and grabbing the occasional beer, for the much needed

diversion at times, and in general for keeping an open ear and mind for inspiring discussions.

For all the technical assistance, instruction, maintenance and in general for keeping things running, I want to thank the respective people from the 3rd Institute of Physics, namely Stephan Hirschmann, Rainer Stöhr, Andrej Denisenko, and Rolf Reuter. From the 4th Institute of Physics, I want to thank Mario Hentschel, Monika Ubl, Bettina Frank, and Philipp Flad, for always being so helpful, easygoing, and in general a pleasure to work with. From the Max-Planck-Institute Stuttgart, I want to thank Thomas Reindl, Marion Hagel, Ulrike Waizmann, Thomas Meisner, and Arnold Weible, for all the help and advice they provided throughout these years.

I would like to thank my friends, foremost Bernhard Kohlmann, for his deep friendship and the joyful time we spent together over the past 18 years. Philipp Graus, for being my regular retreat during Pfingsten and all the great time spent together at the lake. Matthias Noebels and Fabian Weller for the ups and downs during game nights. Xiaochen Song, for supporting and accompanying me for the largest part of the PhD. Johannes Schmidt and Artur Skljarow for the entertaining time during BBQ evenings and in the city.

Most importantly, I wish to thank my family, my mother Elisabeth and my father Harry and my sisters, Anna and Andrea, for their love, patience, and support.

Thomas Kornher
July 2020

Erklärung über die Eigenständigkeit der Dissertation

Ich versichere, dass ich die vorliegende Arbeit mit dem Titel
„Spectroscopy and engineering of single rare-earth solid-state qubits"
selbständig verfasst und keine anderen als die angegebenen Quellen und Hilfsmittel benutzt habe; aus fremden Quellen entnommene Passagen und Gedanken sind als solche kenntlich gemacht.

Declaration of Authorship

I hereby certify that the dissertation entitled
„Spectroscopy and engineering of single rare-earth solid-state qubits"
is entirely my own work except where otherwise indicated. Passages and ideas from other sources have been clearly indicated.

Name/Name: Thomas Kornher

Unterschrift/Signed: _____

Datum/Date: _____